

Ph.D. Thesis



**FACULTY  
OF MECHANICAL  
ENGINEERING  
CTU IN PRAGUE**

Department of Process Engineering

# **Contactless heat transfer measurement methods in processing units**

**Bezkontaktní metody měření přestupu tepla v  
procesních zařízeních a aparátech**

**Ing. Stanislav Solnař**

Supervisor: prof. Ing. T. Jirout, Ph.D.

Supervisor: Ing. M. Dostál, Ph.D.

2021



# Acknowledgements

First of all, I would like to thank all colleagues and teachers at the Department of Process Engineering for surviving alongside me. Very often, our debates have led to great progress in a seemingly dead end. I would like to thank the supervisors of this work for their endless patience with me.

I thank the family for their support in good and bad times.

Many thanks to my bands Yo Mamma Band, DeZtraktor, Tomacula Calida, El Cigano White Boyz'n'Girlz, The Humid 5 and Rulík do Čaje for countless hours of rest and fun.

Many thanks to friends Bc. R. Žehlička, Mgr. E. Žehličková and dog Auroš, Ing. V. Kozák (tel. number: +420 728 299 290), brothers Martin, Alfréd and Boris, all three Ing., Ing. J. Pilař and Ing. T. Červenka from DZT s.r.o., (unbelievable) Ing. A. Nevečeřilová from DZT s.r.o. and many others that they have lived and survived this part of my life.

The biggest thanks goes to my lovely wife, Ing. Arch. Zuzanka!



# Declaration

I declare that I have worked on my Ph.D. thesis independently and have used only the literature listed in the attached list.

I have no serious reason to oppose the use of this school work within the meaning of Section 60 of Act No. 121/2000 Coll., On Copyright, on Rights Related to Copyright.

.....  
In Prague

.....  
Ing. Stanislav Solnař



# Abstract

Contactless measurement of local values of heat transfer coefficient by two different methods is presented in this Ph.D. thesis. The first method, temperature oscillation (also known as TOIRT method), uses heat waves from heat sources that hit the measured wall and measure the surface temperature of the wall using an IR camera. By comparing the phases of the individual signals (generated heat waves and the measured surface temperature) it is possible to obtain information about the phase delay, which is directly related to the coefficient of heat transfer.

I have validated the method experimentally when measuring the heat transfer coefficient between tube and flowing fluid in the tube and also numerically. Experimental measurements show results that are in agreement with the literature. The sensitivity analysis shows that this method is suitable for measuring the heat transfer coefficient in the range of  $100 - 3000 \text{ W/m}^2\text{K}$  with a reasonable error. After performing the verification experiments I applied the method to the measurement of geometries typical of process engineering such as vessels equipped with impellers or reactors. However, these apparatuses do not have simple but very complex flows inside and this method has never been used for similar applications.

The results of the measurement of the heat transfer coefficient at the bottom of the vessel equipped with impeller as well as on the wall of the vessel for various configurations and various impellers are presented. Data from the measurement of the heat transfer between the smooth wall and the perpendicular impinging jet are also presented. The results show good agreement with the literature except measurements on the wall of the vessel with the impeller, which show a different tendency.

The second method, which I derived for the non-oscillatory change in the heat flux that falls on the measured wall, calculates the local values of the heat transfer coefficient from the temperature response of the wall to the step function in heat flux. The method of heat flux jump (HFJ) is described, analytically and numerically verified and sensitivity analysis showed that it is suitable for small values of heat transfer coefficient, up to approximately  $1000 \text{ W/m}^2\text{K}$ . I have verified the method for measuring the heat transfer coefficient between a smooth wall and the impinging air jet with good agreement with the literature.

In addition to the measurement method itself, this method can also be applied to adjust and improve the results of the TOIRT method or even to measure the distribution of incident heat flux on the measured wall.

Both methods are very suitable for process engineering because they are fully contactless and do not require temperature measurement of the fluid between which heat transfer occurs. It is thus possible in this way to measure the heat transfer coefficient values in reactors with dangerous or toxic substances etc. Moreover, both methods are very fast in terms of both measurement and evaluation, and the new heat flux jump method is even faster.



# Nomenclature

Variable	Description (Unit)
$a$	thermal diffusivity ( $\text{m}^2/\text{s}$ )
$A$	amplitude ( $^{\circ}\text{C}$ , $\text{K}$ )
$A$	matrix (–)
$A, B$	model constants (–)
$B$	baffles width (m)
$C$	geometric constant (–)
$C$	heat capacity ( $\text{J}/\text{kg}$ )
$C_1, C_2$	model constants (–)
$c_0, c_1, c_2, c_3$	coefficients (–)
$c_p$	specific heat capacity ( $\text{J}/(\text{kg K})$ )
$d$	diameter (m)
$D$	vessel diameter (m)
$Er$	error (%)
$f$	frequency (Hz)
$f$	friction factor (–)
$g$	gravitational acceleration ( $\text{m}/\text{s}^2$ )
$Gr$	Grashof number (–)
$h$	height (m)
$h$	heat transfer coefficient ( $\text{W}/(\text{m}^2 \text{K})$ )
$H$	water level height (m)
$H(t)$	Heaviside function (–)
$i$	constant (–)
$k$	thermal conductivity ( $\text{W}/(\text{m K})$ )
$k, m, n$	exponents (–)
$L$	characteristic length, length (m)
$L_x, L_y$	length in $x$ or $y$ (m)
$m$	mass (kg)
$M$	number of iterations (–)
$N$	revolutions (rev/s)
$N_p$	power number (–)
$Nu$	Nusselt number (–)
$\overline{Nu}$	overall Nusselt number (–)
$p$	corection factor (–)
$P$	power (W)
$Pr$	Prandtl number (–)
$q$	heat flux density ( $\text{W}/\text{m}^2$ )

$Q$	heat (J)
$\dot{Q}$	heat rate (W)
$r$	radius (m)
Re	Reynolds number (–)
RS	relative sensitivity (%/deg, %/s)
$s$	Laplace variable (–)
$S$	surface (m <sup>2</sup> )
SNR	signal-to-noise ratio (dB)
Sc	Schmidt number (–)
$t$	time (s)
$t^*$	dimensionless time (–)
$T$	temperature (°C, K)
$\bar{T}$	Laplace image of temperature (–)
$u$	velocity (m/s)
$U$	voltage (V)
$\dot{V}$	volumetric flow (m <sup>3</sup> /s)
$w$	heat transfer coefficient ratio (–)
$x, y, z$	coordinates (m)
$z^*$	dimensionless coordinate (–)

### Greek letters

---

$\beta$	thermal expansion coefficient (1/K)
$\beta, \beta_k$	coefficients (–)
$\gamma, \gamma_k$	coefficients (–)
$\delta$	thickness (m)
$\delta_f$	boundary layer thickness (m)
$\delta_T$	thermal boundary layer thickness (m)
$\varepsilon$	emissivity (–)
$\vartheta$	oscillation part of temperature (°C, K)
$\lambda_c$	characteristic number (–)
$\mu$	dynamic viscosity (Pa s)
$\nu$	kinematic viscosity (m <sup>2</sup> /s)
$\nu_1, \nu_2$	coefficients (–)
$\xi$	dimensionless radius (–)
$\rho$	density (kg/m <sup>3</sup> )
$\tau$	time constant (s)
$\varphi$	phase (°)
$\Phi_E$	error (–)
$\sigma$	Stefan-Boltzman constant (W/(m <sup>2</sup> K <sup>4</sup> ))
$\psi_0$	coefficient (–)
$\omega$	angular velocity (rad/s)
$\Delta$	difference

$\nabla$  nabla operator

### **Subscripts**

---

0	initial, at $z = 0$ or $r = 0$
1,2	at $r = r_1$ , at $r = r_2$
a	ambient, analytical
cos	cosinus part
e	experimental
edd	measured with EDD method
f	fluid
G	generated
i	inner
M	mixing
max	maximum
min	minimum
N	normalized
new	new
s	substitution
set	set value
sin	sinus part
st	steady state
w	wall
$\delta$	at $z = \delta$



# Contents

<b>1</b>	<b>Introduction</b>	<b>15</b>
1.1	Basics of heat transfer . . . . .	15
<b>2</b>	<b>Heat transfer measurement methods</b>	<b>21</b>
2.1	Stationary methods . . . . .	22
2.2	Dynamic methods . . . . .	29
2.3	Oscillation methods . . . . .	33
2.4	Comparative methods . . . . .	35
<b>3</b>	<b>Aims of the work</b>	<b>39</b>
<b>4</b>	<b>Temperature oscillation method</b>	<b>41</b>
4.1	Theoretical background . . . . .	42
4.2	Data reduction . . . . .	49
4.3	Sensitivity analysis . . . . .	54
4.4	Numerical study . . . . .	56
4.5	Technical equipment . . . . .	60
4.6	Experimental validation . . . . .	63
4.7	Impinging jets . . . . .	67
4.8	Vessels equipped with agitators . . . . .	73
4.8.1	Bottom of vessels with agitators . . . . .	74
4.8.2	Wall of vessels with agitators . . . . .	82
<b>5</b>	<b>Heat flux jump method</b>	<b>89</b>
5.1	Theoretical background . . . . .	90
5.2	Numerical confirmation . . . . .	97
5.3	Data reduction . . . . .	99
5.4	Sensitivity analysis . . . . .	101
5.5	Experimental validation . . . . .	103
5.6	Impinging jets . . . . .	107
5.7	Wind tunnel . . . . .	110
5.8	Application to oscillation method . . . . .	115

<b>6</b>	<b>Future research</b>	<b>117</b>
<b>7</b>	<b>Conclusion</b>	<b>119</b>
<b>8</b>	<b>References</b>	<b>121</b>
<b>9</b>	<b>Appendix</b>	<b>129</b>

# Chapter 1

## Introduction

For a good design of the apparatus where heat exchange takes place, it is necessary to know very well the map of the intensity distribution of heat transfer in such apparatus. For the common engineering task of heat exchanger design we usually settle for the average value of heat transfer coefficient, but to improve design, reduce apparatus size or save money, it is necessary to display local values of heat transfer and study its changes with changing input parameters. The industry also calls for very fast and very accurate measurements of such quantities.

Despite the huge development of numerical simulations and thousands of scientific articles in the area of determining the values of heat transfer coefficient, experimental measurement still has its place also due to the validation of these numerical models. Experimental technique is constantly evolving, thus improving experimentally measured results and also increasing the speed of measurement and decreasing financial demands.

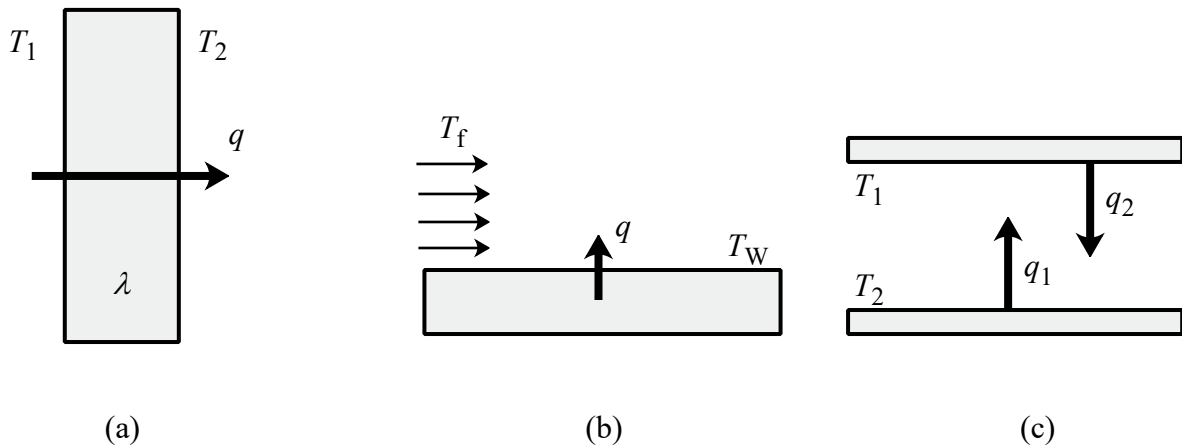
### 1.1 Basics of heat transfer

Heat transfer in general can be understood as energy that is in motion between two points that show different temperatures. We can say that there is a heat transfer between any two points with different temperatures. From the transmission point of view, three principles of heat transfer are known, namely conduction in solids or stationary fluids, convection between a solid wall and a flowing fluid, and radiation between two solid walls (Incropera et al. (2007)).

Conduction is associated with the mechanical energy of the particles at the microscopic scale and the energy is transmitted mechanically, by the movement of the particles. Conductive heat transfer can also occur in stationary fluids, but it is very often difficult to keep fluids stationary. Conductive heat flux can be expressed as the product of the material property and the temperature gradient, known as the Fourier law

$$q = -k\nabla T \quad (1.1)$$

where  $k$  represents the thermal conductivity of a material. This equation is named after J. B. J. Fourier, who first expressed this equation at the beginning of the 19th century. A negative sign in the equation is that the heat flows in the direction of the decreasing temperature.



■ **Figure 1.1:** Three types of heat transfer (a) conduction through a solid wall (or not moving fluid), (b) convection from surface to a fluid and (c) radiation between two walls.

Thermal conductivity can range from hundredths (air, gases, plastics ...) to tens and hundreds (aluminum, copper) and is a function of temperature. For one-dimensional heat conduction problems, it is usually possible to find an analytical solution for the heat flux through the wall (both stationary and non-stationary). For more complex problems (2D, 3D), we can often see the helping hand of numerical solutions (Incropera et al. (2007), VDI Heat Atlas (2010)).

Convective heat transfer is associated with macroscopic movement of flowing fluid. This type of transfer is actually a superposition of energy transfer due to the macroscopic movement of the fluid and the conductive heat transfer in the fluid. For this reason, convective heat transfer is dependent not only on the material properties, but also on the process properties such as fluid velocity, mixing intensity, shape of process equipment, etc.

The knowledge of convective heat transfer has a great influence on the design of new process equipment. A velocity and temperature profiles are created in the flowing fluid which has a direct impact on the magnitude of the heat transfer coefficient. Fluid behavior in the near wall region where large velocity and temperature gradients are known as boundary layers. This concept of boundary layers was first formulated by L. Prandtl at the beginning of the 20th century and is still in use.

The heat flux is directed towards a lower temperature so that in convection heat transfer both directions are possible (depending on the wall and fluid temperature, the wall can be heated or cooled) and its direction is considered normal to the wall surface. The amount of heat transferred depends on the velocity and temperature profile in the fluid and thus this task can become very complex e.g. for turbulent flow. We use the fairly simple relation to calculate the heat flux

$$q = h(T_W - T_f), \quad (1.2)$$

which is known as Newton's law of cooling. Symbol  $h$  represents the convective heat transfer coefficient that carries information about the material properties of the fluid, the geometric

properties of the task, the surface roughness of the wall, etc.

In the boundary layer concept there is a quantity of the thickness of the thermal boundary layer  $\delta_T$ . This thickness can be approximated as the thickness of the layer of a fictitious stationary fluid that transfers the same heat flux as the convective transfer. The temperature profile is then replaced by a linear temperature profile between  $T_W$  and  $T_f$  as if it were in conduction in a stationary fluid layer and the heat flux on the wall in the  $x$  direction can be expressed as

$$q = -k \left. \frac{\partial T}{\partial x} \right|_{x=0}. \quad (1.3)$$

By comparing equations (1.2) and (1.3) we can find another expression of the heat transfer coefficient

$$h = -k \frac{\left. \frac{\partial T}{\partial x} \right|_{x=0}}{T_W - T_f} \quad (1.4)$$

and the thermal boundary layer thickness can be approximated by  $\delta_T \approx k/h$ .

Based on the similarity method, it is possible to reduce the number of variables in equations by introducing dimensionless numbers, which are then the same for all geometrically similar problems. The dimensionless heat transfer coefficient is known as the Nusselt number named after W. Nusselt

$$\text{Nu} = \frac{hL}{k}, \quad (1.5)$$

where  $L$  represents the characteristic dimension of the measured system, most often the impeller diameter, the vessel diameter, the inner diameter of the tube, the distance from the plate edge and others. When dealing with convective heat transfer we can encounter two basic types, natural convection and forced convection. In forced convection, the fluid is driven by an external force (compressor, pump), while natural convection arises from the difference in density of the fluid (most often due to temperature changes).

The flow characteristics of natural and forced convection are generally described by Grashof and Reynolds numbers

$$\text{Gr} = \frac{L^3 g \beta \Delta T}{\nu^2} \quad (1.6)$$

and

$$\text{Re} = \frac{uL}{\nu} = \frac{uL\rho}{\mu}, \quad (1.7)$$

where  $L$  is the characteristic dimension,  $\beta$  volume expansion coefficient and  $\nu$  kinematic viscosity. In some cases (e.g. vessels equipped with impellers), it is better to replace the velocity  $u$  with the product of the rotational speed  $N$  and diameter of the impeller  $d$ , we are talking about mixing Reynolds number

$$\text{Re}_M = \frac{Nd^2\rho}{\mu}. \quad (1.8)$$

Other fluid parameters usually appear in a dimensionless form known as the Prandtl number

$$\text{Pr} = \frac{\nu}{a} = \frac{\mu c_p}{k}, \quad (1.9)$$

which represents the ratio of kinematic viscosity to thermal conductivity of fluids. This number can also be understood as a similarity between velocity and temperature fields in the fluid.

In the literature, the values of the heat transfer coefficient are usually not directly present, but their dimensionless form as the Nusselt number, which is given as a dependence of Reynolds (forced convection) or Grashof (natural convection) numbers and Prandtl numbers in the correlations.

$$\text{Nu} = f(\text{Re}, \text{Pr}) \quad \text{Nu} = f(\text{Gr}, \text{Pr}) \quad (1.10)$$

for the forced or natural convection respectively. These basic correlation relationships can be supplemented by other dimensionless criteria for a more accurate description of the system. Common correlation very often seen in literature is

$$\text{Nu} = C \text{Re}^m \text{Pr}^n, \quad (1.11)$$

which denotes the power dependence of dimensionless numbers and also add to equation the geometric constant  $C$ .

For engineering tasks of apparatus design and other applications, we often find ourselves satisfied with the average value of the Nusselt number  $\overline{\text{Nu}}$ , which represents the weighted average of the local values of the Nusselt numbers on the surface

$$\overline{\text{Nu}} = \frac{1}{S} \int_0^{L_x} \int_0^{L_y} \text{Nu}(x, y) \, dx \, dy. \quad (1.12)$$

The average Nusselt numbers are then given in the same correlation as the local values.

Some typical values of heat transfer coefficient for various situations are shown in the Table 1.1 (Incropera et al. (2007), VDI Heat Atlas (2010)).

■ **Table 1.1:** Typical values of heat transfer coefficient VDI Heat Atlas (2010).

<b>System</b>	$h$ (W/(m <sup>2</sup> K))
Free convection in gases	2 – 25
Free convection in liquids	10 – 1 000
Forced convection in gases	25 – 250
Forced convection in liquids	50 – 20 000
Boiling and condensing fluids	2 500 – 100 000

Radiation is the transfer of heat by means of electromagnetic waves, and so this transfer is also possible in vacuum, unlike the others. Any body emits radiation that is associated with the body's temperature. The basis for heat flux calculations is the so-called black body, which in practice is usually created by a body with an internal gap, which is heated to a certain temperature and has a small hole, which emits radiation energy out. The radiation heat flux of such a body can be described by relation

$$q = \sigma T^4, \quad (1.13)$$

where  $\sigma$  represents the Stefan-Boltzmann constant ( $\sigma = 5.67 \times 10^{-8} \text{ W}/(\text{m}^2 \text{ K}^4)$ ).

However, the radiation of real bodies is lower than that of a black body due to various influences whose impact does not change very much and so their influence is applied in the emission coefficient  $\varepsilon$  and the bodies are then called grey, which are defined by  $\varepsilon = \text{const.}$  Emissivity takes values from 0 (bodies that emit no energy) to 1 (black body). Real bodies take values between them, e.g. polished aluminum  $\varepsilon = 0.04$ , polished steel  $\varepsilon = 0.3$  or dead oxidized steel  $\varepsilon = 0.96$  (VDI Heat Atlas (2010)).

Very interesting introduction to the heat transfer world is offered by Incropera et al. (2007), Rohsenow et al. (1998), Hauke (2008) or VDI Heat Atlas (2010).



# Chapter 2

## Heat transfer measurement methods

Methods of measuring heat transfer coefficient can be divided into many groups as stationary and dynamic, contact and non-contact, direct and indirect, etc. of which the most known are about three groups, namely stationary, dynamic and comparative methods.

Stationary methods are closely related to Newton's cooling law from whose definition these methods are based

$$\dot{Q} = hS\Delta T. \quad (2.1)$$

The heat exchange surface  $S$  is generally known or can be measured relatively simply and then to determine the heat transfer coefficient  $h$  there are two possibilities: to set the temperature difference  $\Delta T$  and read the supplied heat rate  $\dot{Q}$  or to set the heat rate  $\dot{Q}$  and read the temperature difference  $\Delta T$ .

These methods are widely used in the science world for their simplicity and accuracy, but these methods are very time consuming and also conditions such as perfect thermal insulation etc. must be ensured.

Dynamic methods work with system response to supplied thermal information (lonely or periodically repeating). These methods are very fast but demanding on experimental components (usually very fast reading) and these methods are generally less accurate than stationary methods, but they can offer some positives such as complete contactlessness of the method, which may be useful in industrial measurement.

Comparative methods work on the principle of similarity between heat transfer and mass transfer. On this basis, mass transfer is measured in a geometrically identical or similar system, which is then converted into heat transfer. These methods are very interesting with different accuracy and speed.

In the literature we can also find some special methods such as optical, but they are very rarely used.

The first experimental work of measuring the heat transfer coefficient can be found during the 1920s and mostly in Europe. Rummel, Nusselt, or Hausen's work was primarily focused on describing and calculating the thermal characteristics of regenerators or air heaters, which was

the main target of heat transfer at that time. In the pre-war period it is possible to find several works, in the vast majority of German. During World War II, it was not published very much and further experimental work can be found in the early 1950s, but mostly from the 70s onwards. A very interesting publication dealing with the beginnings of heat transfer measurement is Willmott (1993).

## 2.1 Stationary methods

Cummings and West (1950) prepared an experiment to measure the heat transfer between the agitated liquid in the vessel and the coiled baffles that was installed in the vessel. In an agitated vessel equipped with a pair of agitators (both axial and radial type) on a common shaft, the temperature of the fluid was measured and 4 additional thermocouples were installed at the inlet and outlet of the cooling coil and the inlet and outlet of heating steam to the duplicator. The cooling water flow was measured with a calibrated rotameter with an inaccuracy of up to 2%.

From all the temperatures measured, the authors then calculated the heat transfer coefficient for different rotational speeds, different cooling water flows and also for the various agitators using the energy balance of the system. Their work is also supplemented by experimental measurements on other liquids such as glycerol, toluene, isopropyl alcohol and others. It is also possible to find information on heat transfer in the fluid-solid multiphase system.

Hagedorn (1965) measured in his thesis the heat transfer in mixing apparatuses with Newtonian and non-Newtonian liquids, especially pseudoplastic materials. He used the semi-static method of heating and cooling of the agitated batch in a perfectly insulated system. The agitated vessel was fitted with a duplicator into which low pressure steam (in case of heating) or cooling water (in case of cooling) flowed. The vessel was also provided with baffles and various types of stirrers that are common for mixing non-Newtonian liquids.

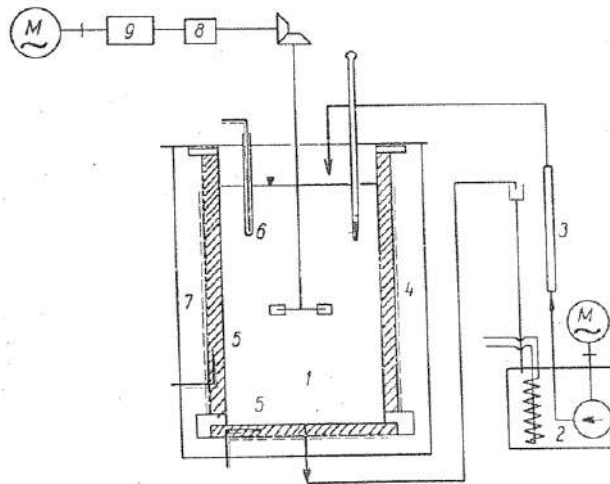
On the basis of the calorimetric equation

$$Q = m c_p \Delta T, \quad (2.2)$$

the heat rate, which is transferred with the batch whose temperature was measured by a thermometer and its thermophysical properties as well as mass, were calculated. The dissipated heat from fluid mixing was also taken into account in the calculations as a correction factor. The wall temperature was measured in the middle of the wall and further the surface temperature was calculated based on the Fourier heat conduction law. From the calculated heat flux and from the measured temperatures in the vessel and the surface temperature of the agitated vessel, the author calculated the overall value of the heat transfer coefficient.

Author reports an average measurement error in the range of 6-35% depending on the fluid used. Non-Newtonian fluids with a flow index lower than 1 show a greater measurement error than Newtonian fluids. At the end of the work the author presents a series of correlations for various geometries he measured.

Kupčík (1974) measured the overall value of the heat transfer coefficient on the wall and at the bottom of the agitated vessel with various impellers. For experiments, he used a thermally insulated vessel to which constant temperature water was supplied from the thermostat. Heat losses to the surroundings were calculated as 1 to 2% and therefore were not considered in the calculations.

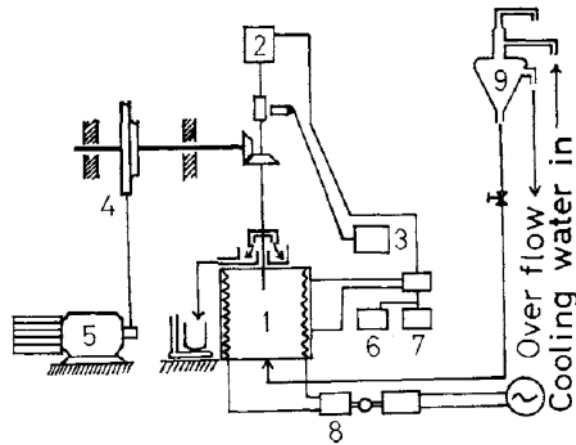


■ **Figure 2.1:** Apparatus scheme used by Kupčík (1974). 1 - vessel with impeller, 2 - thermostat, 3 - flowmeter, 4 - electric resistance heating, 5, 6 - thermocouples, 7 - insulating, 8, 9 - speed variator and revolution counter.

The steel vessel was heated on the walls and in the bottom by an electric heating wire and differential thermocouples were placed on the walls (the other end was placed in the liquid). After stabilizing the thermodynamic equilibrium in the system, temperatures were read, as well as power in a thermostat that kept the fluid at a constant temperature. The inaccuracy of such a measurement method is not mentioned in the article, only deviations of the determined exponents of the Reynolds number from the theoretical value, which is even 30%.

Ishibashi et al. (1979) measured heat transfer in mixed containers with special types of impellers such as helical-screw or double and quadruple helical-ribbon impeller. A thermally insulated, flat-bottomed vessel made of copper was heated by a heating coil in close proximity to the outer wall. Based on the good thermal conductivity of the material used, they assumed an even distribution of the wall temperature in the stirred vessel. The top and bottom of the vessel were also thermally insulated from the environment. The cooling water or aqueous glycerin solution was kept at a constant temperature externally and its temperature at inlet and outlet from the vessel was measured with thermocouples. Another series of thermocouples was placed to measure the surface temperature of the agitated vessel wall.

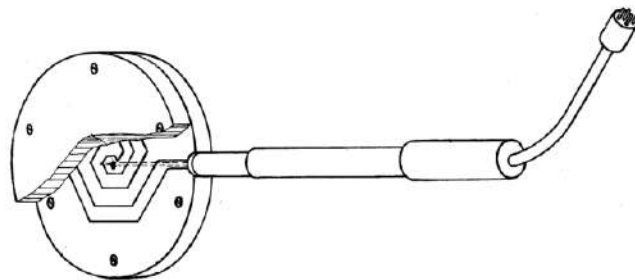
Due to the good thermal insulation of the vessel the authors ignored the heat loss to the surroundings. The heat supplied to the system was calculated from the change in coolant temperature. Based on Newton's cooling law, the relevant heat transfer coefficient was then calculated. Experimental measurements on the wall of an agitated vessel were compared with literature and



■ **Figure 2.2:** Apparatus scheme used by Ishibashi et al. (1979). 1 - vessel with impeller, 2 - slip-ring, 3 - revolution counter, 4 - transmission, 5 - motor, 6 - pen coder, 7 - digital voltmeter, 8 - wattmeter, 9 - constant head tank.

the results were in very good agreement.

Tydlitát et al. (1977) prepared a methodology for measuring the heat transfer coefficient and a measuring device that they also patented. The measuring device consists of a sensor with heating wire and temperature measurement. The measurement is done by heating the sensor to a temperature higher than the ambient temperature and controlling it while the sensor is cooled by surrounding heat transfer. The set temperature difference is maintained by a heating wire connected to the wattmeter and the dissipated power is monitored from which the heat transfer coefficient can be calculated.

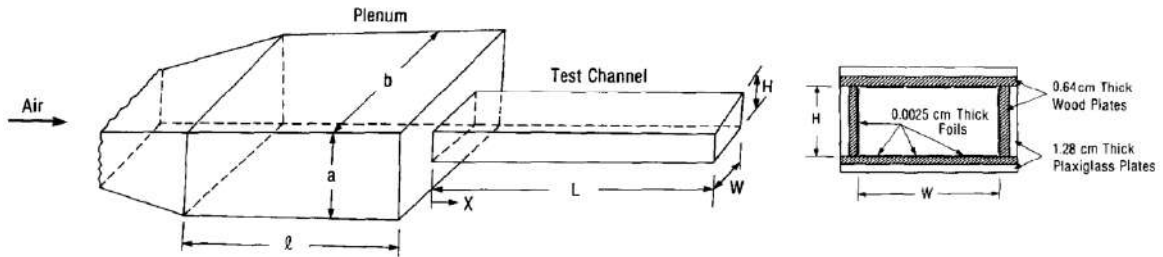


■ **Figure 2.3:** Patented device for measuring heat transfer coefficient by Tydlitát et al. (1977).

Authors recommend keeping the temperature difference very small in order to avoid parasitic effects such as natural convection around the measuring probe. In general, the device is more suited for measuring of larger values of heat transfer coefficient such as flow around an aircraft wing or fast moving vehicles. There is no information about inaccuracy of this method of heat

transfer coefficient measurement.

Han and Park (1988) measured the local values of the heat transfer coefficient in the square and rectangular cooling channels of the turbines. In experiments they measured both smooth and rib channels to increase turbulence. The replacement channel model was mainly made of Plexiglass, which was coated by a thin stainless steel sheet and on which strip foil heaters were installed in series. The model was also fitted with a total of 90 thermometers in different positions to obtain local values.



■ **Figure 2.4:** Apparatus scheme used by Han and Park (1988).

On the basis of Eq. (2.1), the electrical power to the strip foil heaters was measured, which was dissipated into the heat, as well as the temperature of the flowing air and the local channel temperature. From this information, the authors calculated local values of the heat transfer coefficient and reported inaccuracy of this method up to 8%.

Experimental results from the smooth channel were compared with the McAdams (originally Dittus and Boelter) correlation for fluid flow in a tube for fully turbulent flow

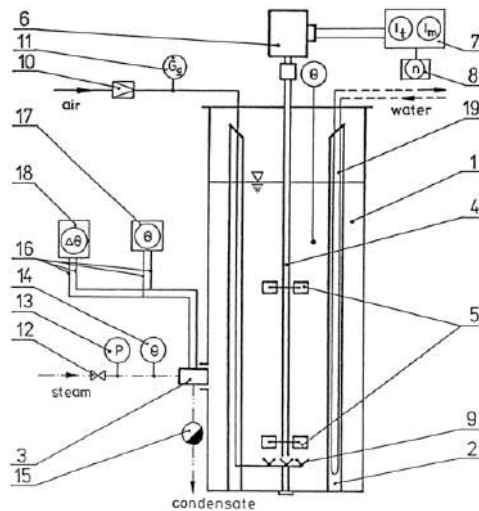
$$Nu = 0.023 Re^{0.8} Pr^{0.4} \quad (2.3)$$

and stated that the measured Nusselt number values are 5-15% higher than those predicted by the McAdams correlation.

For the ribbed ducts where the copper fins were glued to the existing model, the heat transfer coefficient increased rapidly and the dependence of the heat transfer increase with the rib angle applied in the duct was also observed. It was also observed that when applying ribs to channels, the distribution of the Nusselt number is not a smooth line, but an oscillatory gradually decreasing dependence.

Karcz (1999), before studying the heat transfer using the electrochemical method, studied the heat transfer on the wall of an agitated vessel at the multi-phase flow using a stationary method with its own heat flux meters. The heat flux meter is designed according to the law of heat conduction and so two calibrated thermometers are placed in the measuring body. On the basis of the measured thermal difference between these thermometers and their distance, which is known, it is possible to calculate the heat flux passing through this probe.

The outside of the agitated vessel was heated with condensing steam to a constant temperature. The temperature of the medium (distilled water or else) was measured with a thermometer



■ **Figure 2.5:** Experimental setup used by Karcz (1999). 1, 2 - agitated vessel, baffles, 3 - local heat flux meter, 4 - shaft, 5 - impellers, 6 - motor, 7 - steering unit, 8 - revolution counter, 9 - gas sparger, 10 - control valve, 11- flow meter, 12 - valve, 13 - manometer, 14 - thermometer, 15 - condenser pot, 17 - thermostat, 18 - point recorder.

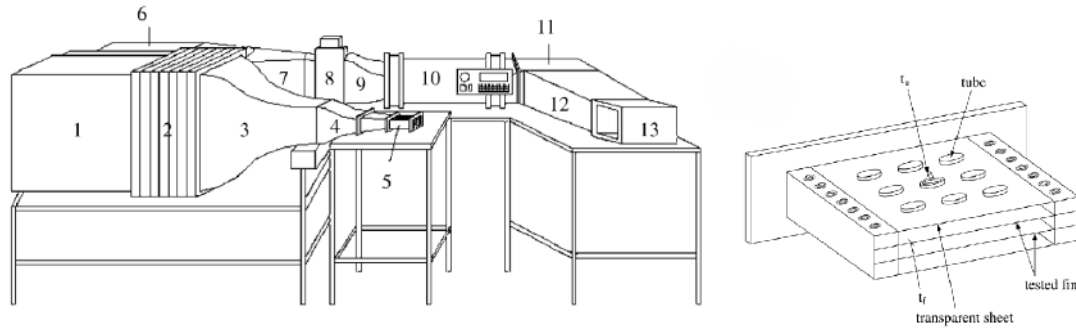
and the wall temperature (required to calculate the heat transfer coefficient) was calculated based on the Fourier heat conduction equation. By comparing the heat flux and the temperature difference, the local values of the heat transfer coefficient are calculated.

The article also discusses the inaccuracy (or correction factor) of the measuring device depending on the vessel radius. Author stated that for all measured liquids the change of the vessel shape due to the measuring element has no effect (correction factor is equal to 1) for vessels with a radius greater than 30 mm.

Herchang et al. (2002), using an IR camera, measured the heat transfer coefficient on the wall to which tubes were attached in two configurations, in-line position and alternately side by side position. The air flow (that was induced by the axial fan) cooled the tubes and the measuring plate. Resistance heaters were installed in the tubes to preheat them to a constant temperature. After stabilization of the system to thermodynamic equilibrium, the measured surface was photographed by an IR camera and the heat transfer coefficient could be calculated on the basis of the energy balance.

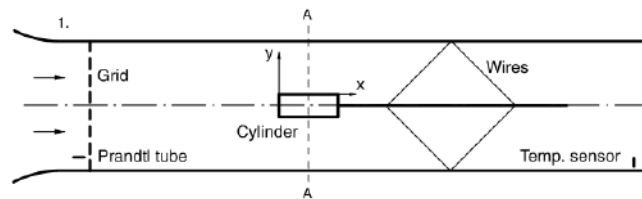
The balance of the system counted on the heat transfer in the plate and by means of a finite element scheme (which was the same as the resolution of the IR camera) the partial differential equations were converted into a system of ordinary equations that are easily solvable. Their measured heat transfer coefficient was thus not only dependent on the temperature difference between the wall and the flowing medium so lateral conduction in the measured wall was also taken into account. Authors write that the determined inaccuracy of the method is  $\pm 7.5\%$ .

At the end of their work, they found that moving pipes from the in-line configuration to the side-by-side configuration can significantly increase the heat transfer rate.



■ **Figure 2.6:** Experimental setup used by Herchang et al. (2002). 1, 6 - corner, 2 - settling chamber, 3, 4 - contraction section, 5 - test section (see the right picture), 7 - diffuser, 8 - heater, 10 - fan.

Wiberg and Lior (2005) used a stationary method with a heating film and a layer of thermally active colors (TLC) in an air channel, where the cylinder was overflowed by the air. The cylinder was made of extruded polystyrene with very low thermal conductivity to minimize heat loss to the measured cylinder. The heat loss to the environment due to the radiation was included in the evaluation of the experiment, according to the authors it was 4 - 10% of the total heat flux in the system.

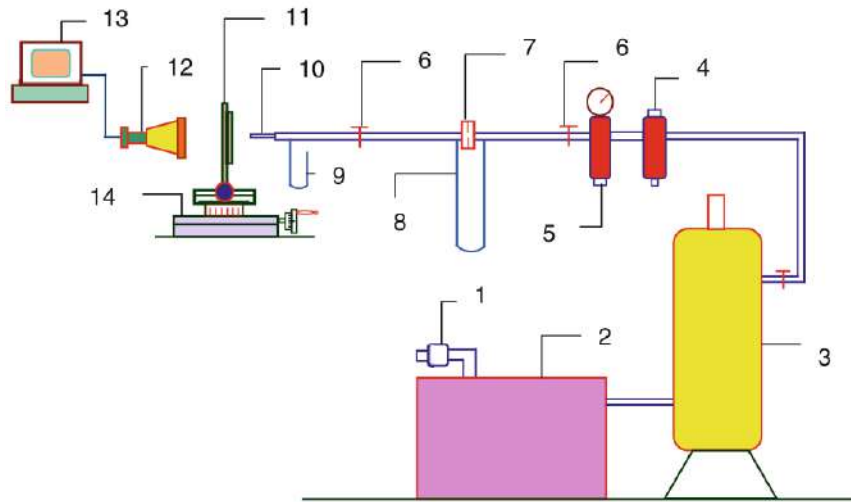


■ **Figure 2.7:** Experimental setup used by Wiberg and Lior (2005).

During the measurement, the surface of the object was heated by the heating film and the power input of the heating films were measured. After the system is stabilized, a TLC layer was photographed and the color photograph was converted to a surface temperature map from the calibration curve. The local heat transfer coefficient with a theoretical inaccuracy of 7% was calculated from temperature differences on the wall of the cylinder and in the air flow and from the measured power inputs to the heating film.

Katti et al. (2011) measured local values of the heat transfer coefficient between the smooth wall and the impinging air jet for low Reynolds numbers ranging from 500 to 8 000. Impinging jet was generated by the compressor through a long tube and the outlet pointed perpendicular to the heated plate. The heated plate (resp. foil, thickness was 0.06 mm) was placed in a structure that held the target and was also provided with ohmic heating. From the knowledge of the voltage and electric current passing through the target, it is possible to calculate Joule's heat dissipating into the target. The air temperature was measured with a K-type thermometer and the target was also scanned by an IR camera.

Based on the knowledge of the supplied heat output from ohmic heating and the difference between the target and air temperatures, they were able to calculate the values of the heat



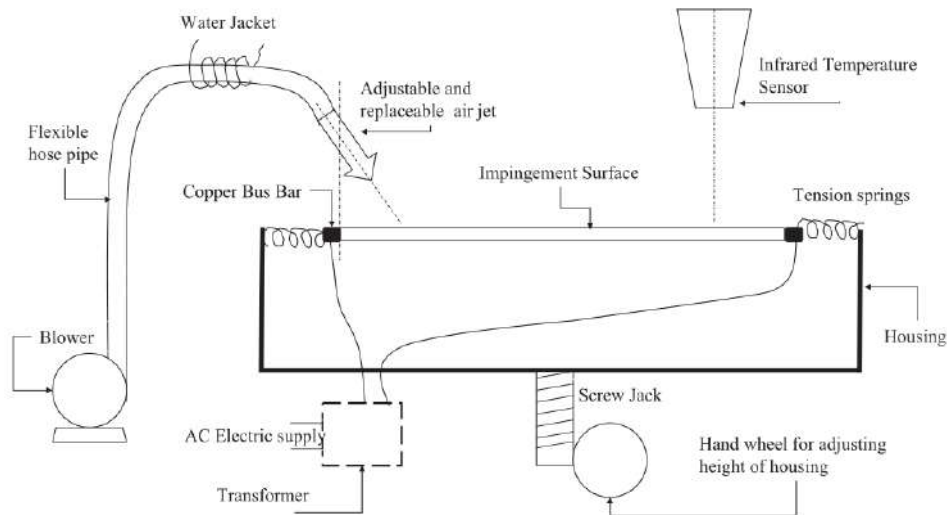
■ **Figure 2.8:** Experimental scheme used by Katti et al. (2011). 1, 4 - air filter, 2 - compressor, 3 - vessel, 5 - pressure regulator, 6 - valve, 7 - venturi meter, 8, 9 - manometer, 10 - nozzle, 11 - impingement plate assembly, 12 - IR camera, 13 - PC, 14 - traverse system.

transfer coefficient. Losses to the environment by radiation and natural convection have been determined experimentally and are described in detail in Katti and Prabhu (2008).

Experimental results were validated by comparison with literature. The results are given as dependencies of the local value of the Nusselt number in dependence on the radial coordinate as well as a correlation relationship for the average value of the Nusselt number over the whole measured area of the experiment. The authors report an inaccuracy of the experiment of 4%.

Ingole and Sundaram (2016) measured local values of heat transfer coefficient when the hot wall was cooled by a stream of cold air that formed an angle with the plate, the so-called inclined impinging jet experiment. The very thin plate was heated by electric current (total 150W) and the temperature was influenced by the incident air flow. In principle, the same method differed in measuring local temperatures, the authors used a contactless thermometer, which was moved to different positions during the experiment and from which the experiment was later evaluated.

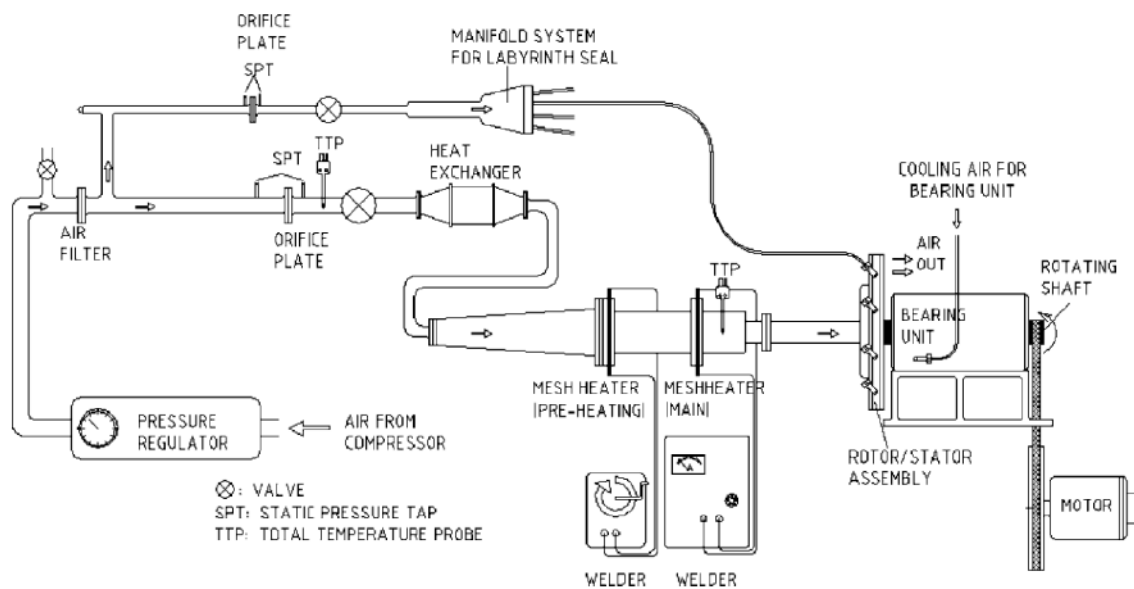
Environmental losses were not measured experimentally, but were calculated. The conductive loss was neglected due to the very small thickness of the measuring plate. Radiation loss into the environment was calculated based on the measured emissivity and was approximately 30W. The convective loss to the environment by natural convection was calculated using appropriate correlation relations and was about 8W. The inaccuracy of the method is not mentioned in the article.



■ **Figure 2.9:** Experimental scheme used by Ingole and Sundaram (2016).

## 2.2 Dynamic methods

Newton et al. (2003) published an article dealing with a step change in the temperature of a flowing medium and how to calculate the heat transfer coefficient from this change. However, the well-known derivation that leads to the solution of the error function was not considered correct, because it is not possible to achieve a perfect step change in temperature.

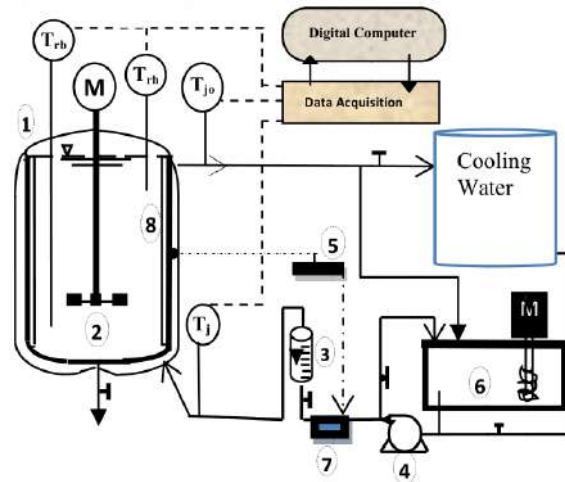


■ **Figure 2.10:** Experimental scheme used by Newton et al. (2003).

In the latter case, they replaced the excitation function with a much more realistic model, an exponential function that corresponds to the transition effect when the temperature changes.

Their solution (so-called slow transient) leads to the exponential sum series. They used this method to measure the heat transfer coefficient on a gas turbine model in the stator-rotor gap. In addition to the static results, they also observed a decrease in the heat transfer coefficient during the time of the experiment. Calibrated TLC layer was used to measure the surface temperature. Local values of the heat transfer coefficient were then determined from the measured temperature increase at the individual measuring points. The temperature change can be analytically calculated by summing the exponential functions and the coefficient has been determined by comparing the analytical and experimental results.

Debab et al. (2011) measured the overall heat transfer coefficient in a stirred vessel with a non-Newtonian power-type liquid. In their work, the batch was mixed with a radial agitator and the influence of the baffles, which were evenly distributed along the vessel wall, was studied. The vessel was fitted with a duplicator, which temperature was maintained via water in a circuit that was driven by a pump and measured by a flow meter. A total of 4 temperatures were measured at the inlet and outlet of the cooling water and then the temperature of the batch in the upper and lower parts of the agitated vessel.



■ **Figure 2.11:** Experimental rig used by Debab et al. (2011). 1 - vessel, 2 - impeller, 3 - flow meter, 4 - pump, 5 - temperature controller, 6 - thermostat, 7 - electric heater, 8 - baffles.

The values of the overall heat transfer coefficient were then calculated from the temperature record on the basis of the equation

$$h = \frac{m c_p}{S \Delta T} \frac{dT}{dt} \quad (2.4)$$

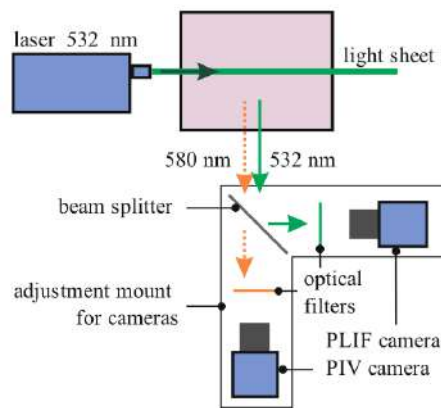
where the temperature derivative over time was replaced by the temperature difference over the time period that was set for data collection.

The inaccuracy of measurement by this method is not reported in the paper, but the authors state that for the basic design of such a device, the accuracy of the method is sufficient.

Jainski et al. (2014) as well as Nebuchinov et al. (2017) measured local values of heat transfer coefficient using a combination of optical methods: particle image velocimetry (PIV)

for velocity field measurement and planar laser induced fluorescence (PLIF) for temperature field measurement.

The PLIF method is based on the natural fluorescence of organic dyes when illuminated by laser. The fluorescence intensity (measured by the camera) is dependent on the amount of laser illumination (known parameter) and also on the temperature of the dyes, so it is possible to scan the temperature fields. However, special optical filters must be used for measurements and measurement has to be correctly calibrated. The PIV method allows us to track the velocity field. Calibrated particles are placed into the stream, which are also illuminated by a laser. From the individual images of particles, it is then possible to calculate their change of position and thus also direction and speed.



■ **Figure 2.12:** Optical setup for PIV and PLIF measurement used by Nebuchinov et al. (2017).

From these two fields it is then possible to determine the thickness of the boundary layer and thus the local values of the heat transfer coefficient. Authors state that the inaccuracy of temperature field measurement is below 5% and velocity field measurement is below 2%.

Věříšová et al. (2015) measured the overall values of the heat transfer coefficient on the wall of the agitated vessel in which the multistage stirrer was placed. The measurement was performed by a semi-dynamic method based on the heat balance in the system, from the theoretical point of view it was a perfectly isolated system. In such a system, the heat transfer coefficient can be calculated from the relation

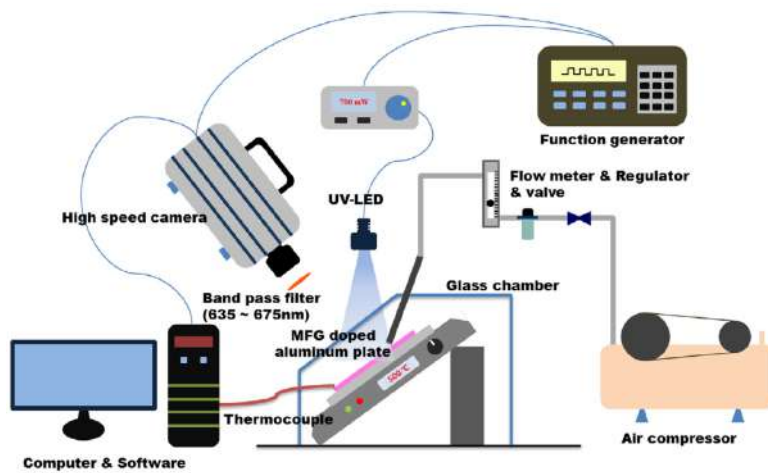
$$m c_p \frac{dT}{dt} = h S \Delta T. \quad (2.5)$$

Since the analytical solution assumes that the temperatures are invariant (which does not work for the wall temperature), the authors used a numerical solution of these equations and by a minimization algorithm sought the best match of the experimental data with the numerical solution.

The experiment was measured in heating and cooling cycles, i.e. two values of the heat transfer coefficient for one revolutions of the impeller was measured, namely the heat transfer coefficient for heating and cooling. Authors showed that these coefficients for heating and cool-

ing differ slightly. The inaccuracy of this measurement method is not mentioned in the article.

Yi et al. (2016) investigated the heat transfer between the heated smooth wall and the impinging air jet, which had different angles to the wall. In particular, the authors measured the transition characteristic of the heat transfer coefficient. They used thermographic phosphorus to monitor local temperatures of the wall which absorb the ultraviolet radiation at 385 nm and emit fluorescence of 650 nm wavelength. The intensity of irradiated fluorescence is dependent on the surface temperature of the wall, respectively at the phosphorus temperature. The measurement started by preheating the wall to a relatively high temperature (about 500 °C) and maintaining it by the controller and thermocouple. Then, a cold impinging air jet was triggered and the intensity of the irradiated fluorescence respectively the surface temperature was measured over time.



■ **Figure 2.13:** Experimental setup used by Yi et al. (2016).

In the measurement, authors assumed that the wall on which the heat transfer is measured behaves as 1D semi-infinite body, which on one side has, as a boundary condition, convective heat transfer. It follows from the derivation that the local value of the heat transfer coefficient can be calculated from the temperature record

$$\frac{T_W - T_0}{T_f - T_0} = 1 - \exp\left(-\frac{h^2 at}{k^2}\right) \operatorname{erfc}\left(\frac{h\sqrt{at}}{k}\right). \quad (2.6)$$

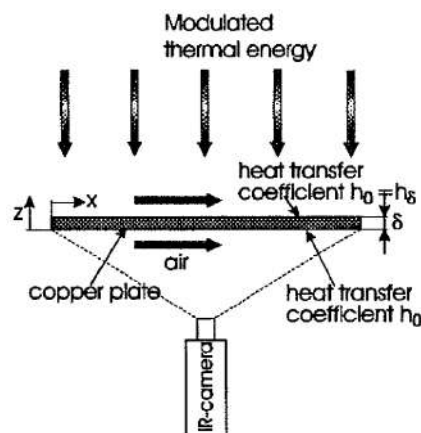
The authors found that the local values of the heat transfer coefficient drop nearly twice after 2 seconds of measurement than at the beginning and also that the shape and absolute values are very dependent on the angle of the impinging air jet.

This article is also supplemented with measurement using particle image velocimetry (PIV) method to clarify the formation of the second local maximum in the Nusselt number dependency. The authors stated that the secondary maximum is associated with the formation of an unstable vortex at the beginning of the wall jet zone. The inaccuracy of the method is not mentioned in the paper, only the inaccuracy of surface temperature measurement using thermographic phosphorus.

## 2.3 Oscillation methods

Oscillation methods are a specific part of dynamic methods. The original Hausen (1976) idea from the 1930s of using thermal oscillations to measure the heat transfer coefficient was further studied by his students Glaser (1938) and Langhans (1952), later also Kast (1965), Matulla and Orlicek (1971), Stang and Bush (1974) and Roetzel (1989).

Oscillation methods have a sinusoidal excitation function and monitor the temperature response of the wall to this signal. By comparing the phases of the individual signals (generated by the heat flux source and the wall temperature response) it is possible to calculate the heat transfer coefficient, more details are in the Chapter 4.



■ **Figure 2.14:** Schematic drawing of the experimental setup by Wandelt and Roetzel (1997).

Glaser (1938) studied the mean values of heat transfer coefficient in regenerators and heat exchangers by temperature oscillations. Langhans (1952) studied heat transfer and pressure loss in regenerators with an accumulation layer. Kast (1965), Matulla and Orlicek (1971) and Stang and Bush (1974) studied the heat transfer in beds and heat exchangers by analyzing the inlet and outlet temperatures that were modulated by the sine function. In addition, Stang and Bush (1974) used the amplitude of the measured signal to determine the average heat transfer coefficient. Finally, Roetzel (1989) applied temperature oscillations in the study of heat transfer in pipes, which is also mentioned in Roetzel and Prinzen (1991).

Roetzel et al. (1994) used temperature oscillation method to measure the performance of plate heat exchangers. In the experiment, they used two water loops, one of which was controlled for temperature oscillation by electric heating and cooling water. Fluid temperatures were measured at the inlet and outlet of the exchanger. By comparing the experimentally measured temperature phase delays with the analytically calculated values, the heat exchanger (NTU, number of transfer units) performance was determined. Authors stated that for lower Reynolds numbers, the results are very similar to literature, but for higher Reynolds numbers they show higher values, which may be associated with dispersion effects.

Perhaps the first real use of the TOIRT (Temperature Oscillation Infra Red Thermography) method to measure local heat transfer coefficient values (as used in my thesis) is Wandelt and

Roetzel (1997), which measured the heat transfer on the longitudinal flowed plate. The measured wall was influenced by the air flow from both sides in the same way, so the same value of the heat transfer coefficient on both sides of the measured wall was guaranteed. Radiative heat flux (sinusoidal modulation) was applied to the measured wall from one side and the local surface temperature was measured by an IR camera from the other side. By comparing experimentally measured results with available literature, authors found a relatively good agreement and thus confirmed the applicability of the TOIRT method for measuring the local values of the heat transfer coefficient, see Fig. 2.14.

Their work was followed by Freund (2008) in his thesis, which examined this new method thoroughly. In his work, besides the experiments themselves, it is possible to find research on the topic of oscillation methods. Previous research was mainly concerned with the history and development of the use of temperature oscillations for measuring the heat transfer coefficient. Two main methods have been identified from the literature, namely Prinzen and Wandelt, which differ from each other by the distribution of the delivered modulated heat flux. Prinzen's method consists in delivering heat flux through the laser to one point from which heat is propagated by conduction to other sites of the measured wall. The Wandelt method assumes homogeneous incident heat flux and thus neglects lateral conduction in the measured wall.

Freund studied this method and described its application in measurement in great detail. He encountered a problem of the non-oscillatory part of the data record, which had to be removed from the record to correctly evaluate the heat transfer coefficient (further information in Chapter 4). He dealt with imperfect distribution of incident heat flux as well as distribution of heat transfer coefficient using numerical model (finite element), which calculated iteratively values of heat fluxes at individual measuring points and map of heat transfer coefficient. For this numerical calculation, however, it was necessary to completely filter and smooth the data.

The method was validated theoretically and analytically with experimental measurement. For semi-infinite body, he calculated the expected temperature delay on the body surface and verified it experimentally. As with our measurements, he had to account for the delay in heat flux sources.

He finished his thesis by describing several experiments, such as impinging jets, spray cooling systems, plate heat exchangers or vortex generators in a wind tunnel, mostly 2D flows.

In the literature we can find several works dealing with temperature oscillations as a tool for measuring heat transfer coefficient from other authors. E.g. Carloff et al. (1994) measured the overall heat transfer coefficient on the wall of the agitated reaction tank by temperature oscillations. The modulated heat flux was fed into the agitated fluid by electric heating to both the batch and the reactor wall, and the heat transfer coefficient was calculated from the integral heat balance of the one-period system.

Ramirez et al. (1997) found that, based on the research, basic dynamic methods (step changes, rises and decays, pulsed perturbations ...) are not suitable for measuring the heat transfer coefficient for high NTU heat exchangers. On the other hand, he said, based on his other work, that the oscillation method is suitable for this type of measurement. The paper describes the mathematical model and application of the method and also states that the measured results show very good agreement with established heat transfer coefficient correlations.

Oscillations in the fluid temperature have also been successfully used to measure the thermop-

physical properties of materials, especially thermal conductivity. Czarnetzki and Roetzel (1995) used this method to measure the thermal conductivity of liquids that were enclosed in a measuring cell. The measuring cell was equipped with dual Peltier modules that generated temperature oscillations and their surface temperature was monitored. The thermal conductivity of the material was determined on the basis of the attenuation of the temperature oscillation amplitude and or on the basis of the phase delay of the measured temperatures on the module surface and a very well defined location in the fluid. Experimental measurements were made for several fluids (water, ethanol, glycerin and others) and the results show good agreement with the literature. The method has proven to be a very fast alternative for measuring thermal conductivity of liquids with reasonable precision.

Bhattacharya et al. (2006) used a very similar technique and, for accurate measurements, set the practical limits of the oscillating temperature periods as well as their amplitudes so that the measurement is unaffected by other phenomena (based on heating) and the measurement is very easy to read.

Industry also successfully use oscillation technique to investigate subsurface material failures, the so-called Lock-in thermography method.

## 2.4 Comparative methods

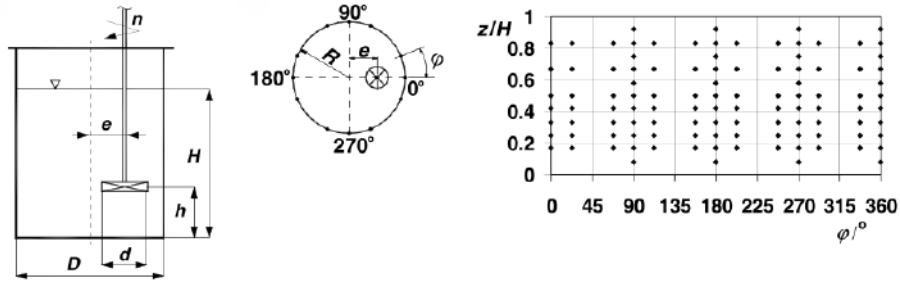
Nusselt (1916) dealt with the then much-studied problem, namely the speed of coal combustion. The coal blocks were placed in a closed reactor and were combusted in the presence of oxygen flowing from below the experiment. The measured coal losses were used to evaluate the combustion rate, which led to the determination of the convective diffusion coefficient. Author also compared this dependence (convective coefficient vs. velocity of flowing oxygen) with his measured dependence of heat transfer coefficient for the same geometry. From the results he stated that the dependences are very similar and thus actually confirmed the possibility of measuring the heat transfer coefficient using the mass transfer coefficient.

Lehner et al. (1999) presented an article on the measurement of the heat transfer coefficient using the ammonia absorption method. This method is based on capturing ammonia, which is added in very small quantities to the flowing medium, on a special filter paper which is pre-soaked in a  $\text{MnCl}_2$  solution. A chemical reaction occurs on the surface of the paper, which also serves as the measured wall, resulting in a local color change of the paper. Thus, at the end of the experiment, the color intensity of the paper at a given location is related to the intensity of mass transfer. Based on the calibration of the experiment it is then possible to calculate the local values of the mass transfer coefficient. The mass transfer coefficient can also be converted into local values of the heat transfer coefficient based on the analogy between heat and mass transfer.

Authors showed the functionality of the method in an airflow experiment with a small amount of ammonia along the wall (i.e. along the filter paper with  $\text{MnCl}_2$  solution).

Cudak and Karcz (2008) measured the local values of the heat transfer coefficient in an

agitated vessel with axial and radial impellers using the electrochemical (also electrodiffusion, EDD) method. This method measures the electrical current that passes between the anode and cathode in a conductive environment, which is usually an aqueous solution of a suitable salt. In this method the measured electric current is proportional to the mass transfer coefficient  $k_A$ . The heat transfer coefficient can then be calculated based on the similarity between heat and mass transfer. A total of 112 measuring probes were deployed during their experiment.



■ **Figure 2.15:** Experimental setup and probes location used by Cudak and Karcz (2008).

Conversion between the mass transfer and heat transfer coefficients is based on the ratio of Schmidt to Prandtl numbers, Cudak and Karcz (2008) used

$$\left(\frac{Sc}{Pr}\right)^{2/3} \quad (2.7)$$

After recalculation, the calculated value of the heat transfer coefficient must be corrected by a correction factor. The correction factor takes into account that even very small and thin electrodes interfere with the flow and disturb the boundary layer that changes on the measured wall. The correction factor (usually  $p$ ) represents the difference between the measured and the real value of the heat transfer coefficient, most often

$$p = \frac{h}{h_{edd}} \quad (2.8)$$

and can be determined experimentally or numerically. Authors measured several correction factors  $p$  depending on the configuration used.

Petera et al. (2017) used the electro-diffusion method (EDD) to measure the heat transfer coefficient at the bottom of the agitated vessel. The vessel was agitated with a 6PBT45 impeller, which was placed in a draft tube. Various system configurations were measured during the experiment. In this study, the effect of the tangential velocity component on the magnitude of the heat transfer coefficient at the bottom of the vessel was examined. The measured results were compared with the experiments of the impinging jet, where the tangential component of velocity does not occur and found that the tangential component has a significant influence on the values of the heat transfer coefficient.

The bottom of the vessel was made of Plexiglass, in which a total of 12 electrodiffusion probes were placed. The values of mass transfer coefficient and then their dimensionless form

were calculated from the measured electric current. By the ratio of Schmidt and Prandtl numbers it is possible to recalculate mass transfer to heat transfer (using the same ratio, see Eq. (2.7)). Authors used a numerical calculation to determine the correction factor  $p$ .

There are also other, not very often seen, methods to measure the heat transfer coefficient, e.g. Bokert and Johnson (1948) used an optical method using a Mach-Zhender interferometer to measure the heat transfer in a laminar flow. This method uses light bending and interference to track the field around objects. Authors used this method to measure the heat transfer in free convection around a heated cylinder, a heated wall and other objects. This method was also used at the International Space Station, see Ahadi and Saghir (2014).

There are hundreds of other articles on heat transfer coefficient measurement in the literature, but their methodology is either the same or a small modification of the methods mentioned here. Overall, the methods can be summarized into static, dynamic and comparative categories. Static methods are characterized mainly by high sensitivity and minimal measurement error. However, these methods are very time consuming, their modification on local value measurements is complicated and applicability in process engineering limited due to thermocouple temperature measurements or very narrow-band TLC. Comparative methods, based on the principle of similarity between heat and mass transfer, show good sensitivity and reasonable measurement error, but are fully dependent on laboratory models and cannot be applied when measuring on real devices. None of the comparative methods offers the possibility of contactless measurement.

Dynamic methods, due to the advancement in the field of measuring technology, are quite simple and very fast methods for determination of local values of heat transfer coefficient. Despite their great dependence on the conditions and shape of the excitement function, these methods are still successfully applied with reasonable sensitivity and measurement error. The temperature oscillation method excels with its full contactlessness and thus is directly suitable for application in process engineering, where we can also encounter apparatuses with dangerous or poisonous substances. It is also very fast method for measuring local values of heat transfer coefficient.

Other methods, such as optical, are very interesting, but their application is very limited and not very often used.

■ **Table 2.1:** Comparison of the most used experimental methods

method	year	range of $h$	inaccuracy	contactless	local values	time
Static-4 thermocouples	1950	$\approx 3000$	–	no	no	slow
Semistatic-calorimetric eq.	1965	$\approx 2000$	6 – 35%	no	no	medium
Static-2 thermocouples and controlled thermostat	1974	$\approx 3000$	–	no	no	slow
Static-set temperature difference, measured heat flux	1977	$> 1000$	–	no	yes	slow
Static-heated wall with local thermocouples	1988	$\approx 1000$	8%	no	yes	slow
Static-heat flux and temperature measurement by own probe	1999	$\approx 3000$	–	no	yes	slow
Static-IR camera scanning, preheat	2002	$\approx 1000$	8%	no	yes	medium
Static-TLC scanning, preheat	2005	$\approx 1000$	7%	no	yes	medium
Static-IR camera scanning, preheat	2011	$\approx 2000$	4%	no	yes	medium
Dynamic-slow transient step change temperature, TLC	2003	$\approx 1000$	–	no	yes	medium
Semidynamic-step change based on calorimetric eq.	2011	$\approx 3000$	sufficient	no	no	fast
Dynamic-PIV and PLIF measurement	2017	$\approx 1000$	5%	yes	yes	fast
Dynamic-oscillating method	2008	1000 – 8000	various	yes	yes	fast
Comparative-oxygen recalculation during combustion	1916	$\approx 1000$	–	no	no	slow
Comparative-ammonia absorption	1999	$\approx 1000$	–	no	yes	slow
Comparative-electrochemical	2008	1000 – 10000	8%	no	yes	medium

# Chapter 3

## Aims of the work

It is possible to use very precise static methods, very fast dynamic methods and / or comparative methods for experimental measurement of the heat transfer coefficient. All have their pros and cons, but the undeniable advantage of dynamic methods is their speed and ability to measure local values of transmission quantities.

Dynamic methods are not very often used for involved and complex fluid flows, such as heat transfer between a vessel wall and an agitated fluid, between a smooth wall and an incident impact stream, or between a wall and an air stream in a wind tunnel.

The main goal of this work is to apply the dynamic oscillation method to complex flows, which very often occur in process engineering, for studying local values of heat transfer intensity. The aim of the work is to answer if it is possible to apply this method with given boundary conditions to such a complex flow. Flow will surely affect the temperature profile over time in the measured wall and there is a question what concessions or compromises need to be made for the method to work in such conditions. During the experimental measurement, I found that the oscillation method is not suitable for very low heat transfer intensities (typically gas flows) and so the second main goal is to derive my own dynamic method that would allow the measurement of such flows. Based on a similar principle and the similar assumptions, the heat flux jump method is derived for a different input function and is investigated on basic and more complex gas flows. The overall goal of this work is divided into three partial goals:

### ■ Application of TOIRT method to complex flow geometry

Temperature oscillation method seems to be very suitable for measuring local and average heat transfer coefficient values in process units and apparatuses. Since it does not require any contact with the processing unit or the liquid in which the heat transfer takes place, it makes it possible to measure the heat transfer coefficient in containers and vessels with dangerous or even toxic liquids. Measurement results can be used to predict flow mode in devices or to detect changes in the vessel with regular measurements. However, this method has been tested on simpler geometries and I want to test its applicability to complex flow geometries such as vessels equipped with agitators.

■ **Numerical and technical research of the oscillation method**

The method has been thoroughly theoretically studied in the past and has also been experimentally verified on simpler geometries. I have prepared a numerical simulation study that allows to predict very quickly the surface temperatures in the measured wall. From the results of numerical simulations, I determined, among other things, the minimum number of heat waves for experimental measurements or the transient effect that occurs in the wall. Investigations of experimental equipment helped to improve the application of the method to individual geometries, mainly by the methodology of synchronization of used heat flux sources and data processing.

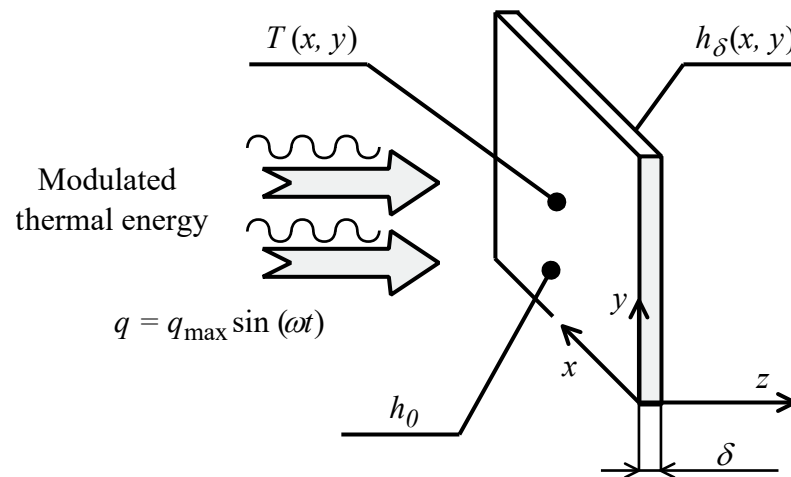
■ **Heat flux jump method**

Heat flux jump method is a logical continuation of the oscillation method. The transient effect of the oscillation method would make it impossible to use all the measured data, or it is necessary to measure a large amount of data to minimize the transient error. Both approaches are not very suitable and so I have analytically derived the wall temperature change for these experiments and its results can serve to remove the transient phenomenon. In addition, the derivation serves as a stand alone measurement method, which is very suitable for low values of the heat transfer coefficient or as a measurement method for determining the incident heat flux on a wall.

# Chapter 4

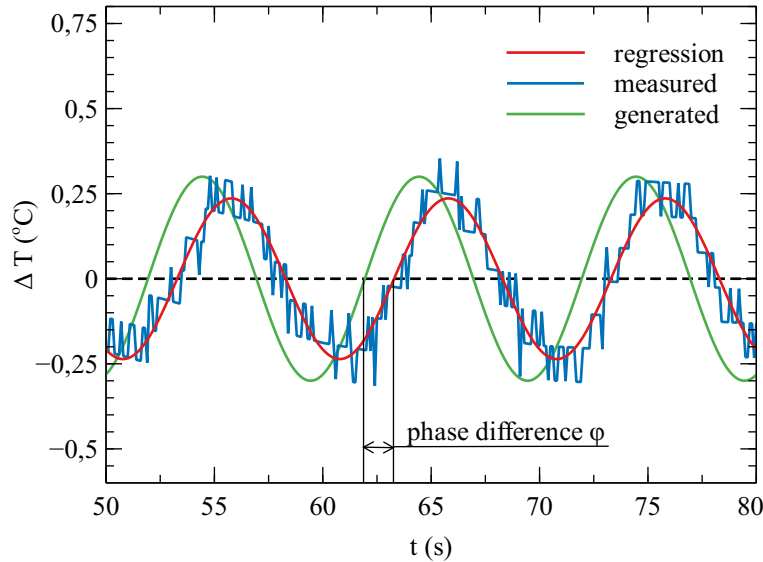
## Temperature oscillation method

The temperature oscillation method is a relatively new and not very often used method for measuring the local values of the heat transfer coefficient. The basis of the method consists in measuring the surface temperature of the measured wall at individual points by IR camera. The wall temperature is influenced by several factors, two of which are the strongest, namely the modulated heat flux and the heat transfer coefficient. If we influence the wall with the sinusoidal periodically repeated heat flux and measure the surface temperature, we find that the surface temperature is also modulated by the sine function, but is delayed behind the heat flux. It is the delay of the surface temperature behind the heat flux that is directly related to the heat transfer coefficient and thus can be determined. A schematic drawing of the method can be seen in the Fig. 4.1.



■ **Figure 4.1:** Schematic drawing of temperature oscillation method. The measured wall is shown in a Cartesian coordinate system where the wall in  $x$  and  $y$  has infinite length and in the  $z$  direction has a thickness  $\delta$ .

The phase difference between the signals (see Fig. 4.2) is directly related to the value of the heat transfer coefficient on the other (unlit) side of the board. It can be said with exaggeration that this method allows to see behind the opaque wall.



■ **Figure 4.2:** Example of comparison of generated and measured signal (obtained from measured data by regression).

If I use several contactless thermometers or IR camera to measure the surface temperature during the experiment, it is possible to obtain a map of the heat transfer coefficient intensity.

## 4.1 Theoretical background

There are several oscillatory methods for measuring heat transfer, which are based on different theoretical foundations. Their derivation, assumptions, results and procedures are summarized in Roetzel (1989), or in other publications that deal directly with one problem.

In this paper, all derivations are taken for a cylindrical coordinate system (the task was to apply the heat transfer measurement in a pipe and compare the results), but with some simple modifications they can be converted to a Cartesian coordinate system.

At the beginning it is useful to introduce some mathematical operations valid for oscillation signals. Basically, any periodic function is mathematically substitutable by the sum of several sine functions of different frequencies that can be evaluated individually (see for example Peireyra and Ward (2012)). If only the first harmonic function is of interest, the following equations can be obtained by applying Fourier harmonic analysis with numerical integration:

$$A_{\sin} = \frac{1}{\pi} \int_{t^*=0}^{2\pi} T(t^*) \sin t^* dt^* \quad (4.1)$$

and

$$A_{\cos} = \frac{1}{\pi} \int_{t^*=0}^{2\pi} T(t^*) \cos t^* dt^* \quad (4.2)$$

with dimensionless time  $t^*$  according to

$$t^* = \omega t = 2\pi f t. \quad (4.3)$$

When solving the following tasks, the total temperature can be divided into a steady, time-averaged temperature  $T_{st}$  and an oscillating component of the temperature  $\vartheta$ .

$$T(t) = \vartheta(t) + T_{st} \quad (4.4)$$

The first harmonic sine oscillation of the temperature can then be written as

$$\vartheta = A \sin(t^* + \varphi) \quad (4.5)$$

with amplitude

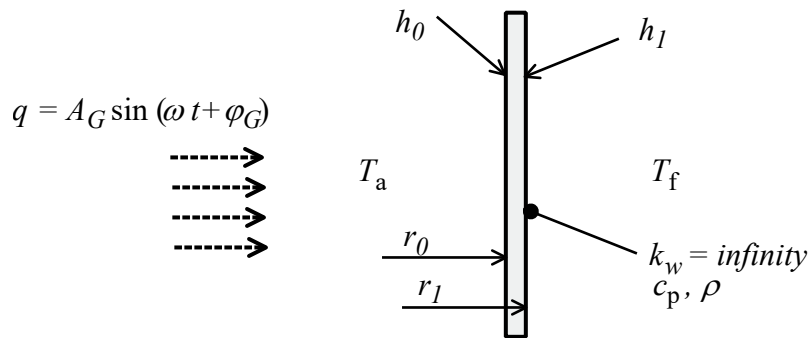
$$A = \sqrt{A_{\sin}^2 + A_{\cos}^2} \quad (4.6)$$

and phase shift

$$\varphi = \arctan\left(\frac{A_{\cos}}{A_{\sin}}\right) \quad (4.7)$$

#### ■ Zero wall resistance model

The zero wall resistance model assumes that the temperature in the fluid is perfectly mixed (is the same in the fluid) and the fluid temperature is only time dependent. This model is probably the simplest and was used also by Matulla and Orlicek (1971). For this calculation, no thermal resistance in the measured wall is assumed, which can be achieved only by a very thin measured wall with very good thermal conductivity (e.g. copper). For other materials, however, this model is unsatisfactory.



■ **Figure 4.3:** Schematic drawing of zero wall resistance model.

This simplest model solves the energy balance in a wall with infinitely high thermal conductivity (no wall thermal resistance). The rate of change in the wall temperature can be written as

$$\underbrace{(r_1^2 - r_0^2) \pi L \rho c_p}_{= C \text{ (heat capacity)}} \frac{dT}{dt} = h_1 S_1 (T_f - T) - h_0 S_0 (T - T_a) \quad (4.8)$$

with the heat transfer surface

$$S = 2 \pi r L. \quad (4.9)$$

For steady state thermal oscillation, the resulting temperature can be divided into two components, namely the oscillation temperature  $\vartheta$  and steady state temperature  $T_{st}$

$$T(t) = \vartheta(t) + T_{st}; T_f(t) = \vartheta_f(t) + T_{f,st}, \quad (4.10)$$

where temperatures with st index represent local time averaged temperatures, which in this case are the same as steady state temperature.

$$C \frac{d\vartheta}{dt} = h_1 S_1 (\vartheta_f - \vartheta) - h_0 S_0 (\vartheta) + \underbrace{h_1 S_1 (T_{f,st} - T_{st}) - h_0 S_0 (T_{f,st} - T_a)}_{=0} \quad (4.11)$$

It follows from the equation (4.11) that only the oscillatory component of the temperature record can be taken into account when deriving this task. If we measure the oscillation temperature on the wall according to

$$\vartheta = A \sin t^* \quad (4.12)$$

the temperature in the liquid will oscillate according to

$$\vartheta_f = A_f \sin(t^* + \varphi_f) \quad (4.13)$$

with phase shift  $\varphi_f > 0$ . The substitution of temperature oscillations (4.12 and 4.13) into the equation (4.11) implies that measurable phase delay  $\varphi_f$  can be expressed as

$$\varphi_f = \arctan \left( \frac{\omega C}{h_1 S_1 + h_0 S_0} \right) \quad (4.14)$$

and temperature amplitude in the fluid such as

$$A_f = A \sqrt{\left( \frac{\omega C}{h_1 S_1} \right)^2 + \left( 1 + \frac{h_0 S_0}{h_1 S_1} \right)^2} \quad (4.15)$$

Both equations (4.14 and 4.15) show that it is possible to calculate one heat transfer coefficient if the other is known. In this task where one side is heated and only natural convection is expected, the value of the heat transfer coefficient  $h_0$  can be calculated based on correlations and the heat transfer coefficient  $h_1$  can be calculated based on measured amplitudes or phase delay of the oscillation in the fluid temperature.

### ■ Finite wall resistance model

In the second case, it is assumed that the thermal conductivity  $k$  of the wall material is not infinite and that a temperature profile is formed in the wall. This more complex model is much closer to reality and the temperature profile must meet the energy equation. Introduction of dimensionless radius

$$\xi = r \sqrt{\frac{\omega}{2a}}, \quad (4.16)$$

the energy equation becomes

$$2 \frac{\partial T}{\partial t^*} = \frac{i}{\xi} \frac{\partial T}{\partial \xi} + \frac{\partial^2 T}{\partial \xi^2} \quad (4.17)$$

where  $i = 0$  for a plane wall,  $i = 1$  for a cylinder, and  $i = 2$  for a sphere. Such an equation assumes constant thermophysical properties of the wall over time (density  $\rho$  and thermal conductivity  $k$ ) and can be applied to different geometries by changing the value  $i$ .

If we again divide the total temperature into an oscillatory  $\vartheta$  and non-oscillatory part  $T_{st}$  (only applies to steady state oscillation conditions) we get the oscillatory temperature as a function of the coordinate  $\xi$  and time  $t^*$  and the temperature  $T_{st}$ , which is a function of only the coordinate  $\xi$

$$T(t^*, \xi) = \vartheta(t^*, \xi) + T_{st}(\xi). \quad (4.18)$$

By replacing the total temperature with two parts ( $\vartheta$  and  $T_{st}$ ) into Eq. (4.17) we get the expression

$$2 \frac{\partial \vartheta}{\partial t^*} = \frac{i}{\xi} \frac{\partial \vartheta}{\partial \xi} + \frac{\partial^2 \vartheta}{\partial \xi^2} + \underbrace{\frac{i}{\xi} \frac{\partial T_{st}}{\partial \xi} + \frac{\partial^2 T_{st}}{\partial \xi^2}}_{=0}. \quad (4.19)$$

This equation shows that the temperature profile  $T_{st}$  has no effect on the temperature oscillation profile  $\vartheta$ . Thus, the total temperature in Eq. (4.17) can be replaced only by the oscillating part of the temperature. The oscillation temperature is now given by (based on Eq. (4.12))

$$\vartheta = A e^{m(\xi)} \sin [t^* + \varphi(\xi)]. \quad (4.20)$$

For the same conditions as in the previous model, this expression returns back to the Eq. (4.12). Now it is necessary to determine both functions  $m(\xi)$  and  $\varphi(\xi)$  so that the boundary conditions and the energy equation are fulfilled. Derivation of both functions from Eq. (4.20) and substitution of them into Eq. (4.19) creates a system of two differential equations that must be solved

$$i \frac{\varphi_s}{\xi} + \frac{d\varphi_s}{d\xi} + 2 \varphi_s m_s = 2 \quad (4.21)$$

$$i \frac{m_s}{\xi} + \frac{dm_s}{d\xi} + m_s^2 - \varphi_s^2 = 0 \quad (4.22)$$

where  $\varphi_s$  and  $m_s$  are derivatives of functions

$$\varphi_s = \frac{d\varphi}{d\xi}; \quad m_s = \frac{dm}{d\xi} \quad (4.23)$$

The solution is based on the expansion of the polynomial function into a sum series, which will then be added together. Function expansion is

$$\frac{1}{\xi} = \frac{1}{\xi_0} \left[ 1 - \left( \frac{\xi - \xi_0}{\xi_0} \right) + \left( \frac{\xi - \xi_0}{\xi_0} \right)^2 - + \dots \right] \quad (4.24)$$

and is valid for  $|(\xi - \xi_0)| < \xi_0$ . Using this expansion, it is possible to calculate the derivatives of the  $\varphi_s$  and  $m_s$  functions using the sum series

$$\varphi_s = \sum_{k=0}^n \gamma_k (\xi - \xi_0)^k; \quad m_s = \sum_{k=0}^n \beta_k (\xi - \xi_0)^k \quad (4.25)$$

where the coefficients  $\gamma_k$  and  $\beta_k$  are

$$\gamma_k = \frac{1}{k} \left[ \sum_{i=0}^{k-1} \gamma_i (-\xi_0)^{i-k} - 2 \sum_{i=0}^{k-1} \gamma_i \beta_{(k-i-1)} \right] \quad (4.26)$$

and

$$\beta_k = \frac{1}{k} \left[ \sum_{i=0}^{k-1} \beta_i (-\xi_0)^{(i-k)} - \sum_{i=0}^{k-1} \beta_i \beta_{(k-i-1)} + \sum_{i=0}^{k-1} \gamma_i \gamma_{(k-i-1)} \right] \quad (4.27)$$

The sum of such a series can be used to calculate the derivatives of functions  $\varphi_s$  and  $m_s$  and by integrating also functions  $\varphi$  and  $m$

$$\varphi = \sum_{k=0}^n \frac{\gamma_k}{k+1} (\xi - \xi_0)^{(k+1)}; \quad m = \sum_{k=0}^n \frac{\beta_k}{k+1} (\xi - \xi_0)^{(k+1)}. \quad (4.28)$$

Using these results, it is then possible to write the harmonic temperature oscillation as

$$\vartheta = v_1 \frac{\xi_0}{\xi} \exp(\xi - \xi_0) \sin[t^* + (\xi - \xi_0)] + v_2 \frac{\xi_0}{\xi} \exp(\xi - \xi_0) \cos[t^* + (\xi - \xi_0)] + \frac{\xi_0}{\xi} \exp(\xi - \xi_0) \sin[t^* - (\xi - \xi_0)] \quad (4.29)$$

with coefficients

$$v_1 = \frac{\xi_0^2 (2 - \beta_0^2) - \xi_0 2\beta_0 - 1}{\xi_0^2 [1 + (1 - \beta_0)^2] - \xi_0 2(1 - \beta_0) + 1} \quad (4.30)$$

and

$$v_2 = \frac{-\xi_0^2 2\beta_0 - 2\xi_0}{\xi_0^2 [1 + (1 - \beta_0)^2] - \xi_0 2(1 - \beta_0) + 1}. \quad (4.31)$$

Equation (4.29) describes the temperature profile over time and at the location of the oscillating portion of the temperature. If the coefficients  $\varphi$  and  $m$  are already computable, the derivative of the oscillating temperature part  $\vartheta$  at the location  $\xi_1$  can also be calculated

$$\left. \frac{\partial \vartheta}{\partial \xi} \right|_{\xi=\xi_1} = \frac{r_1 - r_0}{|r_1 - r_0|} \frac{h_1}{k} \sqrt{\frac{2a}{\omega}} (\vartheta_f - \vartheta_1). \quad (4.32)$$

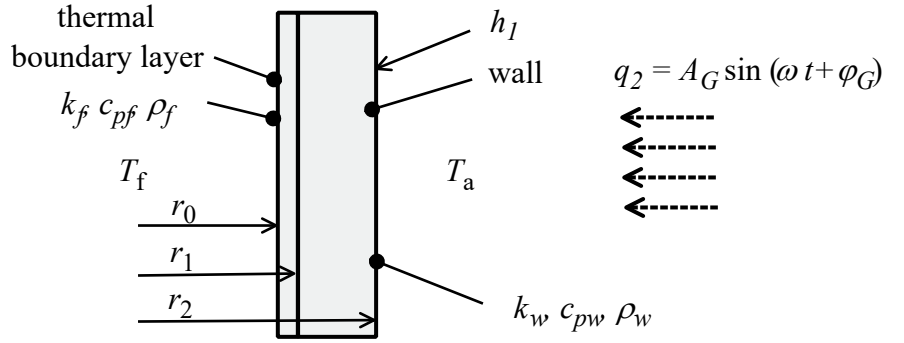
This equation can be understood the other way round: for the measured phase difference between the oscillating temperature part in the fluid and on the surface ( $\vartheta_f - \vartheta_1$ ), the derivative of the oscillating temperature part at the interface can be calculated and thus the heat transfer coefficient  $h_1$  can be determined.

### ■ Double thermal resistance model

As the last model presented here we show a model of double thermal resistance, which is based on the principle of boundary layers. This model also takes into account the thermal capacity and resistance of the boundary layer whose thickness is (see Fig. 4.4)

$$\delta_f = r_1 - r_0 = \frac{k_f}{h}. \quad (4.33)$$

The details and scheme of the double thermal resistance model are shown in the Fig. 4.4.



■ **Figure 4.4:** Schematic drawing of the double thermal resistance model.

Derivation is based on the same bases and assumptions as the model with finite wall resistance, so it is clear that the description of temperature in time and place must be the same. Using Eq. (4.29) and applying to the boundary layer we get

$$\begin{aligned} \vartheta_f = & v_1 \frac{r_0}{r} \exp(r - r_0) \sqrt{\frac{\omega}{2a_f}} \sin \left[ \omega t + (r - r_0) \sqrt{\frac{\omega}{2a_f}} \right] + \\ & v_2 \frac{r_0}{r} \exp(r - r_0) \sqrt{\frac{\omega}{2a_f}} \cos \left[ \omega t + (r - r_0) \sqrt{\frac{\omega}{2a_f}} \right] + \\ & \frac{r_0}{r} \exp(-(r - r_0)) \sqrt{\frac{\omega}{2a_f}} \sin \left[ \omega t - (r - r_0) \sqrt{\frac{\omega}{2a_f}} \right], \end{aligned} \quad (4.34)$$

which is already rewritten for dimensional variables. For place  $r = r_0$  the oscillation at temperature is equal to 0 and so it can be deduced that the values of constants  $v_1$  and  $v_2$  are

$$v_1 = -1; \quad v_2 = 0 \quad (4.35)$$

thus simplifying the equation to

$$\begin{aligned} \vartheta_f = & \frac{r_0}{r} \left[ -\exp(r - r_0) \sqrt{\frac{\omega}{2a_f}} \sin \left( \omega t + (r - r_0) \sqrt{\frac{\omega}{2a_f}} \right) \right] + \\ & \frac{r_0}{r} \left[ \exp(-r + r_0) \sqrt{\frac{\omega}{2a_f}} \sin \left( \omega t - (r - r_0) \sqrt{\frac{\omega}{2a_f}} \right) \right]. \end{aligned} \quad (4.36)$$

By setting the coordinate  $r = r_1$  we can find out that the temperature oscillations at this point can also be written from the boundary condition as

$$\vartheta_{f,1} = A_1 \sin(\omega t + \varphi_1). \quad (4.37)$$

The same Eq. (4.29) can also be applied to monitoring temperature oscillation in the wall with corresponding thermophysical properties

$$\begin{aligned} \vartheta_w = & v_1 \frac{r_1}{r} \exp(r - r_1) \sqrt{\frac{\omega}{2a_w}} \sin \left[ \omega t + (r - r_1) \sqrt{\frac{\omega}{2a_w}} \right] + \\ & v_2 \frac{r_1}{r} \exp(r - r_1) \sqrt{\frac{\omega}{2a_w}} \cos \left[ \omega t + (r - r_1) \sqrt{\frac{\omega}{2a_w}} \right] + \\ & \frac{r_1}{r} \exp-(r - r_1) \sqrt{\frac{\omega}{2a_w}} \sin \left[ \omega t - (r - r_1) \sqrt{\frac{\omega}{2a_w}} \right], \end{aligned} \quad (4.38)$$

for which we can find several boundary conditions. For  $r = r_1$ , the temperature (resp. temperature oscillation) must be the same for both sides (liquid and wall). At the same time, the heat flux  $q$  must be the same, which can be expressed by the thermal conductivity of the material and the temperature derivative at this point.

$$r = r_1 \rightarrow \vartheta_{f,1} = \vartheta_{w,1}; \quad k_f \frac{\partial \vartheta_{f,1}}{\partial r} = k_w \frac{\partial \vartheta_{w,1}}{\partial r} \quad (4.39)$$

On the coordinate  $r = r_2$  we can find the boundary condition for temperature oscillation, which is expressed by

$$\vartheta_{w,2} = A_2 \sin(\omega t + \varphi_2). \quad (4.40)$$

At this coordinate we also know the heat flux value

$$\dot{q}_2 = -k_w \left. \frac{\partial \vartheta_{w,2}}{\partial r} \right|_{r_2} = A_G \sin(\omega t + \varphi_G) - h_1 \Delta T \quad (4.41)$$

By comparing the heat fluxes (i.e. by comparing the derivative of the oscillatory parts of the temperature with the corresponding thermal conductivity) we get the dependence between the phase difference of the generated and surface signals  $\varphi_G - \varphi_2$  and the thickness of the liquid boundary layer  $\delta_f$ . Once the thickness of the boundary layer  $\delta_f$  is known, the heat transfer coefficient can be calculated based on

$$h = \frac{k_f}{\delta_f}. \quad (4.42)$$

On this basis, Roetzel (1989) and also Wandelt and Roetzel (1997) presented the resulting relationships between the phase delay and the heat transfer coefficient, from which the heat transfer coefficient can be evaluated based on the measured phase delay.

$$\tan \varphi|_{z=\delta} = \frac{c_1 + 2\xi \psi_0 c_2 + 2\xi^2 \psi_0^2 c_3}{2\xi \psi_0 (1+w) c_0 + 2\xi^2 \psi_0^2 (1+2w) c_1 + 4\xi^3 \psi_0^3 w c_2 + c_3} \quad (4.43)$$

To simplify this equation, the authors introduced several constants into the equation

$$\begin{aligned}
c_0 &= \cosh^2(\xi) \cos^2(\xi) + \sinh^2(\xi) \sin^2(\xi) \\
c_1 &= \cosh(\xi) \sinh(\xi) + \cos(\xi) \sin(\xi) \\
c_2 &= \cosh^2(\xi) \sin^2(\xi) + \sinh^2(\xi) \cos^2(\xi) \\
c_3 &= \cosh(\xi) \sinh(\xi) - \cos(\xi) \sin(\xi)
\end{aligned} \tag{4.44}$$

and several dimensionless variables

$$\begin{aligned}
\xi &= \delta \sqrt{\frac{\omega}{2a}} \\
w &= \frac{h_\delta}{h_0} \\
\psi_0 &= \frac{h_0 a}{\delta k \omega}
\end{aligned} \tag{4.45}$$

If the heat transfer coefficient on the illuminated side  $h_0$  would be of interest, the authors presented the relationship between the heat transfer coefficient and the phase delay

$$\tan \varphi|_{z=0} = \frac{2 \xi^2 \psi_0^2 w (\tan \xi - \tanh \xi) + 2 \xi \psi_0 (1+w) \tan \xi \tanh \xi + \tan \xi + \tanh \xi}{2 \xi^2 \psi_0^2 w (\tan \xi + \tanh \xi) + 2 \xi \psi_0 (1+w) - \tan \xi + \tanh \xi} \tag{4.46}$$

The heat transfer coefficient can also be determined from the measured amplitude of the oscillation temperature for both sides of the task (from both the illuminated side and the non-illuminated side)

$$A^2|_0 = \frac{(\delta q m/k)^2}{4 \xi^4 [\psi_0 (1+w)]^2 c_0 + 8 \xi^5 \psi_0^3 w (1+w) c_1 + (2 \xi^2 + 8 \xi^6 \psi_0^4 w^2) c_2 + 4 \xi^3 \psi_0 (1+w) c_3} \tag{4.47}$$

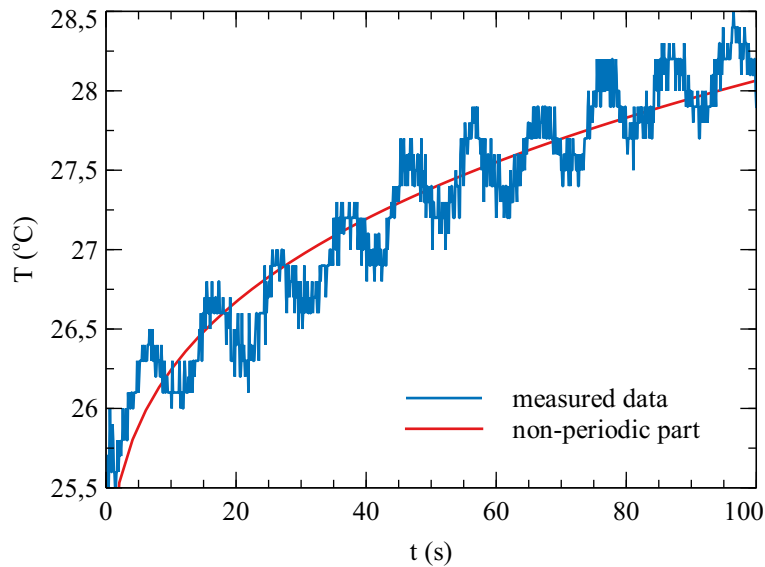
$$A^2|_\delta = \frac{(c_0 + 2 \xi \psi_0 c_1 + 2 \xi^2 \psi_0^2 c_2) (\delta q m/k)^2}{4 \xi^4 [\psi_0 (1+w)]^2 c_0 + 8 \xi^5 \psi_0^3 w (1+w) c_1 + (2 \xi^2 + 8 \xi^6 \psi_0^4 w^2) c_2 + 4 \xi^3 \psi_0 (1+w) c_3} \tag{4.48}$$

This is probably not clear from Eq. (4.43), but this solution says it is independent of the amount of heat flux delivered to the wall. It is therefore not necessary to know the source power or other parameters of the incident heat flux. This fact has a great effect on the measurement, because measuring the local values of the incident heat flux and its distribution on the wall is not a simple task. If we wanted to evaluate the heat transfer coefficients using the amplitude ratio, it is necessary to know the value of the incident heat flux.

## 4.2 Data reduction

IR camera data is saved in .csv format individually with time code and all images from one measurement are then uploaded to MATLAB where they are converted to .mat file with a prefix d as data and other information such as temperature or impeller speed etc.

The individual `d.mat` files are then loaded into the first MATLAB script, which modifies the measured data and looks for phase delays of the measured data. A typical data record is shown in the Fig 4.5 and we can see that the data record consists of two components, namely the periodic (oscillatory) and the non-periodic to which the periodic is superimposed.

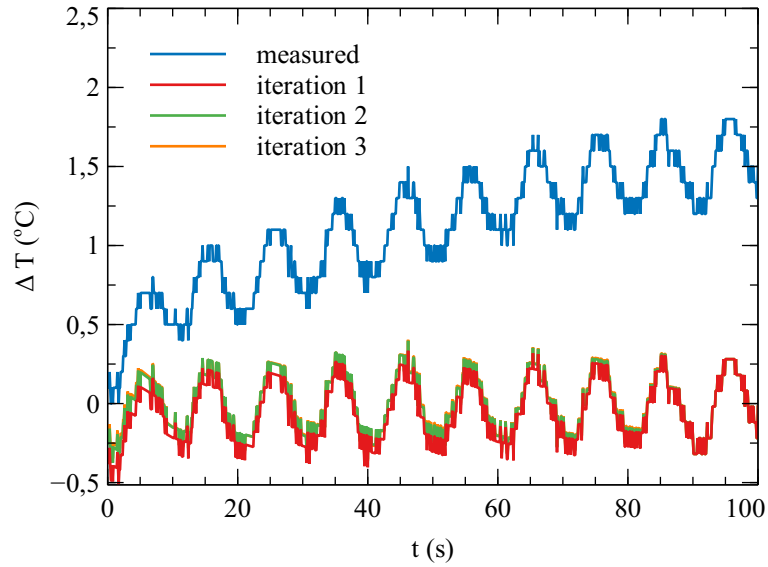


■ **Figure 4.5:** Typical data recording with evident periodic (oscillating) and non-periodic component.

The non-periodic part of the data record must be removed, otherwise the prerequisites of the method would not be met. Freund (2008) algorithm consisted of a sequential calculation of the mean values in each oscillation, which were then connected by a straight line and the measured data were subtracted from these straight lines. This process was repeated until absolute removal of the non-periodic portion of the record was achieved. According to Freund (2008), this modification of the data has no significant effect on the resulting heat transfer coefficient, on the contrary, not removing this dependence would lead to a systematic error of tens of percent.

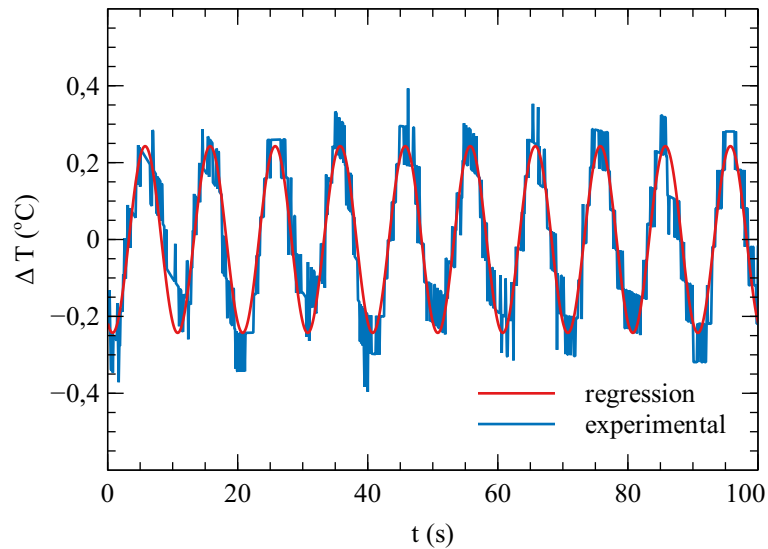
I use the Freund's so-called linear drift compensation algorithm to remove the non-periodic part of the record as well. During the experiments I tried other subtraction algorithms, mostly based on exponential or polynomial functions, but I obtained practically the same results. For measurements with a large number of oscillations, I use an updated Freund algorithm, which in the first two iterations looks for a polynomial function from which it subtracts data, which leads to faster data processing. Editing data when deleting a non-periodic part is shown in the Fig. 4.6.

After this operation, only the oscillatory component remains from the data, from which we determine its phase or its phase delay compared to the transmitted heat flux. To determine the phase delay, we use both: non-linear regression of the measured signal or single-frequency discrete Fourier Transform. Nonlinear regression is very robust to evaluate the phase shift on the other hand the Fourier transform is considerably faster. The use of regression or Fourier transform depends on the experiment and the magnitude of the measured temperature noise. The phase shifts are then stored in `f.mat` for further processing. Adjusted data and regression



■ **Figure 4.6:** Removal of non-periodic data component with the updated Freund's algorithm. Here, only the difference between the measured values and the initial value is shown for better display. The figure shows that after the second iteration, the oscillatory component of the data practically does not change.

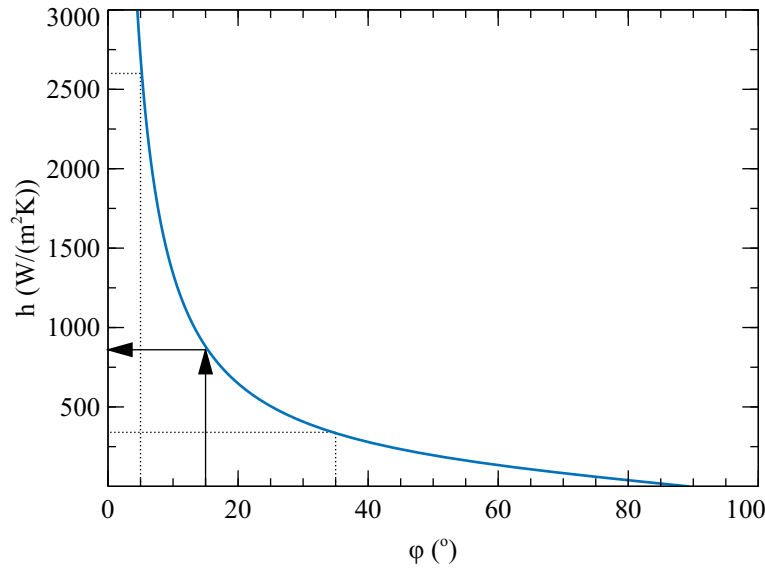
curve fit can be seen in the Fig. 4.7



■ **Figure 4.7:** Interleaving the adjusted data with a regression curve for one measurement point. This point has an amplitude of  $0.4858 \text{ } ^\circ\text{C}$  and a phase delay of  $27.58 \pm 1.47 \times 10^{-7}$  degrees (about 0.77 s), which for a given system represents a heat transfer coefficient  $h \approx 500 \text{ W}/(\text{m}^2 \text{ K})$

The phase shift matrix is read into the last script that converts them to the heat transfer coefficients  $h$ . Phase delay  $\varphi$  conversion is performed by interpolation of analytical solution (divided into 10 000 intervals, see Eq. (4.43)), dependence of phase delay  $\varphi$  and heat transfer

coefficient  $h$  can be seen in Fig. 4.8.



■ **Figure 4.8:** Analytical solution according to Wandelt and Roetzel (1997) presented as dependence of phase delay  $\varphi$  and heat transfer coefficient  $h$  for one experimental setup. The results are then interpolated from this dependency.

The shape of relationship of the heat transfer coefficient  $h$  and the phase delay  $\varphi$  can be changed by selecting the appropriate material to be used in the experiment. Above all, the wall capacity (specific heat capacity  $c_p$  and wall thickness  $\delta$ ) affects the shape of the curve.

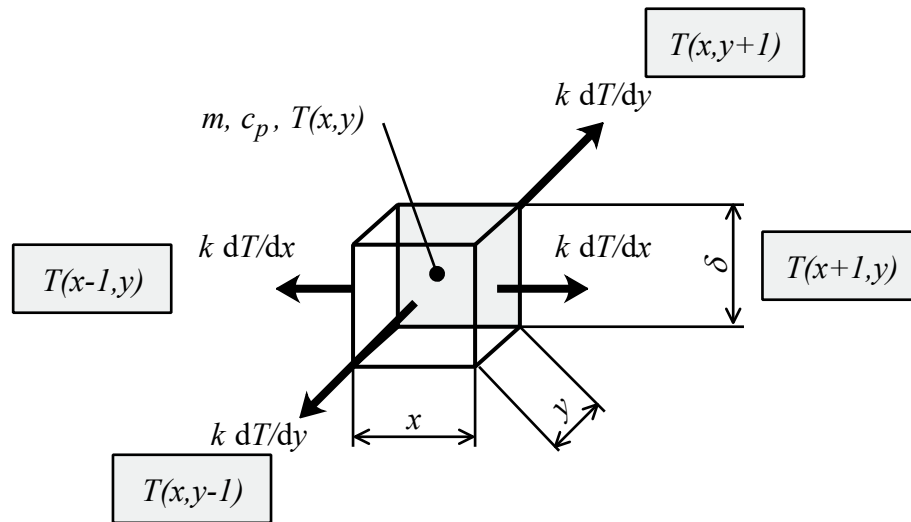
Freund (2008) also solved the problem with lateral conduction in the wall, which the method does not take into account. In his work we can find a numerical solver of finite difference model that takes into account this discrepancy with the theory of the method. Freund's algorithm actually solves the inverse problem, where the input information enters a local phase delay (resp. heat transfer coefficient) and the real values are calculated numerically. This modification of the data seems to better describe the problem and also the conduction in other directions, which surely arises here, but at the cost that it is necessary to adjust the measured data very strongly and smooth them over the surface, otherwise the model will start diverging.

In his thesis, Freund also set a limit when it is necessary to deal with lateral conduction in the wall and when it has a negligible effect. The decision related to a dimensionless wall thickness  $\xi$  that is defined as

$$\xi = \delta \sqrt{\frac{\omega}{2a}} \quad (4.49)$$

says that for values of  $\xi$  less than 0.5, lateral conduction in the wall is negligible with respect to other heat fluxes that take place. The dimensionless wall thickness  $\xi$  depends on the physical wall thickness  $\delta$ , the thermophysical properties of the wall  $a$ , and also the angular frequency of the transmitted heat waves  $\omega$ . Based on this, it is possible to prepare experimental measurements so that lateral conduction is negligible. In my experiments, the value of  $\xi$  was at most 0.25, but mostly around 0.1 and so I neglected this phenomenon.

I have also devised my algorithm that could describe lateral conduction and which is based on a very simple energy balance in the wall. My approach is much simpler and quicker, and its concept is based on dividing the board into cubes that exchange heat between them based on the Fourier heat conduction equation (see Fig. 4.9).



■ **Figure 4.9:** The idea of dividing the measured wall into individual elements in which the energy balance is solved.

Measured wall is divided into  $x \times y$  points (according to the resolution of the IR camera) and dimensions are given them according to the size of the scanned area. In the  $z$ -axis I leave the dimension equal to the wall thickness  $\delta$ . Then I read the individual measured temperature fields and calculate a new temperature  $T_{\text{new}}$  for each measured point. The new temperature is calculated from each heat flux to the sides due to the heat conduction in the wall and from the calorimetric equation. The new temperatures are stored in a matrix, which is then processed in the same way as raw data.

Comparing the original and modified data, I arrive at the result that the deviation of the calculated heat transfer coefficient from these data is less than 0.05%, which is a negligible value (modified data show lower heat transfer coefficient values). Such a low value of the difference between the modified and untreated data is probably due to the very low value of the dimensionless plate thickness  $\xi$  and hence the possibility of neglecting lateral conduction in the wall.

This script has a positive effect on the data, as it slightly smooths the temperature maps and therefore, even after evaluation, the heat transfer intensity map is slightly smoothed. However, I do not use this data modification because it is unnecessary. The script is ready for measurement with much larger values  $\xi$ .

### 4.3 Sensitivity analysis

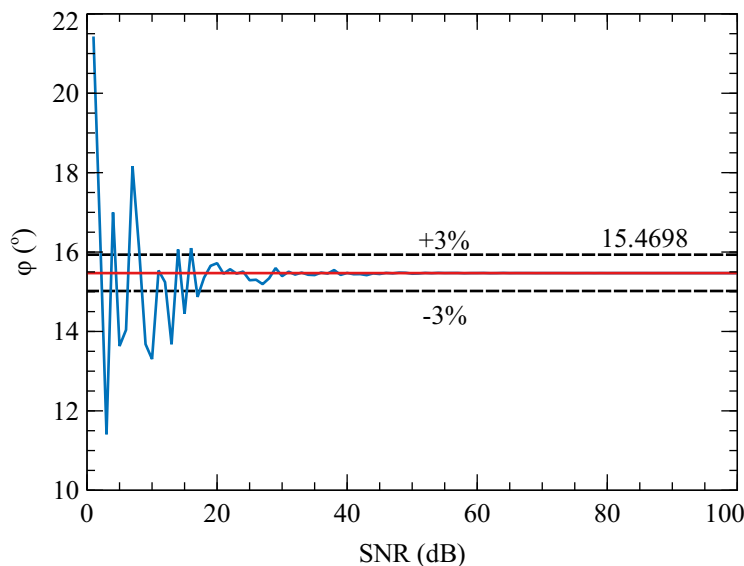
Within the sensitivity analysis I divided the influence of measured quantities on the resulting value of the heat transfer coefficient  $h_\delta$  into parts. The first part discusses the effect of measurement noise (surface temperatures) on the evaluation of the phase delay  $\varphi$ . In the second part the effect of sensitivity of phase delay change  $\varphi$  on the calculated heat transfer coefficients  $h_\delta$  is monitored. In the last phase the effects of individual thermophysical and physical properties of the measured wall are monitored.

In the first part I observed the effect of noisy data on the evaluation of the phase delay  $\varphi$ . I generated a sine wave with a given phase delay  $\varphi$  and then evaluated it again to look for its phase (as well as the measured data). I added to the original sine wave various amount of signal noise (MATLAB function `awgn`, type 'measured') and observed this effect. The degree of signal noise (or the signal distance from the noise) is mostly given by the SNR (signal-to-noise ratio)

$$\text{SNR} = \frac{A_{\text{signal}}}{A_{\text{noise}}} \quad (4.50)$$

i.e. the ratio of the amplitudes of the noise and the signal. This value is usually converted to logarithmic in dB (10 log).  $\text{SNR} = 1$  means that the amplitude of the signal and noise is equal. I used `snr` function in MATLAB for SNR calculation.

In the Fig. 4.10 we can see the dependence of evaluated phase delay  $\varphi$  on SNR and we can say that for SNR values greater than 40 dB the phase delay is consistent and does not change. Experimental data measured by us have an average SNR of 48.9 dB. A problem in converting between experimental data to phase delay  $\varphi$  could only occur in the case of very fast oscillations or for a badly selected (small) heat flux that is transmitted to the measured wall.

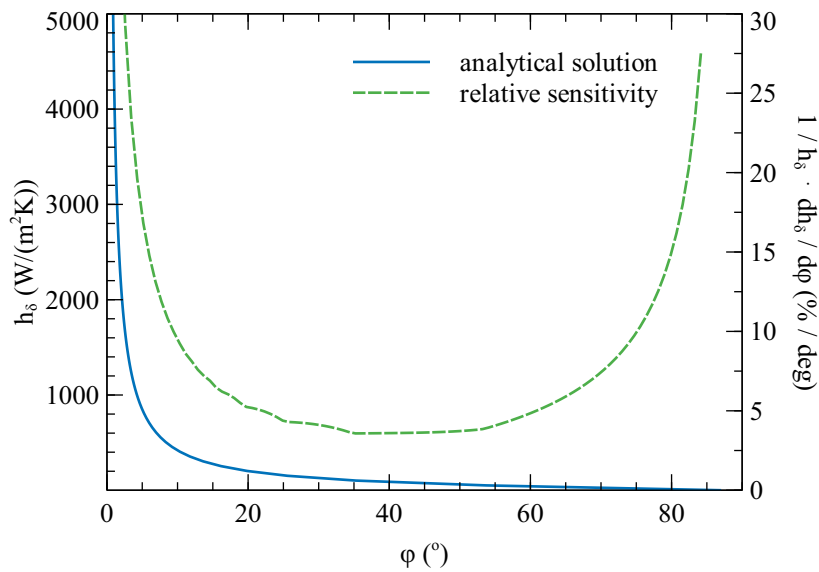


■ **Figure 4.10:** Dependence between evaluated phase delay and SNR. The correct (default) phase delay value is shown in red line.

In the second part, I monitored the sensitivity of the change in the heat transfer coefficient  $h_\delta$  when changing the phase delay  $\varphi$ . Relative sensitivity is mostly given in the literature as

$$RS = \frac{1}{h_\delta} \cdot \frac{dh_\delta}{d\varphi} \quad (4.51)$$

that I converted to percentages. The dependence of relative sensitivity can be seen in the Fig. 4.11. The sensitivity is less than 5% in the range  $20 \leq \varphi \leq 60^\circ$ , where it is very convenient to measure. However, sensitivity rises very quickly on both sides. Relative sensitivity does not change much as input parameters change (material, oscillation signal frequency, wall thickness, see Dostál et al. (2018) for more details).



■ **Figure 4.11:** Dependence of heat transfer coefficient  $h_\delta$  on phase delay  $\varphi$  according to Wandelt and Roetzel (1997) and relative sensitivity of heat transfer coefficient to phase delay change  $1/h_\delta \cdot dh_\delta/d\varphi$ .

In the third part I investigated the effect of individual thermophysical properties of the wall on the resulting heat transfer coefficient (see Tab. 4.1)

■ **Table 4.1:** Results of sensitivity analysis on thermophysical properties of the wall, its thickness and heat transfer coefficient  $h_0$  given as a change from resulting heat transfer coefficient  $h_{set}$ . Note:  $h_0$  (W/(m<sup>2</sup> K)),  $k$  (W/(mK)),  $\rho$  (kg/m<sup>3</sup>),  $c_p$  (J/(kg K)),  $\delta$  (mm).

$h_{set}$ W/(m <sup>2</sup> K)	$k$ ±10%	$\rho$ ±10%	$c_p$ ±10%	$\delta$ ±10%	$h_0$ ±10%
200 ( $\varphi = 50$ )	±0	±9.5	±10.1	±10.3	±0
1300 ( $\varphi = 10$ )	±0.1	±10.2	±9.9	±10.1	±0
8000 ( $\varphi = 1$ )	±0	±0.6	±0.9	±0.2	±0.1

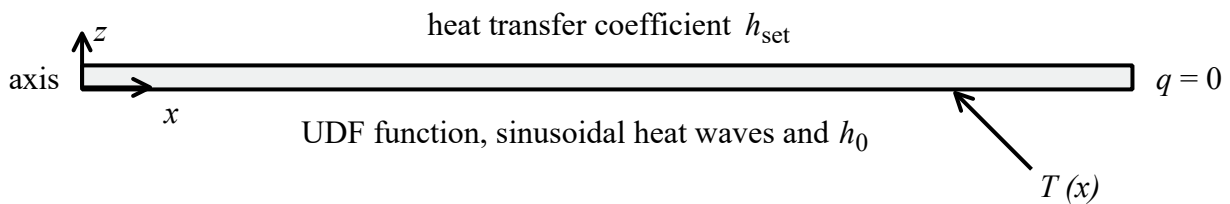
The sensitivity analysis shows that the heat transfer coefficient on the illuminated side  $h_0$  has almost no effect on the higher values of the heat transfer coefficient  $h_\delta$ . Even the change in

thermal conductivity  $k$  has no significant effect on the result, which is surprising. On the other hand, the specific heat capacity  $c_p$ , density  $\rho$  and physical wall thickness  $\delta$  have a fundamental impact on the results even in tens of percent. It is very suitable to measure the wall thickness precisely because it is the most sensitive input parameter.

## 4.4 Numerical study

When investigating the temperature oscillation method, I also used numerical modeling, which makes it possible to obtain results very quickly. Due to the nature of the simulation (heat conduction in a homogeneous wall), I have chosen a 2D wall model that will be provided with a UDF function (user defined function) that generates sinusoidal heat waves. Numerical simulations were performed in the well-known and very often used commercial software ANSYS CFD.

I replaced the measured wall (bottom vessel equipped with agitator, wall under impinging jet ...) by a 2D model of the plate, which was 1 mm thick and 200 mm in size. This model was replaced by a computing mesh with dimensions of  $1000 \times 40$  nodes, altogether 40 000 elements. All points were chosen as rectangular without refinement at the walls and so this computational grid is of high quality without any deformed elements.

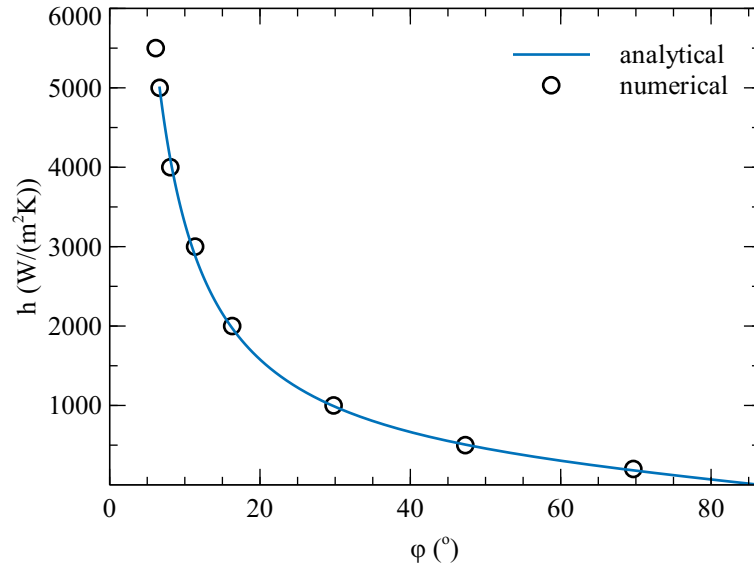


■ **Figure 4.12:** 2D model of simulated homogeneous wall with boundary conditions

As shown in Fig. 4.12, the measured wall is defined from the upper side by the boundary condition of the third type, where I set the value of the heat transfer coefficient  $h_{set}$ . At the bottom of the model is equipped with a UDF function for generating heat waves and there is also a condition of the third kind that simulates natural convection around the measured plate due to wall heating. The left boundary condition is chosen as an axis and the right condition of the third kind represents zero heat loss to the surroundings.

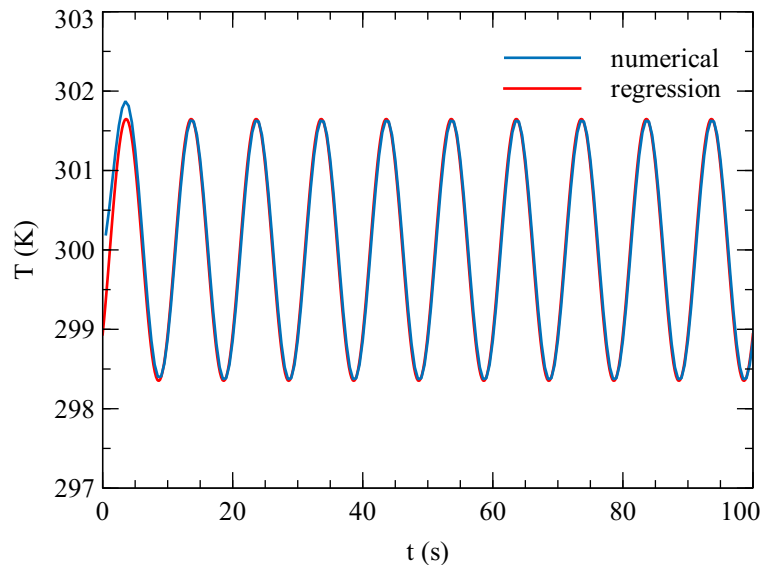
To validate the numerical model, I chose to compare the numerically calculated values with the analytical solution of Eq. (4.43) for the same experimental conditions (wall thickness, thermal conductivity, wall density and heat capacity, both heat transfer coefficients  $h_{set}$  and  $h_0$ ), I performed a numerical simulation for 100 heat waves with a time step of  $1/1000$  s. The comparison of the numerically calculated values with the analytical result can be seen in the Fig. 4.13.

Although the fit of the numerically calculated surface temperatures by the regression curve looks very good (see Fig. 4.14), it is possible to see some mismatches between the regression



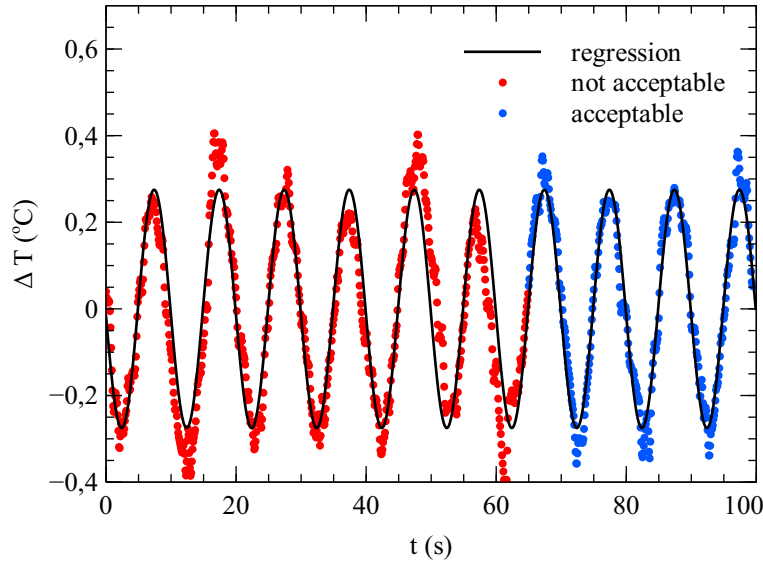
■ **Figure 4.13:** Comparison of numerically calculated values on 2D model with analytical solution of authors Wandelt and Roetzel (1997) for the same experimental conditions

curve and the calculated values at the beginning of the temperature time record. These small differences at the beginning of the record do not affect the overall non-linear regression in case a large number of thermal oscillations are detected. However, if we perform a non-linear regression for a smaller number of heat waves (in the extreme case for 1 or less), these initial deviations may create a significant difference in the evaluated phase delay and hence the evaluated heat transfer coefficient.



■ **Figure 4.14:** A comparison of numerically calculated temperatures and non-linear regression for heat waves with a period of 10 seconds ( $f = 0.1$  Hz) and for the heat transfer coefficient  $h_{\text{set}} = 2000$  W/(m² K). Only the first 10 heat waves are shown in this figure.

These imperfections are also observed in comparison of experimental temperature recording and nonlinear regression (see Fig. 4.15). Here, the differences are supplemented by the noise that occurs when measuring the surface temperatures of the wall with IR camera.



■ **Figure 4.15:** A comparison of experimentally measured temperatures and non-linear regression for heat waves with a period of 10 seconds ( $f = 0.1\text{Hz}$ ) and for the heat transfer coefficient  $h \approx 1600\text{W}/(\text{m}^2\text{K})$ . Data with red dots are visibly less interleaved with nonlinear regression. Data with blue dots are interleaved with regression perfectly. Only the first 10 heat waves are shown in this figure.

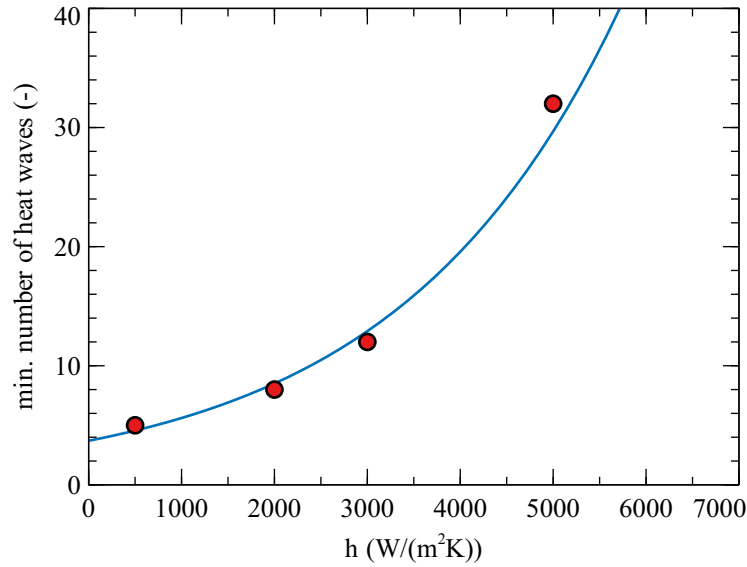
The first way to deal with this phenomenon is to determine the boundary where the non-linear regression does not perfectly describe the measured data and not to include these temperatures in the final non-linear regression. However, it can be seen from the picture that there can be a large amount of such data. When evaluating experimental measurements, this process would be iterative: to determine the initial boundary of regression and the non-linear regression itself.

The second option is to look for the number of heat waves that is needed for nonlinear regression that will no longer be affected by this phenomenon. For such a study I chose to add white Gaussian noise (`awgn` function in MATLAB, signal to noise ratio SNR = 50 dB, type 'measured') to the calculated numerical temperatures, which corresponded to real measured temperatures from IR camera (for experimentally measured data, the average SNR is 48.9 dB). I evaluated the noisy data for different number of heat waves and observed deviation from the correct value determined by the analytical solution. A typical dependence of relative error

$$\text{Er} = \frac{h_{\text{found}}}{h_{\text{set}}} \cdot 100\% \quad (4.52)$$

on the number of heat waves involved in non-linear regression for very high values of heat transfer intensity is shown in Fig. 4.16.

If I set a limit from which the relative error for experimental measurements is acceptable (e.g. 0.1%, 1%, 2%), it is possible to prepare dependencies of the minimum number of measured



■ **Figure 4.16:** Dependence of relative error  $E_r$  on the number of heat waves that were included in nonlinear regression for very high heat transfer intensity,  $h_{\text{set}} = 7000 \text{ W}/(\text{m}^2 \text{ K})$ .

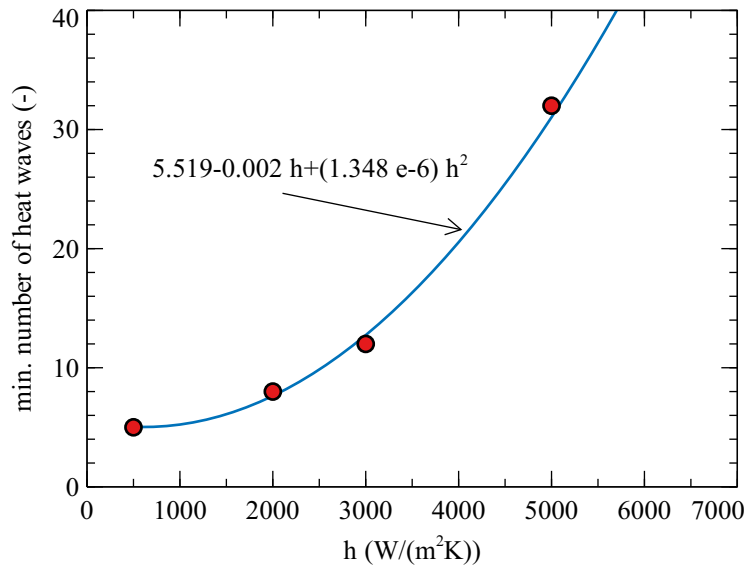
and processed waves to meet this limit for individual heat transfer intensities. These points can then be interleaved with a function and used to easily calculate the minimum number of heat waves to minimize this phenomenon.

As we can see, this dependency can be interleaved by a polynomial function, e.g.

$$\text{NOHW} = 5.519 - 0.002h + 1.348 \times 10^{-6}h^2 \quad (4.53)$$

which theoretically means that the minimum number of heat waves (NOHW) for this measured wall is 5 and increases with increasing heat transfer coefficient (for this case with a considered deviation of 1%).

The minimum number of heat waves is also dependent on the capacity of the system, especially the thickness of the measured wall. This dependence is therefore not universally valid and a new dependence of the minimum number of heat waves should be established for each measured wall.



■ **Figure 4.17:** Minimum number of waves for relative error level less than 1% and for thermophysical properties of measured wall made of mat. 1.4301 and wall thickness  $\delta = 1$  mm. The data is fitted with a polynomial function.

## 4.5 Technical equipment

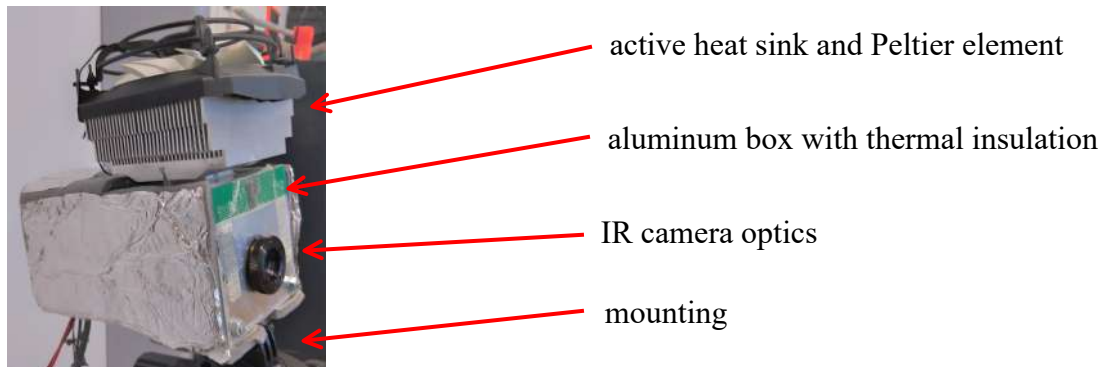
The temperature oscillation method needs to generate sinusoidal modulated heat flux and precisely synchronized triggering of the IR camera at perfect time intervals for its function. To generate these two signals I use the BK Precision 4052 dual-channel function generator with internal triggering. In the first channel, a sinusoidal modulated voltage signal is generated in the range of 3 – 10 V and a rectangular signal in the range of 0 – 3 V is generated in the second channel, which is connected to the IR camera and controls its shooting.

The sine modulated signal is connected to the JS\_2K0-2K0\_NV power supplies (BKE, 1.6 kW, 230 V AC input, 20-200 V DC output) that supply electric power to the halogen flood lights. I use several (depending on experiment) 500 W halogen flood lights to generate the heat flux. Due to their very poor efficiency, most of the electric power supplied is transformed into heat and radiated to the measured wall and so we supply heat flux through radiation. I also tried special red halogen tubes during the experiments, but I didn't notice any significant improvement in the results.

I used the TIM 160 IR camera (MicroEpsilon) with a spatial resolution of  $160 \times 120$  points to measure the surface temperature at individual measuring points. This microbolometric camera works on the principle of measuring the temperature change of the bolometric units and thus, in principle, it is heated by its own operation. Unfortunately, heating the camera also results in a change in measured temperatures and should be recalibrated with its own internal calibration procedure (the so-called Flag function) before every single measurement and the camera temperature change during measurement cannot be determined.

To ensure the smallest possible change in the measured temperature, I have designed a

cooling box for IR camera. The aluminum box is equipped with a Peltier element on the top of the box with a 55 W cooling capacity and an active heat sink on the hot side. The box walls are insulated with thermal insulation and a small fan is installed inside to ensure homogeneous temperature throughout the box.



■ **Figure 4.18:** Photo of IR camera in cooling box.

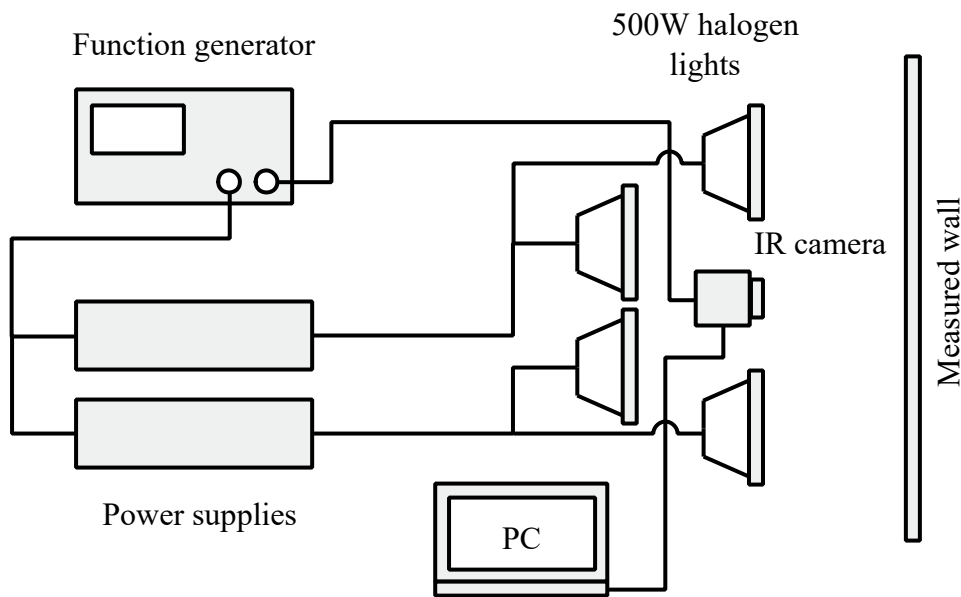
It is necessary to set the temperature of the IR camera and the box before the measurement, which takes approximately 2 hours. With the cooling box, the temperature of the IR camera can be rapidly reduced to improve its digital noise and also maintain a constant temperature of around 5 °C. When measuring an object with the same and homogeneous temperature (straight wall with matt black paint kept at a constant temperature), we found a standard deviation of the measured temperature 0.121 K by a non-cooled camera and the 0.074 K deviation was measured with an active cooling of the IR camera, which is an improvement of approximately 39%.

In experiments I found that the method does not need calibration, but that my 500 W halogen floodlights, due to their own thermal capacity, delay after the control signal in the order of hundreds of milliseconds. If I ignore this phenomenon, I would make a systematic error. I have tried several methods to determine the delay of our lights, including comparing the measured data with the literature (see Experimental validation).

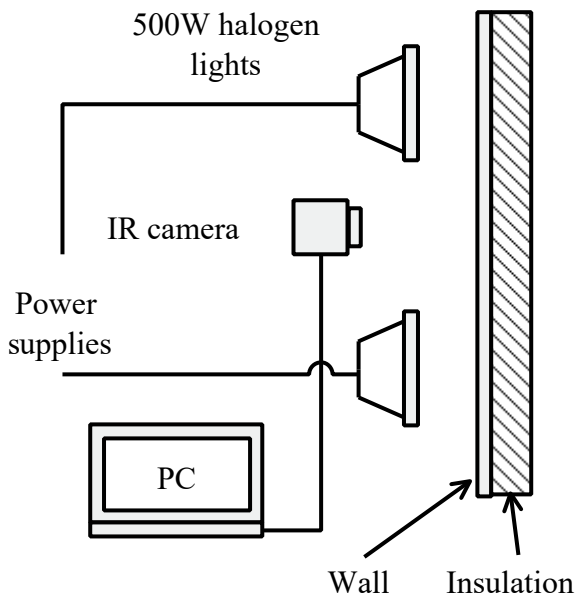
I first tried the zero heat transfer method. I insulated the measured wall from one side with a 100 mm thick polystyrene plate and assumed that such a high thermal resistance simulates the same boundary condition as  $h_{\delta} = 0$ . Then I performed classical measurements with the same settings as in the experiments and evaluated the temperature delay on the body surface. With this procedure, I determined that the halogen lights had a delay of approximately 230 ms, which corresponds to a phase delay time of approximately 8.3 degrees at a heat wave period of 10 s. The scheme of this experiment is shown in Fig. 4.20.

Unfortunately, I repeated the experiment after some time when the halogen lights were in use and found that the delay of the lights increased. This means that the light sources "age with time" and it is therefore necessary to measure the synchronization delay from time to time or replace the halogen bulbs. Perfect results are achieved by synchronizing measurements before each experiment.

For the second method I assumed that this system is first order and so its delay can be calculated from the measured response to the step function. In this case, I was using a speed



■ **Figure 4.19:** Schematic drawing of the experimental equipment used for 4 halogen lights experiments.



■ **Figure 4.20:** Schematic drawing and photo of a synchronization experiment where the right side of the wall is thermally insulated and represents the boundary condition  $h_8 = 0$ .

camera (with appropriate optics and light shielding) to directly scan the halogen lamp and watch it switching on and off. Based on the assumption, it is then possible to calculate the delay from the time constant of such a system. This method showed practically the same results

(slightly higher, about 235 ms) as the zero heat transfer method and also confirmed the “aging” of halogen lamps.

This time (and also phase) delay is then used in the evaluation to correct the measured results, I call it the synchronization phase lag. Otherwise, the measurement would be subject to a systematic and relatively large error.

However, this systemic or synchronization delay is not dependent on the length of the heat wave period that we send to the measured wall. In Solnař et al. (2018b) we tried different periods of transmitted signal (2, 5, 10 and 20 s) with basically the same result.

I also measured the shape of a sine wave that is generated in halogen floodlights. For this experiment, I assumed that the intensity of light would be accompanied equally proportionally by the intensity of heat flux, so I prepared an experiment to measure the intensity of light. The photoresistor was directed perpendicularly to the halogen light and sensed the intensity of light at a frequency of 1 kHz. The measured shape corresponds very well to the sine wave, so I assume that this factor has no significant effect on the results.

## 4.6 Experimental validation

I validated the TOIRT method on probably the best-known experiment of measuring heat transfer, fluid flow in a tube. In this case the flow in one direction prevails (radial and tangential direction also occurs, but it is minor). This experiment has been measured many times by many researchers and has also been confirmed by papers in the literature and the most frequently cited correlation is Gnielinski’s correlation, which is very often complemented by Hausen’s correction for short tubes

$$\text{Nu} = \underbrace{\frac{(f/8) \text{RePr}}{1 + 12.7 \sqrt{f/8} (\text{Pr}^{2/3} - 1)}}_{\text{Gnielinski}} \underbrace{\left[1 + (d_i/l)^{2/3}\right]}_{\text{Hausen}} \quad (4.54)$$

where  $f$  is the friction factor which can be expressed for smooth tubes as

$$f = (1.8 \log_{10} \text{Re} - 1.5)^{-2}. \quad (4.55)$$

valid for  $10^4 < \text{Re} < 10^6$ ,  $0.1 < \text{Pr} < 1000$  and  $d_i/l \geq 1$  (VDI Heat Atlas (2010)).

Gnielinski’s correlation has also been reviewed and re-tested several times e.g. Taler (2016) used the same correlation equation and for the narrower range of Reynolds number  $4300 < \text{Re} < 12000$  specified the individual constants in the original equation.

Another very often seen correlation, which is also much simpler, is the correlation of the authors Dittus and Boelter (or sometimes called McAdams), which does not take into account the development of the temperature profile since the beginning of the heating zone (measurement zone) but only the integral value over the whole measured area.

$$\text{Nu} = 0.023 \text{Re}^{0.8} \text{Pr}^n, \quad (4.56)$$

where  $n$  represents the exponent of the Prandtl number and usually  $n = 0.3$  for cooling and  $n = 0.4$  for heating is considered. This correlation is valid for  $\text{Re} \geq 10000$  and for  $0.7 \leq \text{Pr} \leq 17600$ .

My validation experiment was made in a closed water loop of about 50 liters, which was driven by a centrifugal pump (Ebara 1.5 kW, controlled by a Siemens Sinamics G120 frequency converter). The water was pumped into a stainless steel pipe ( $32 \times 1.5$  mm,  $d_i = 32$  mm, mat. EN 1.4307, density  $\rho = 7900$  kg/m<sup>3</sup>, thermal conductivity  $k = 15.2$  W/(mK) and specific capacity  $c_p = 501$  J/(kgK)), which was 2 m long and thermally insulated with foam insulation to the beginning of the measuring section (1.7 m). The output of the measuring section was connected to an induction flow meter (Krohne OptiFLUX 5000) and a tank where the water temperature was measured by a Pt 1000 sensor. A schematic drawing and photo of validation experiment can be seen in the Fig. 4.21. Further details can be found in Solnař et al. (2019) or Dostál et al. (2018). These results also served as validation tests for other articles, e.g. Solnař et al. (2018a).

The stainless steel tube was sprayed in the measuring section (200 mm) with a black matte paint to increase and more constant emissivity of  $\varepsilon = 0.96$ . At the tube, we started a measuring section up to 1.7 meters to stabilize the hydrodynamic profile, and in addition to the measuring section, I added thermal insulation to ensure that the temperature profile developed at the beginning of this section. I used heat waves with several periods and various frequency of temperature field scanning.

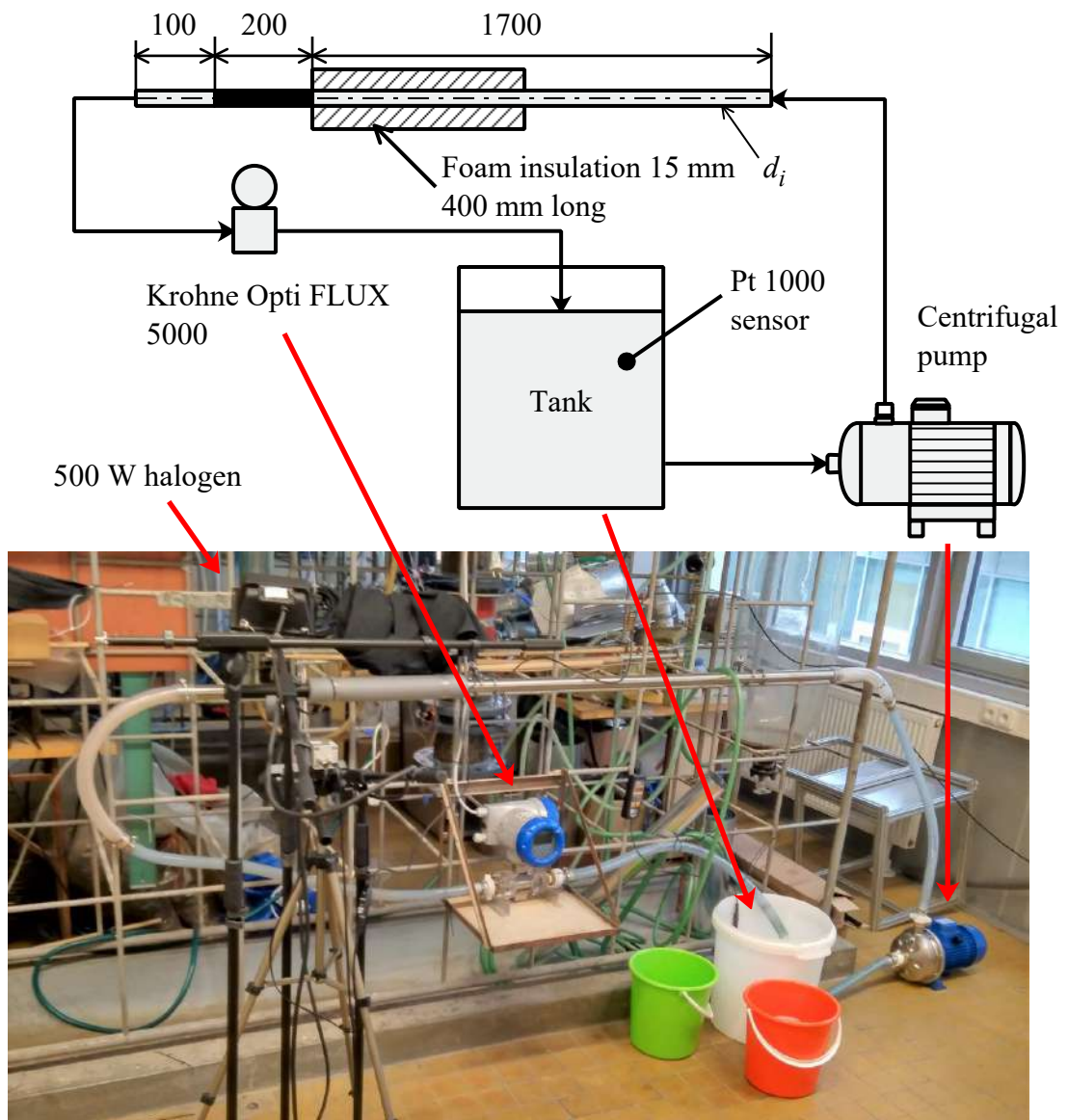
From the measured data with an IR camera with a spatial resolution of  $160 \times 120$  measured points, I chose only a bar that was perpendicular to the camera lens. Due to the reflections illuminated from the tube into the lens and other circumstances, I selected only a part of the recorded area, thus obtaining an investigated area that was  $160 \times 5$  points. Halogen lights were aimed at the tube from above and below the camera at an angle of about 45 degrees and distance about 250 mm.

Locations where the incident light is reflected into the camera cannot be evaluated because they do not allow correct evaluation. These places show much lower local values of the heat transfer coefficient (reflected light into the lens appears in the IR camera as a place with significantly higher temperature and there are no detectable oscillations), so I omit them from data recording and evaluate only other places where this light reflection does not occur. This problem occurred only on rounded surfaces, on straight measuring walls this problem did not occur, or I was able to eliminate it completely by suitable positioning of the lights.

The water flow, which was measured by an induction flow meter, was used to calculate the Reynolds number according to Eq. (1.7) and thermophysical properties were taken from the Šesták et al. (1996). The Reynolds number range for this experiment was between 12 000 and 25 000, thus it is ensured a fully turbulent flow. During one measurement, the water temperature in the tank increased due to dissipation of the pump energy and heating from the outside by radiation. The heating was mostly 0.3 K during one measurement, so I took the arithmetic mean of the temperatures at the beginning and at the end of the measurement. The obtained heat transfer coefficients are recalculated to Nusselt numbers according to Eq. (1.5) where I substitute the inner diameter of the pipe for the characteristic dimension. Overall Nusselt numbers  $\overline{Nu}$  are taken as a mean value of the local values, see Eq. (1.12). For the calibration experiment, I measured 7 different water flows and repeated the experiment 7 times, altogether 49 measurements.

The measured data and comparison with known correlation relations can be seen in Fig. 4.22.

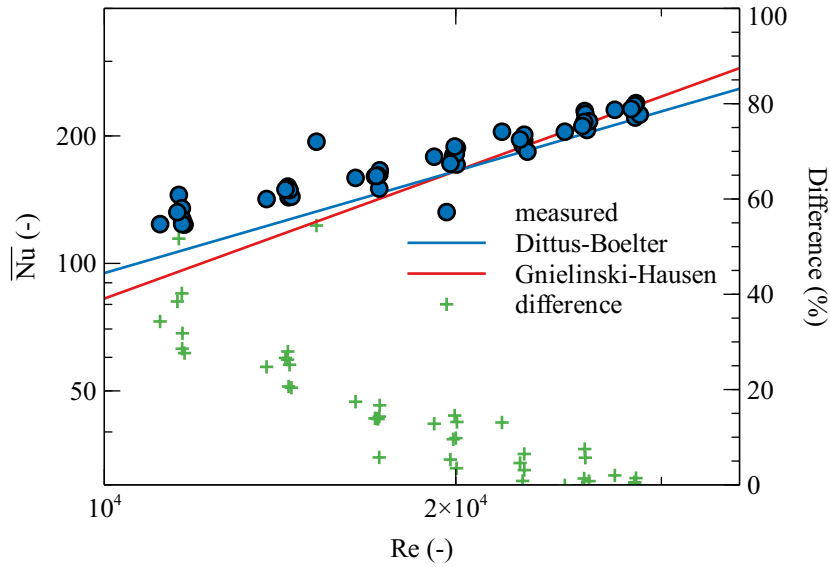
From the comparison of the data I can say that for higher Reynolds numbers ( $Re \geq 20000$ )



■ **Figure 4.21:** Schematic drawing and photo of a fluid flow experiment in a closed water loop tube driven by a centrifugal pump.

I have relatively good match of our data with both mentioned correlations. For lower Reynolds numbers, the TOIRT method predicts higher Nusselt numbers, by approximately 40%, this may be due to an insufficient length of the pipe and thus to an imperfect stabilization of the hydrodynamic profile in the pipe.

I also tried to solve the "reverse" task and set the synchronization delay so that the correlation of Gnielinski (with Hausen correction) perfectly fits our measured data. In this way, I have recalculated the system time delay (and hence the phase delay) of about 380 ms. Since the measurement of the water flow in the pipe took place after some other measurements, the idea of



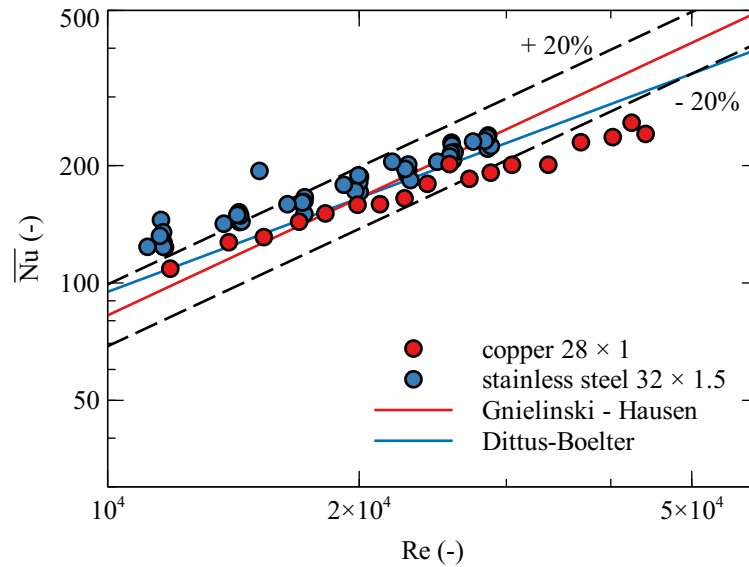
■ **Figure 4.22:** Comparison of experimental data when measuring flowing water in a tube in turbulent mode with correlations by Gnielinski (with Hausen correction for short tubes) and Dittus and Boelter. ( $25 \times 10$  sec waves, 10 Hz)

halogen lights aging is confirmed and it is necessary to perform synchronization measurements from time to time, or better before each series of experiments.

For the purpose of validation, I performed the same experiment for a pipe of different material and dimension. For the second experiment, I used a  $28 \times 1$  mm copper tube ( $d_i = 26$  mm, density  $\rho = 8941 \text{ kg/m}^3$ , thermal conductivity  $k = 395 \text{ W/(mK)}$  and specific capacity  $c_p = 386 \text{ J/(kgK)}$ ), which, like the stainless steel tube, was coated with a thin matt black coating 200 mm long at a distance of 1.7 meters from the beginning of the tube. The connection of the experiment and the technical means used are the same as in the experiment with the stainless steel tube.

In comparison, we can see that the values measured on a smaller copper tube are very well comparable to those on a stainless steel tube, although we can see a slightly different tendency of the Nusselt number on Reynolds number. Thus, the oscillation method is relatively well applicable to different materials and different dimensions of the measured walls of the experiment.

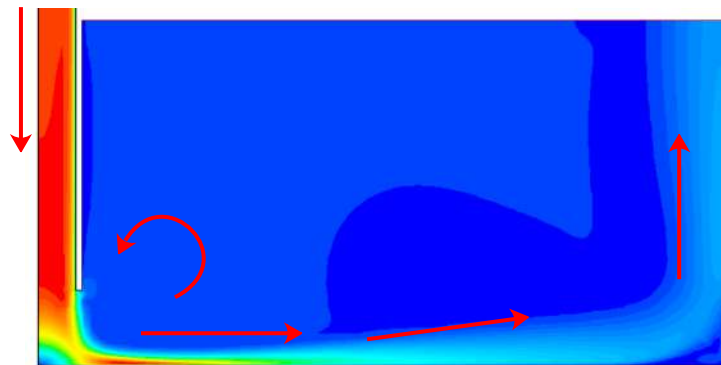
From a validation test on an experiment where flow in one direction predominates, I verified that the method is applicable with a reasonable error. For higher values of the heat transfer coefficient, the insensitivity and error of the method increases very quickly and so I consider the average deviation in the order of percent and the maximum deviation around 40% as very good. I have also shown that changing the material or dimensions of the measured experiment does not have a major effect on the results, so the method is applicable to different materials. The heat transfer in the pipe is quite high and so I expect to reduce the deviation from the literature results for other geometries.



■ **Figure 4.23:** Comparison of mean values of Nusselt number in water flow in pipe for two different pipes (material and size) with Gnielinski correlation. The dashed line indicates deviations of  $\pm 20\%$  from the correlation and we can see that most of the measured points lie in this band. (both  $25 \times 10$  sec waves, 10 Hz)

## 4.7 Impinging jets

In the next step I applied the method to more complicated flow. Impinging jets are very often seen in practice when locally cooling components or pumping mixing, and there is a lot of work on this subject in the literature. When the liquid flows out of the nozzle and hits the target wall, the flow is reversed and continues along the wall, resulting mainly in a two-dimensional flow.



■ **Figure 4.24:** 2D axisymmetric CFD model of fluid flow in the vessel with impinging jet, see Solnař (2016). The figure shows 2D flow, which is generated by reversing the current that falls on the wall.

One of the most cited works when talking about the heat transfer between an impinging jet and a smooth wall is Lytle and Webb (1994). Authors carried out this experiment measuring

the heat transfer with air for various geometrical arrangement of the distance of the nozzle from the wall in the range  $(z/d) = 0.1 - 6$ . In their work, they presented only the dependence of the Nusselt number on Reynolds. For the average value of the Nusselt number they reported

$$\overline{Nu} = 0.424Re^{0.57} (z/d)^{-0.33} \quad (4.57)$$

for a range of distances  $(z/d)$  of 0.1 to 1, Reynolds numbers  $3600 \leq Re \leq 27600$ , and also for an averaged range  $(r/d) = 1$ . For a larger averaged area  $(r/d) = 2$  they then reported

$$\overline{Nu} = 0.150Re^{0.67} (z/d)^{-0.36} \quad (4.58)$$

and we can say that the area over which we average the Nusselt number has a great influence on both the geometric constant and the exponent of the Reynolds number. Authors also presented a correlation for the so-called stagnant point, a place with a radial coordinate  $(r/d) = 0$

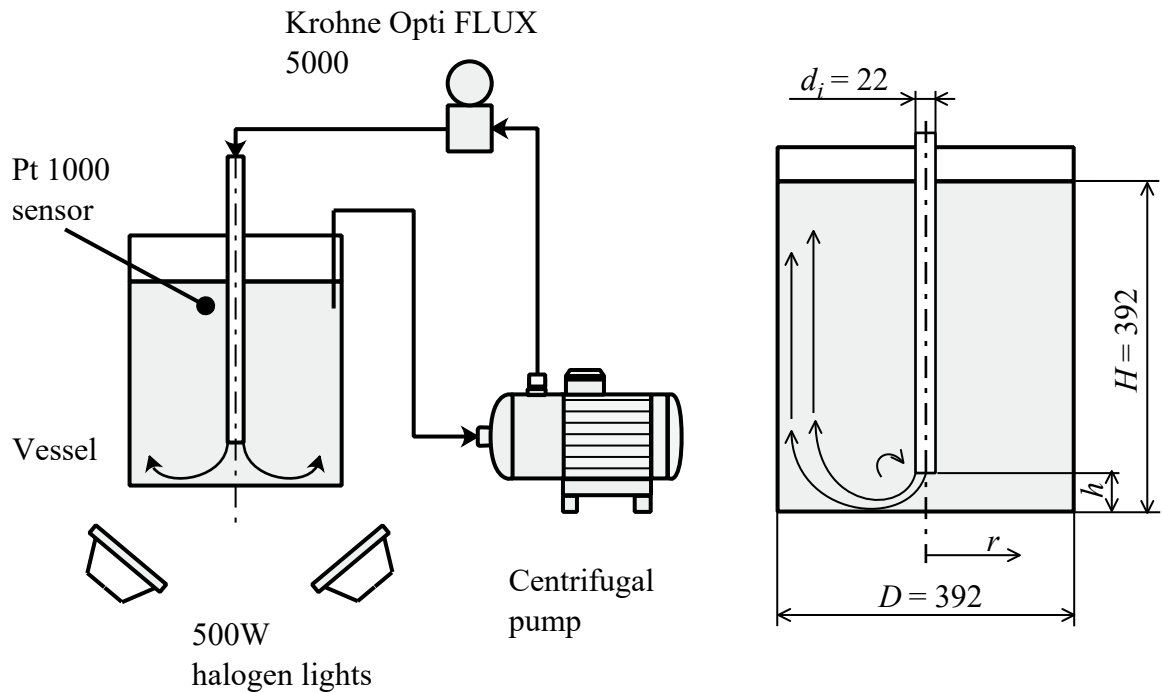
$$Nu_0 = 0.726Re^{0.53} (z/d)^{-0.191} \quad (4.59)$$

Many other authors measured similar or the same geometry and also added radial shapes of the Nusselt number such as Katti and Prabhu (2008), Katti et al. (2011) or Persoons et al. (2013) to the correlations or correlated the measured Nusselt numbers with other correlation relationships. Work that should be mentioned when dealing with the heat transfer in the impinging jet is Zuckerman and Lior (2006), who has done a very long and detailed review of the literature that deals with this. Authors assessed the experimental, analytical and numerical approach and summarized a large number of measured correlations.

My experimental measurements of the heat transfer coefficient between the smooth wall and the impinging water jet were performed in a flat bottom vessel with diameter of 392 mm, where the water level was set as the diameter of the vessel. The closed water loop was driven by a centrifugal pump (Siemens 0.85 kW, controlled by a Siemens Sinamics G120 frequency converter) and the flow rate was measured by an induction flow meter (Krohne OptiFLUX 5300). The pump was connected by hoses to the flowmeter and to an aluminum tube  $25 \times 1.5$  mm ( $d_i = 22$  mm and corresponding length  $L = 45 d_i$ ) which was attached to a rigid steel frame on a cylindrical vessel. The bottom of the container was made of stainless steel (mat. EN 1.4301,  $\delta = 0.99$  mm, density  $\rho = 7900$  kg/m<sup>3</sup>, thermal conductivity  $k = 15.2$  W/(mK) and specific capacity  $c_p = 501$  J/(kg K)) and is attached and sealed to the plastic container by screws. The water level was constant because the pump was drawing water from the vessel. The water temperature in the vessel was measured with a Pt1000 thermometer at the water level around the tube.

The outer side of the flat bottom was provided with a thin matt black coating for constant and higher emissivity, same as previous experiments. The heat waves were supplied by a trio of 500 W halogen floodlights, which were distributed around the bottom evenly over 120 degrees, altogether approximately 1500 W of heat power. During the measurement we used heat flux waves with a period of 10 seconds and 10 Hz surface temperature scanning.

The IR camera scanned the entire bottom of the vessel (with construction), but not all the measured points correspond to the measured wall. Of all the temperatures measured, only those



■ **Figure 4.25:** Schematic drawing of an experiment measuring the heat transfer coefficient between a smooth wall and an incidental impinging water jet in a flat-bottomed cylindrical vessel.

that corresponded to the surface of the measured vessel bottom were selected. The rest of the values (supporting structures, screws, sealing, etc.) were ignored and not evaluated.

The measured water flows were used to calculate the Reynolds number according Eq. (1.7), where the thermophysical properties of the water were taken from the Šesták et al. (1996) for the corresponding temperature measured by the Pt1000 sensor. During one measurement, the water inside the vessel heats up (by about 0.2 K), thus we take the temperature as the arithmetic mean of the temperature at the beginning and end of the measurement.

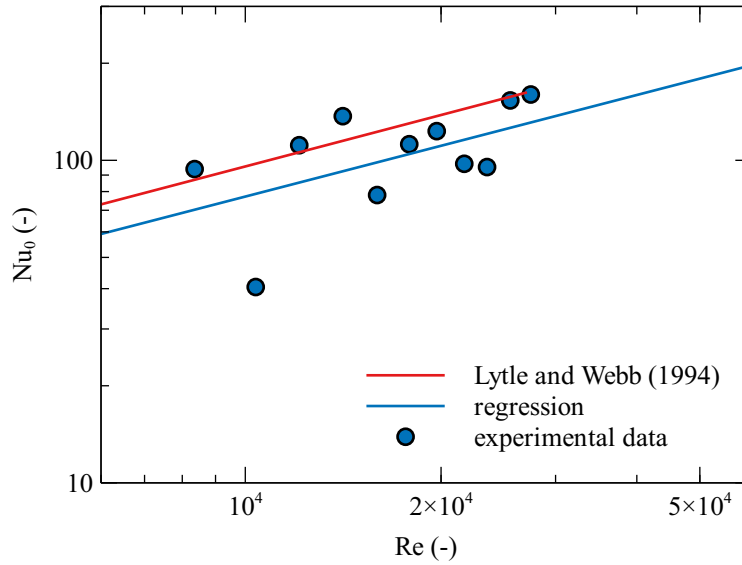
After processing the measured data, I obtained heat transfer intensity maps  $h(x, y)$  for each measured volumetric flow rate. The heat transfer coefficients were recalculated to Nusselt numbers according to Eq. (1.5), where we replaced the characteristic dimension with the inner diameter of the pipe  $d_i$ .

Firstly, I correlated measured values of the Nusselt number at a stagnant point (at the radial coordinate  $(r/d) = 0$ ) by the dependence presented by Lytle and Webb (1994). My correlation was determined by the least squares method and is

$$\text{Nu}_0 = 0.624 \text{Re}^{0.5231} \text{Pr}^{0.4} \quad (4.60)$$

which is very close to the correlation published by Lytle and Webb (1994) (in terms of geometric constant and exponent of Reynolds number). A graphical representation of the measured data and correlations can be seen in Fig. 4.26.

From the results it can be assumed that the tendency of the Nusselt number to Reynolds



■ **Figure 4.26:** Experimentally measured Nusselt numbers for stagnant point ( $r/d = 0$ ), regression and comparison with correlation relationship from Lytle and Webb (1994).

corresponds to the results from Lytle and Webb (1994), but our prediction of Nusselt number is lower. The regression curve describes our measured values with a maximum error of about 25%.

The second regression was performed for the average values of the Nusselt number  $\overline{Nu}$  according to Eq. (1.12) which were taken from the whole measured area, i.e. about  $(r/d) = 9$ , and we compared this dependence on Reynolds number with the correlation relations from Lytle and Webb (1994). The determined correlation for the averaged Nussel numbers is

$$\overline{Nu} = 0.164 Re^{0.67} Pr^{0.4} \quad (4.61)$$

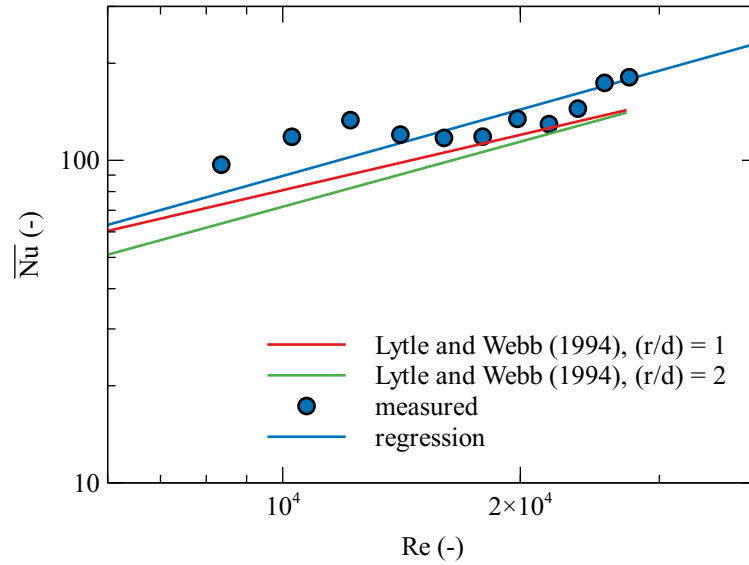
and graphical comparison of the measured values can be seen in the Fig. 4.27.

From the comparison we can conclude that the tendency of dependence is again very similar, the geometric constant is very close and also the data do not have such variance around the correlation line. In terms of the area over which we averaged the Nusselt number, it is better to compare with the correlation of Lytle and Webb (1994) for their area  $(r/d) = 2$ .

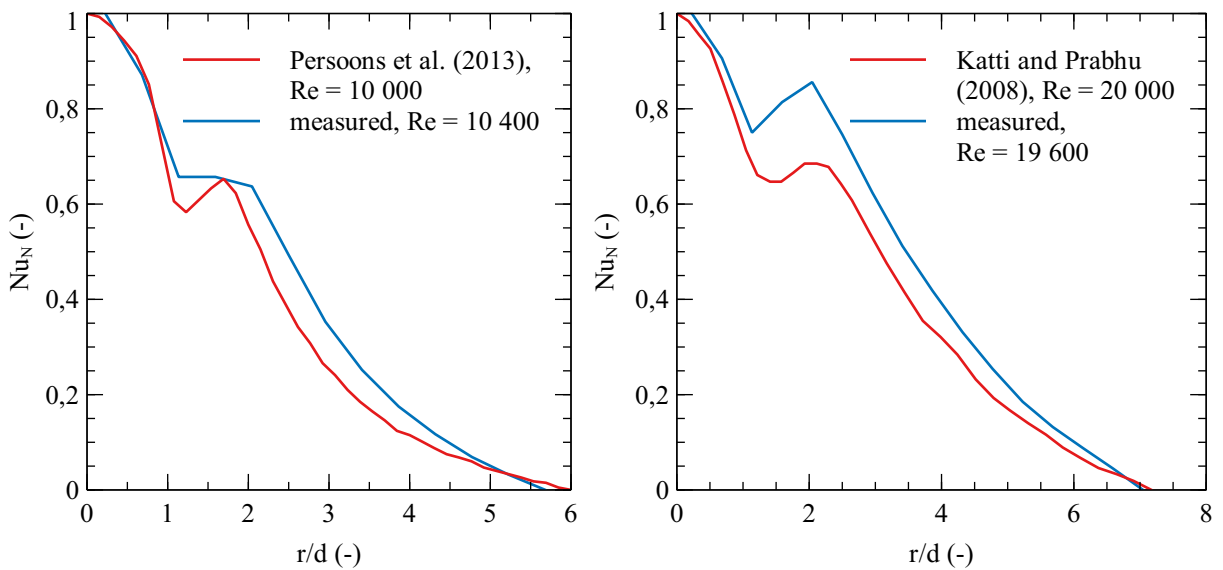
Perhaps the most interesting and most frequently observed result is the local values of the Nusselt number depending on the dimensionless radial coordinate  $(r/d)$ . I compared my radial curves with two literary sources namely Katti and Prabhu (2008) and Persoons et al. (2013) and the results can be seen in the Fig. 4.28. Since I do not have data for exactly the same Reynolds numbers, I decided to compare the normalized Nusselt numbers according to

$$Nu_N = \frac{Nu - \min(Nu)}{\Delta Nu} \quad (4.62)$$

and I assume that in a relatively small range of Reynolds numbers, the shapes of the Nusselt numbers will not vary much, and so believe that normalized values are comparable (see Fig. 4.28).



■ **Figure 4.27:** Comparison of mean values of Nusselt number in dependence on Reynolds for averaged area ( $r/d = 9$ ) and with correlation relations from Lytle and Webb (1994).

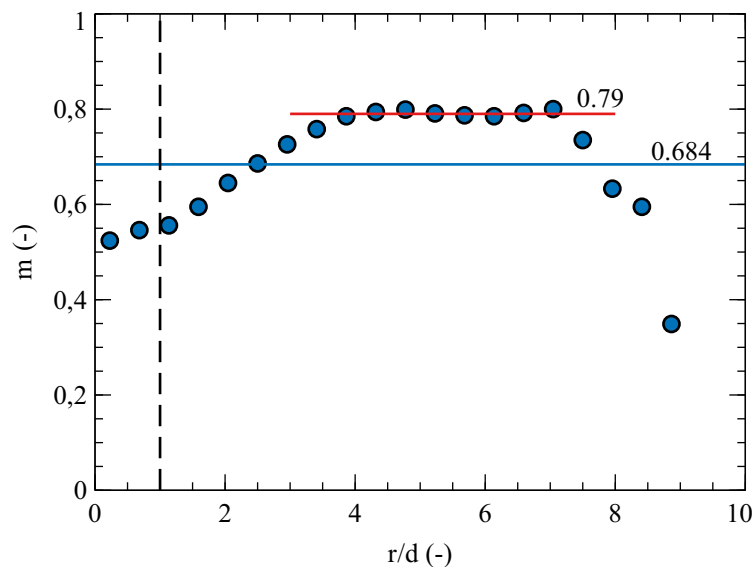


■ **Figure 4.28:** Comparison of dependencies of normalized Nusselt numbers on dimensionless coordinates ( $r/d$ ) with Persoons et al. (2013)-left and Katti and Prabhu (2008)-right.

By plotting the local value of the Nusselt number (its normalized form) as a dependence of the dimensionless radial coordinate ( $r/d$ ), it is obvious that the shape of this dependence is the same or very similar. When comparing for lower Reynolds numbers (Re about 10 000, comparison with Persoons et al. (2013)) we see a very good match between our data and literature. When comparing with higher Reynolds numbers (Re about 20 000, comparison with Katti and Prabhu (2008)) the shape of the Nusselt number is very similar, but my data show higher local values of Nusselt number in the area ( $r/d$ ) from 1 to 3 than literature, but the local maximum

still occurs in the same place.

Finally, I plotted the exponent of the Reynolds number  $m$  as a dependence on the dimensionless coordinate ( $r/d$ ) (see Fig. 4.29). The exponent can tell what flow we can expect at this coordinate. At a stagnant point, the exponent approaches 0.5, which is mostly associated with laminar flow, then increases to 0.8, which is mostly associated with turbulent flow along a wall. Finally, at the edge of the vessel, the exponent decreases, this is most likely associated with a slowing of the fluid flow due to the wall and changing the flow direction. The figure also shows the value of  $m$  for which the correlation for the average values of the Nusselt number was calculated.



■ **Figure 4.29:** Reynolds number exponents  $n$  as a dependence of dimensionless radial coordinates ( $r/d$ ). The black dashed line represents the edge of the inner diameter from which the impinging jet flowed.

Values of the heat transfer coefficient I expected are lower in this geometry, which proved true and also the deviation of my values from the literature is very small. My experimental results are very consistent with the literature in both the correlations and local values of the Nusselt number. The TOIRT method seems to be suitable for measuring such geometries where there are more major flows.

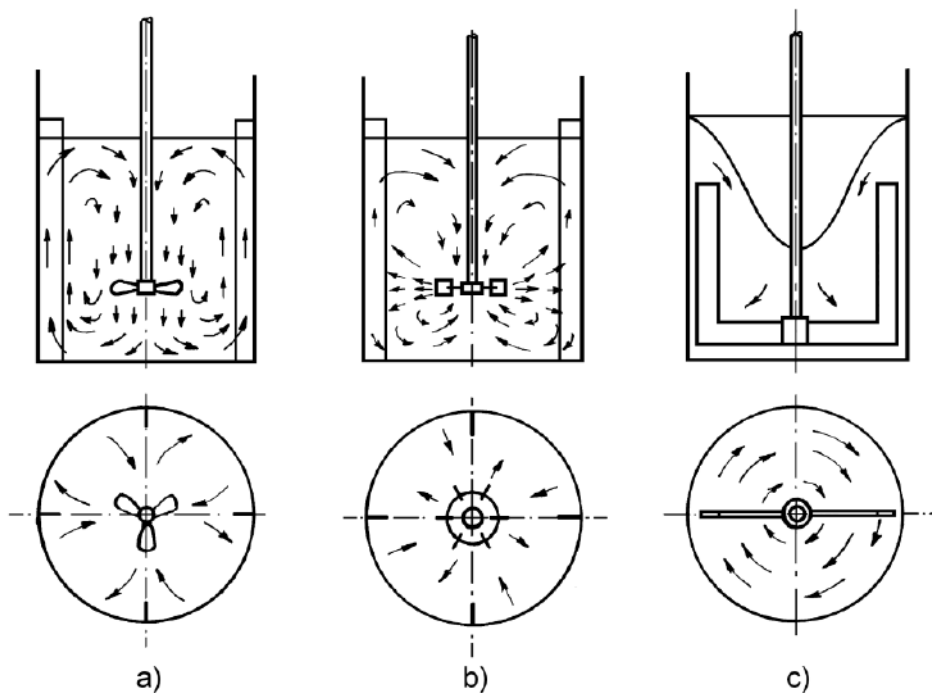
The shape of the Reynolds number exponent  $m$  shows that in the axis of the task the fluid falls perpendicular to the plate. Farther from the center, the exponent rises to the value we know from the turbulent flow along the wall. It decreases at the edge of the vessel, which is most likely associated with the upward rotation of the flow. The assumption of flow is verified there and TOIRT method is suitable for this geometry.

During the experiments I also changed the settings of oscillations (heat flux value, sine period, number of heat waves) and changing the settings had no effect on the resulting data.

## 4.8 Vessels equipped with agitators

Vessels equipped with agitators are probably the most frequently seen equipment in the process industry after pumps and heat exchangers. These apparatuses are primarily intended to prepare homogeneous mixtures or heterogeneous with the same concentration in the batch, but can also be used as heat exchangers. Particularly in the duplicator or in the tubular baffles inside the agitated vessels it is possible to exchange heat with another medium. For these reasons too, values (mostly only overall) of heat transfer coefficients in such apparatuses were very often measured in the past. There are a myriad of papers on this subject in the literature that also carry a huge number of different correlations and different geometries that have been experimentally measured.

However, the fluid flow in the vessel with impeller is very complex. For two basic operations (mixing and dispersing) two basic types of agitators, axial and radial, are used. However, neither of those perfectly creates an axial or radial flow, and there are always other streams present in the fluid. In addition, a tangential flow (mostly limited by baffles, but not perfectly) is also produced during the agitator operation, thus creating a 3D flow in the vessel.



■ **Figure 4.30:** Streamlines for basic mixer types: a - axial, b - radial, c - tangential, see Rieger et al. (2005)

In the literature we usually find the basic correlation (see Eq. (1.11)) which is also very often supplemented with other information such as viscosity ratio, influence of impeller eccentricity, influence of baffles etc.

Many correlations can be found in the literature for various agitated systems, only some of which are in the formula of Eq. (1.11) are listed in Tab. 4.2.

■ **Table 4.2:** Correlation for Nusselt number according to Eq. (1.11) for different agitators and different measuring positions - B bottom, b baffles, W wall, O overall. Note: 3PBT45 three-pitched-blade turbine (45° angle), CBT curved blade turbine, A315 axial impeller, RT Rushton turbine, DHR double helical ribbon, CHS centered helical screw. Methods: EDD electro-diffusion method, D dynamic method, S stationary method

loc.	$C$	$m$	$n$	$Re_M \times 10^4$	agitator	method	Ref.
B	0.3031	0.7559	1/3	6-9.4	CBT+3PBT45	EDD	Věříšová et al. (2015)
B	0.7733	2/3	1/3	7.5-9.8	CBT+4PBT45	EDD	Věříšová et al. (2015)
b	0.54	0.675	1/3	1.9-11.2	6PBT45	D	Dostál et al. (2010)
W	0.327	0.67	1/3	2.3-7	RT	EDD	Cudak and Karcz (2008)
W	0.27	0.67	1/3	2.3-7	A315	EDD	Cudak and Karcz (2008)
W	0.35	2/3	1/3	0.5-8	DHR	S	Ishibashi et al. (1979)
W	0.65	0.6	1/3	0.1-2.5	CHS	S	Ishibashi et al. (1979)
W	0.146	0.73	1/2	0.3-8.5	RT, no baffles	S	Kupčák (1974)
B	0.671	0.52	1/2	0.3-8.5	RT, no baffles	S	Kupčák (1974)
O	0.196	0.69	1/2	0.3-8.5	RT, no baffles	S	Kupčák (1974)
W	0.058	0.76	1/2	0.6-20	2PBT44	S	Kupčák (1974)
B	0.217	0.62	1/2	0.6-20	2PBT44	S	Kupčák (1974)
O	0.071	0.74	1/2	0.6-20	2PBT44	S	Kupčák (1974)

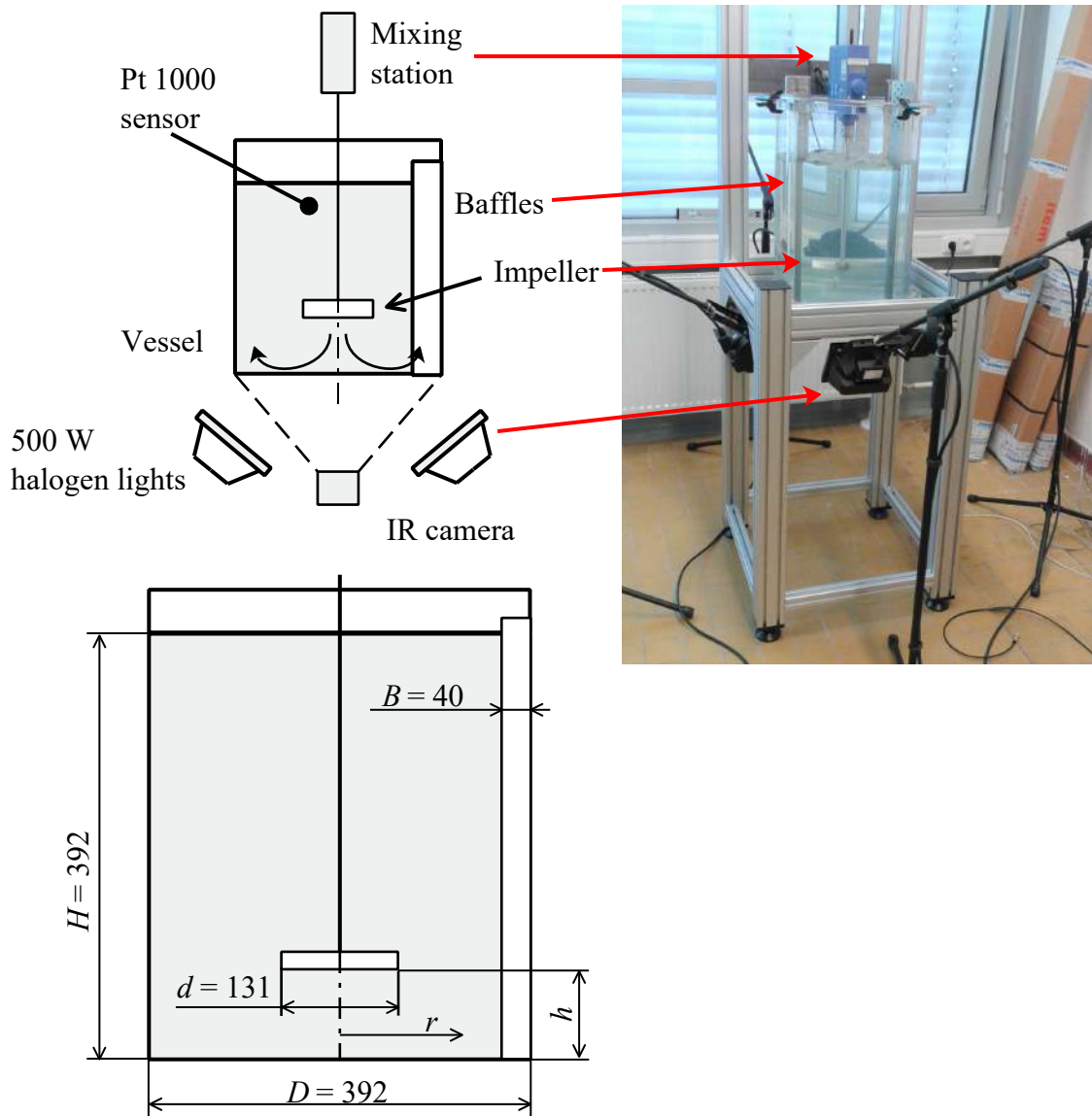
For this geometry I chose mixing Reynolds number according to Eq. (1.8) and to calculate the Nusselt and Prandtl numbers I used (1.5) and (1.9).

From Tab. 4.2 we can see that the expected values of geometric constant  $C$  are in the order of tenths, the exponent of mixing Reynolds number is usually 2/3 or very similar value and the exponent of Prandtl number is usually 1/3.

#### 4.8.1 Bottom of vessels with agitators

My measurements were performed in a  $D = 392$  mm flat bottom Plexiglas container. The bottom was made of stainless steel (mat. EN 1.4301,  $\rho = 7800$  kg/m<sup>3</sup>,  $c_p = 501$  J/(kg K) and  $k = 14.6$  W/(m K)) with a thickness of  $\delta = 0.99$  mm. The outer side of the stainless steel bottom was provided with a very thin matt black coating for an increase in emissivity  $\varepsilon = 0.96$ , which also improved its uniformity. The vessel was filled with water to  $H = D = 392$  mm and waited for its temperature to stabilize with the surroundings. An agitator with a diameter  $d$  was placed on a shaft which was mounted in an adjustable speed mixing station. The height of the bottom of the impeller above the bottom was  $h$ . The vessel was also provided with 4 baffles with width  $B = 0.1D$  that were evenly spaced along the vessel wall. Details of our experimental stand can be seen in the Fig. 4.31. Inside the batch, the temperature of the Pt1000 sensor was also measured to determine the thermophysical properties of the water.

The IR camera pointed from the bottom of the stand perpendicular to the bottom of the vessel at a distance of 750 mm. Since the camera occupied the entire bottom, which was circular, only about 60% of the data was evaluated from the measured scene. The three halogen lights (we also tried 2, 4, and 6) were evenly spaced along the bottom at 120 degrees and angled to illuminate



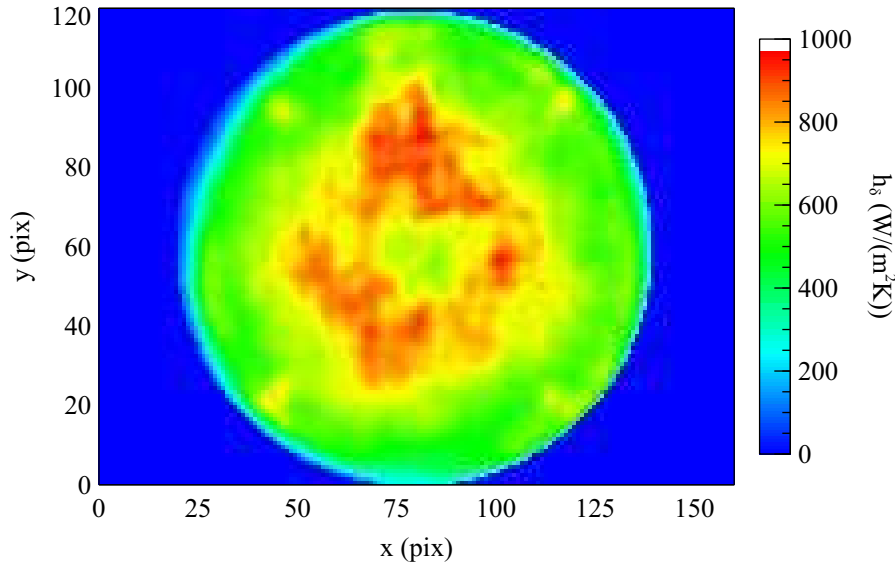
■ **Figure 4.31:** Scheme and photo of an experiment measuring the heat transfer coefficient at the bottom of an agitated vessel.

(and therefore heat) the entire bottom surface. The distance of the edge of the light from the bottom was about 20 mm.

At the beginning of each measurement, the impeller speed was adjusted and maintained by the mixing station. The set rotational speed  $N$  was then used to calculate the mixing Reynolds number (according to Eq. (1.8)). Thereafter, the temperature of the batch was read out by Pt1000 sensor to determine the thermophysical properties of the batch and then the Prandtl number was calculated.

For bottom measurements we used heat oscillations with periods of 5, 10 and 20 s with va-

rious number of oscillations. From the measured data we evaluated the intensity of heat transfer  $h_\delta$  at the bottom of the stirred vessel, see Fig. 4.32.



■ **Figure 4.32:** Distribution of heat transfer coefficient  $h_\delta$  at the bottom of the agitated vessel with four baffles. 6PBT45 axial impeller with  $d = 131$  mm ( $d/D = 1/3$ ), impeller distance from bottom  $h/d = 3/4$ ,  $Re = 2.9 \times 10^4$ . The bottom diameter of the container corresponds to approximately 120 measured pixels.

From the heat transfer intensity distribution, we can see that the largest values of the heat transfer coefficient  $h_\delta$  are below the blades at the end of the impeller. The intensity decreases in the mixer axis. At the edge of the vessel, we can also see an increase in heat transfer due to the baffles and the turbulence of the fluid in this area.

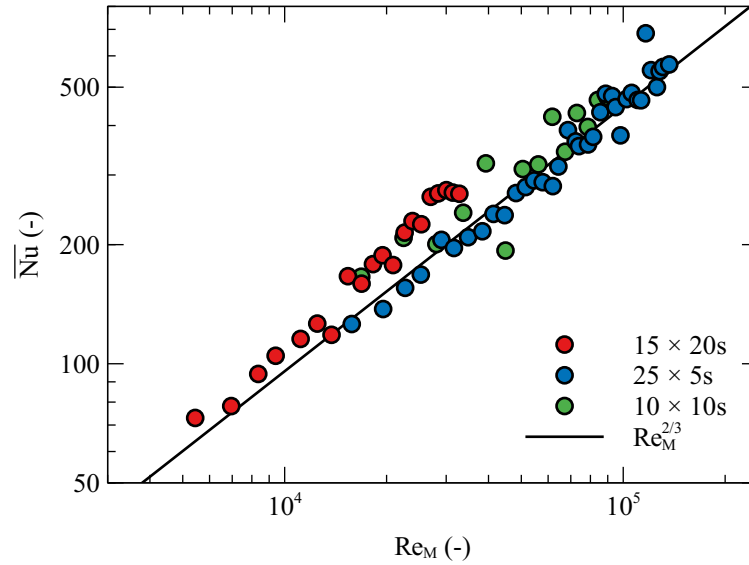
For the preliminary experiments, I chose a typical industrial geometry of the 6PBT45 axial agitator with a diameter  $d = 131$  mm ( $d/D = 1/3$ ), which I placed in height  $h/d = 3/4$  above the bottom of the vessel. For this geometry, I repeated the experiment for various temperature oscillation settings, various Reynolds number ranges, and also for various numbers of temperature oscillations per measurement.

All measured average Nusselt numbers  $\overline{Nu}$  can be seen in the Fig. 4.33, where they are compared with the line that represents  $Re_M^{2/3}$ , which is very often seen Reynolds number power in case of turbulent flow at the bottom of the agitated vessel.

The Fig. 4.33 shows that the measured values of Nusselt numbers are independent of the number on temperature waves or their setting (their period). The results show a very good consistency along  $Re_M^{2/3}$ . My measured values of mean Nusselt number can be interleaved by correlation according to Eq. (1.11)

$$\overline{Nu} = 0.537 Re_M^{2/3} Pr^{1/3}, \quad (4.63)$$

which absolutely agrees with the assumed values of the geometric constant (both Reynolds and Prandtl powers are set according to literature). If we perform a two parametric regression of our



■ **Figure 4.33:** Values of mean Nusselt numbers  $\overline{Nu}$  in dependence on mixing Reynolds number for agitated vessel experiment. Used axial 6PBT45 impeller  $d/D = 1/3$  at height  $h/d = 3/4$ .

data (the Reynolds number power would also be evaluated) we get a correlation

$$\overline{Nu} = 0.502 Re_M^{0.686} Pr^{1/3}, \quad (4.64)$$

which still corresponds very well to the expected values in the correlation.

I also prepared the same experiment for a smaller axial 6PBT45 impeller and monitored the effect on heat transfer coefficients. Impeller with a diameter  $d = 65\text{mm}$  ( $d/D = 0.156$ ) was set to height  $h/d = 3/4$  above the bottom of the vessel. The measured data can then be fitted with one parametric regression according Eq. (1.11)

$$\overline{Nu} = 0.307 Re_M^{2/3} Pr^{1/3} \quad (4.65)$$

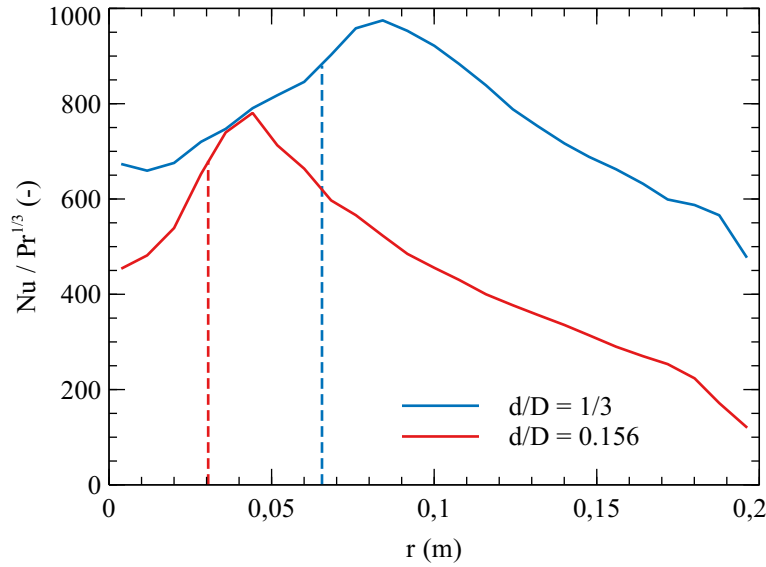
or two parametric regression

$$\overline{Nu} = 0.249 Re_M^{0.682} Pr^{1/3}. \quad (4.66)$$

Both correlations again correspond to the assumed values of the geometric constant  $C$  and the exponent of the Reynolds number  $m$ , so I believe that the TOIRT method is useful for measuring such experiments.

In addition to calculating correlations, this method also allows us to study local heat transfer coefficient values. The knowledge of local heat transfer intensity can help to optimize batch cooling or heating, reducing the size of apparatus and saving resources. One option is to view 2D heat transfer intensity maps (see Fig. 4.32), which may be difficult to recognize. Much more often and more clearly, we find local values depending on the radial distance from axis. For both impellers can we see a comparison of the Nusselt number according to the radial coordinate in the Fig. 4.34.

Comparing the local values of the Nusselt numbers, we can see that the shapes are very similar and that the maximum of the heat transfer intensity is located just behind the end of



■ **Figure 4.34:** Comparison of local Nusselt numbers for both axial impellers in a vessel with baffles, both  $Re = 5 \times 10^4$ . The dashed lines of corresponding colors represent the end of the impeller blades.

the impeller blades. Generally, the heat transfer intensity is higher in an agitated system with a larger impeller.

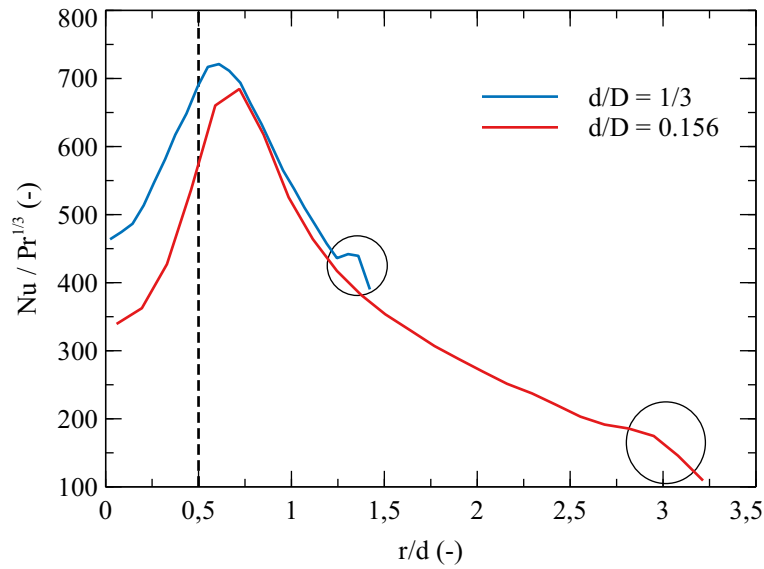
For comparison purposes, it is probably preferable to compare states where the impellers (resp. mixing stations) consume the same wattage than the same Reynolds number. It is also appropriate to introduce a dimensionless radial coordinate  $r/d$  from the axis relative to the diameter of the agitator. The values then become comparable. The power consumption of the impeller can be calculated based on the power number

$$P = N_p \rho N^3 d^5 \quad (4.67)$$

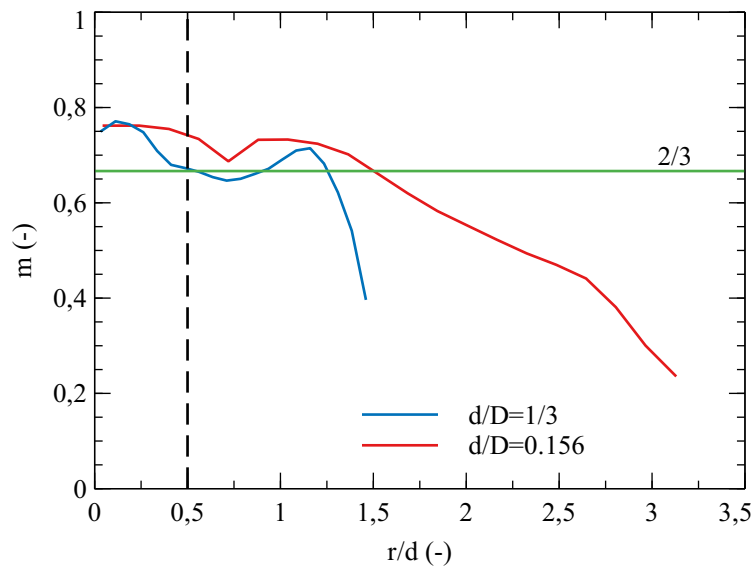
which has been experimentally measured in literature many times. Rieger et al. (2005) states that for a 6PBT45 axial impeller in a cylindrical vessel with baffles, the power number  $N_p = 1.65$  for the turbulent flow ( $Re > 2 \times 10^3$ ). On the basis of this number, which do not change for higher Reynolds numbers, it is then possible to calculate the required power input of the impeller. A comparison of two states having the same power input to the agitator is shown in Fig. 4.35.

Comparing the local values of the Nusselt number, we can see that the values are very similar when comparing states where power input  $P$  is the same. In both cases, the local maximum heat transfer intensity is just beyond the end of the impeller blades and decreases towards the impeller axis. Further from the axis, the intensity also decreases to the lowest values at the vessel wall. Just in front of the wall, we can see an increase in intensity caused by baffle effects and the whirling near the vessel wall.

The method also makes it possible to study the local values of the Reynolds number powers, which can give an indication of the flow regime that can be expected at a given location. Reynolds number powers  $m$  depending on dimensionless radial coordinate  $r/d$  for both impeller sizes can be seen in the Fig. 4.36.



■ **Figure 4.35:** Local values of Nusselt number depending on dimensionless radial coordinate  $r/d$  for the same impeller power input. Reynolds number for impeller  $d = 131$  mm is  $3.5 \times 10^4$  and for impeller  $d = 65$  mm is  $2.6 \times 10^4$ . The black dashed line represents the end of the impeller blades and the black circles indicate the same effect of increasing the heat transfer intensity around the vessel wall.

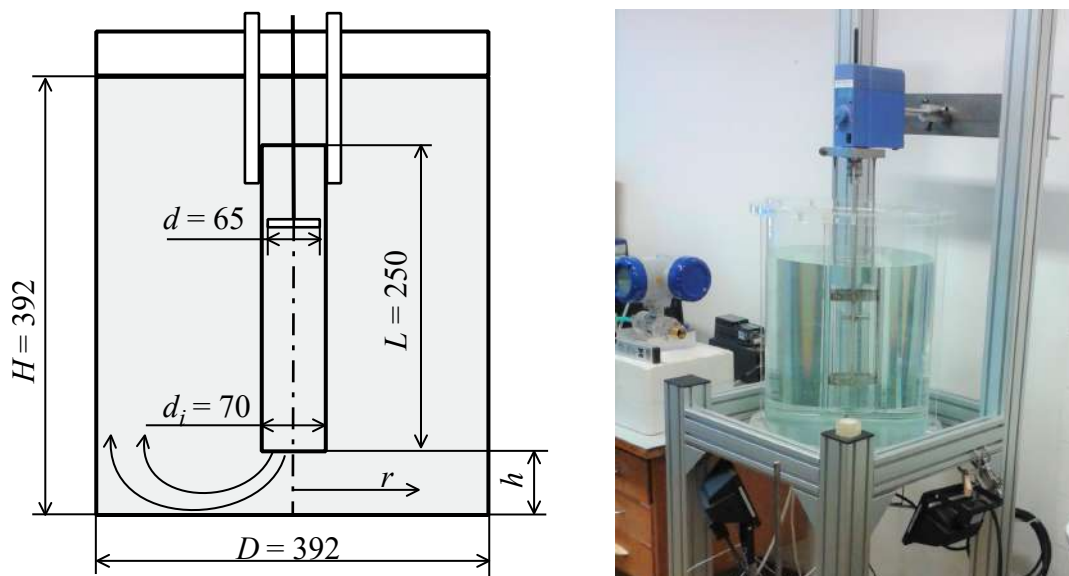


■ **Figure 4.36:** Reynolds number power in dependence on dimensionless coordinate  $r/d$  for both sizes of axial impellers. The black dashed line represents the end of the impeller blades. The green line represents a value of  $2/3$ , which is very often seen in the literature for the bottom of an agitated vessel in a turbulent mode.

The exponent values show a local maximum at the impeller axis and beyond the tip of the blades, but not very high (less visible for a smaller impeller). For the wall, however, the exponents drop very quickly to the minimum at the wall, where it is expected to slow down the flow

due to the change of direction of the flow along the vessel wall. Both dependencies for different impeller sizes are comparable.

For further experiments I also used the configuration where the axial impeller is placed in the draft tube to increase the batch circulation throughout the vessel volume. This configuration is very often seen in industry, especially when mixing suspensions or waste processing technologies. The smaller of the axial impellers ( $d = 65$  mm) was placed in axis of the draft tube with an inner diameter of  $d_i = 70$  mm and a length  $L = 250$  mm, which pumped the water downwards. Baffles were removed from the vessel. The upper inlet of the draft tube was provided with small baffles (30 mm long) to stabilize the flow and the distance of the upper edge of the impeller from the upper edge of the draft tube was 50 mm.

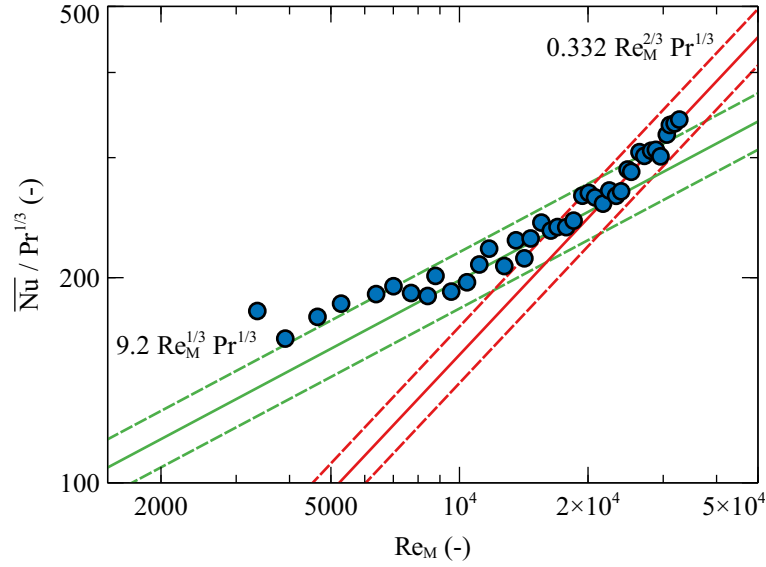


■ **Figure 4.37:** Scheme and photo of the agitator placed in the draft tube in a vessel without baffles experiment.

To calculate the Reynolds and Nusselt numbers, the characteristic dimension was changed to the inner diameter of the draft tube  $d_i = 70$  mm and the distance of the draft tube edge from the bottom  $h/d$  was also related to its inner diameter  $d_i$  of the draft tube.

For various distances of the draft tube from the bottom ( $h/d = 0.25, 0.5$  and  $1$ ) I repeated the measurements and found that the results are not as uniform as in the first case. From the measured mean values of the Nusselt number it is evident that the whole dependence cannot be interleaved by a single regression but by two (see Fig. 4.38). This regression change could represent a change in the flow mode that happens at this Reynolds number.

The measured data can be interleaved by two regressions, with the Reynolds number power  $2/3$  for higher Reynolds numbers and  $1/3$  exponent for lower values. The divide between these regressions is in the area of  $Re \approx 2 \times 10^4$ . This regression transition is also visible in other geometries, for geometry  $h/d = 0.5$ , this transition at  $Re \approx 1.5 \times 10^4$  and for geometry  $h/d = 0.25$  is transition at  $Re \approx 1 \times 10^4$ . Reducing the distance from the draft tube to the vessel bottom



■ **Figure 4.38:** Mean values of Nusselt number in dependence on Reynolds number. Axial impeller  $d = 65$  mm placed in draft tube  $d_i = 70$  mm at bottom distance  $h/d = 1$ . Solid lines represent individual regression and dashed lines represent  $\pm 10\%$  deviation from regression.

results in a reduction in the Reynolds number at which the regression changes. This is probably related to the flow area, which decreases as the distance  $h/d$  decreases, and hence the local velocity at this point increases.

The very low value of the Reynolds number power usually indicates the area of laminar flow. Freund (2008) says that it is not possible to measure the heat transfer coefficients in the laminar region by the TOIRT method, because it does not meet any of the boundary conditions  $T = \text{const.}$  or  $q = \text{const.}$  Another problem may be the disruption of the temperature and velocity profile due to heating. Due to these circumstances, I decided to omit these experiments from the overall regression for further data processing, so only Nusselt numbers for  $\text{Re} > 2 \times 10^4$ ,  $1.5 \times 10^4$ ,  $1 \times 10^4$  respectively will be evaluated.

I have correlated chosen experimental data with correlations

$$\overline{\text{Nu}} = 0.332 \text{Re}_M^{2/3} \text{Pr}^{1/3} \quad (4.68)$$

for  $h/d = 1$ ,

$$\overline{\text{Nu}} = 0.352 \text{Re}_M^{2/3} \text{Pr}^{1/3} \quad (4.69)$$

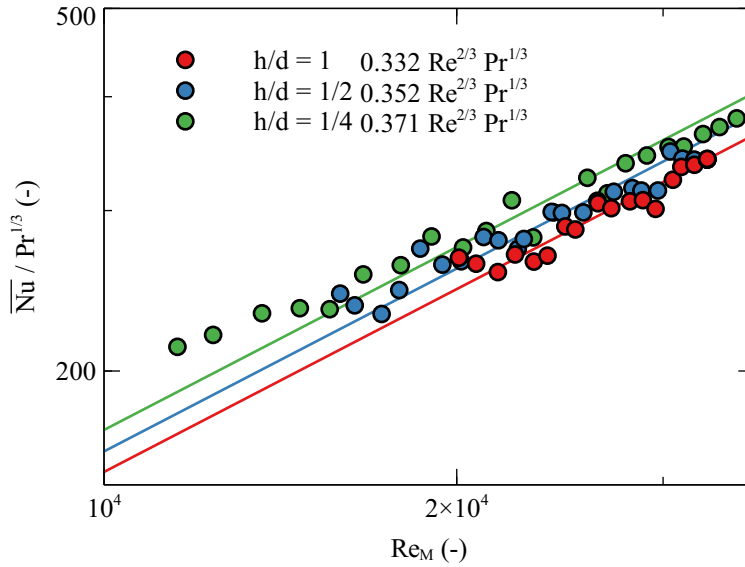
for  $h/d = 1/2$  and

$$\overline{\text{Nu}} = 0.371 \text{Re}_M^{2/3} \text{Pr}^{1/3} \quad (4.70)$$

for  $h/d = 1/4$ .

In the Fig. 4.39 we can see the measured Nusselt numbers for individual geometries  $h/d$ . All data show a very similar tendency on Reynolds number, but the smaller the distance  $h/d$ , the larger the geometric constant  $C$ .

When comparing the regression for the axial impeller with  $d = 65$  mm in the baffled vessel and the same axial impeller placed in the draft tube, we see that they are very similar, but



■ **Figure 4.39:** Measured Nusselt numbers in dependence on Reynolds number for different distances from the bottom  $h/d$ . Matching color solid lines represent individual regressions.

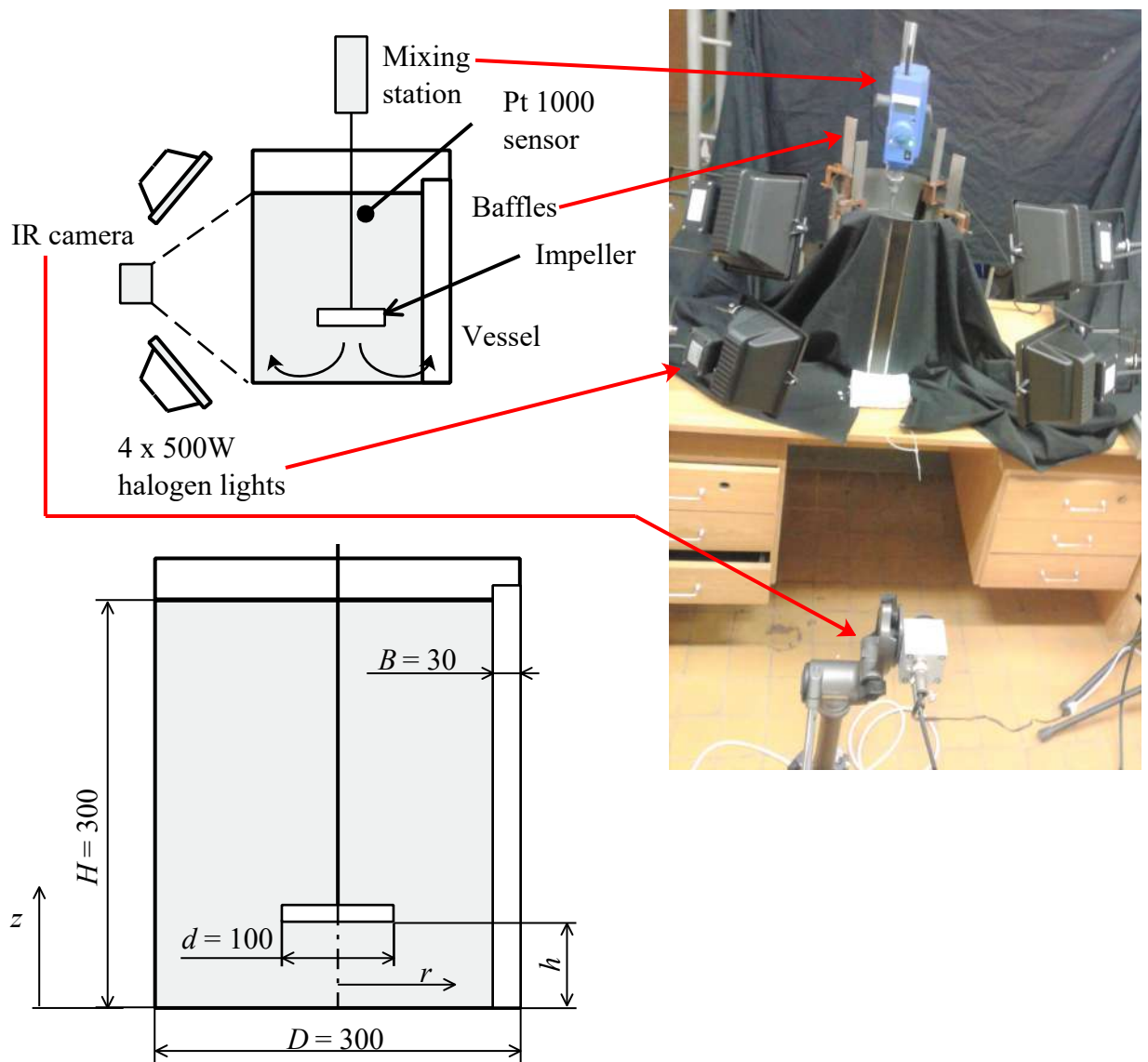
for the impeller placed in the draft tube we get slightly higher geometric constant values  $C$ . Furthermore, it can be assumed that the distance of the draft tube edge from the bottom of the vessel has a visible effect on the heat transfer intensity. The results of this measurement are also in Solnař et al. (2016).

#### 4.8.2 Wall of vessels with agitators

Experiments were performed in a flat bottom stainless steel vessel having a diameter  $D = 300$  mm. The entire vessel was made of mat. EN 1.4301 ( $\rho = 7800 \text{ kg/m}^3$ ,  $c_p = 501 \text{ J/(kg K)}$  and  $k = 14.6 \text{ W/(m K)}$ ) with a wall thickness  $\delta = 1.03$  mm. The outer side was provided with a thin black matt spray in a strip 30 mm wide over the entire height of the vessel with an emissivity  $\varepsilon = 0.96$ . Other parts of the vessel were covered with black cloth to minimize glare effects. The vessel was filled with water to a height  $H = D = 300$  mm. Agitators (axial 6PBT45 and radial Rushton turbine, RT) with a diameter  $d = 100$  mm were set to a height  $h/d = 1$  into the vessel. Four baffles of width  $B = 0.1D$  were used in the vessel in the case of a 6PBT45 impeller, in the case of a RT impeller no baffles were used. A Pt1000 sensor was placed in the vessel to measure the temperature of the batch, and the thermophysical properties of the water were then determined.

Four 500 W halogen floodlights were used for the experiments, which were installed at a distance of about 300 mm from the outer wall of the vessel at an angle of 60 degrees (two along left hand side and two along the right hand side). The IR camera pointed perpendicular to the middle of the water level, i.e.  $H/D = 0.5$  from a distance of about 500 mm. Further details of the experiment are shown in Fig. 4.40. Various period and number of heat waves were chosen according to geometry. The calculation of Reynolds, Nusselt, and Prandtl numbers remains the same as in the case of the bottom of the agitated vessel. The impeller diameter was chosen as a

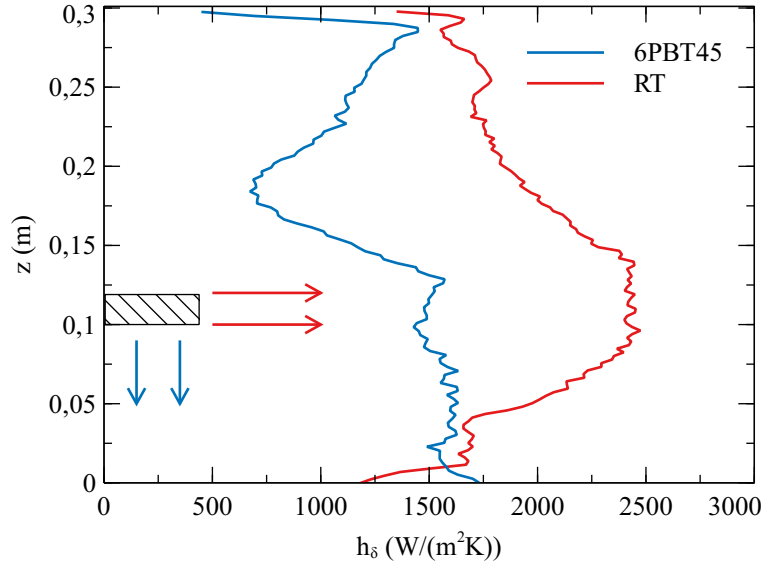
characteristic dimension. Further details can also be found in Solnař et al. (2018b).



■ **Figure 4.40:** Scheme and photo of an experiment measuring the heat transfer coefficient on the wall of an agitated vessel.

First, I compared the local values of the heat transfer coefficient as a function of the horizontal coordinate  $z$ . The heat transfer intensity shows the differences between the axial 6PBT45 impeller in the baffled vessel and the radial Rushton turbine in the same baffled vessel (see Fig. 4.41).

It is clear from the comparison that the differences between agitators used are great. The 6PBT45 axial impeller has the highest heat transfer intensity in and below the impeller region. Above the impeller, the intensity decreases very quickly and increases again at the water level



■ **Figure 4.41:** Local values of heat transfer coefficient in dependence on  $z$  coordinate for radial and axial impeller,  $Re_M = 4 \times 10^4$ . The filled rectangle represents the position of the impellers. The arrows with the corresponding color represent the basic flow pattern.

region in the vessel. The radial impeller shows the highest intensity in the impeller region and the values decrease to both sides of the agitator. Generally, Rushton turbine generates about twice the heat transfer coefficient values on the wall than 6PBT45 impeller.

The average values of the Nusselt number  $\overline{Nu}$ , which we calculated according to Eq. (1.12), were interleaved with the correlation according to Eq. (1.11) with a fixed Prandtl number power equal to  $1/3$ . The average Nusselt numbers  $\overline{Nu}$  with corresponding correlations are shown in Fig. 4.42. The correlation is not entirely consistent with the literature when the Reynolds number power was expected to be similar to the turbulent regime at the bottom, i.e. approximately  $2/3$ . My experimental data are interleaved by correlation

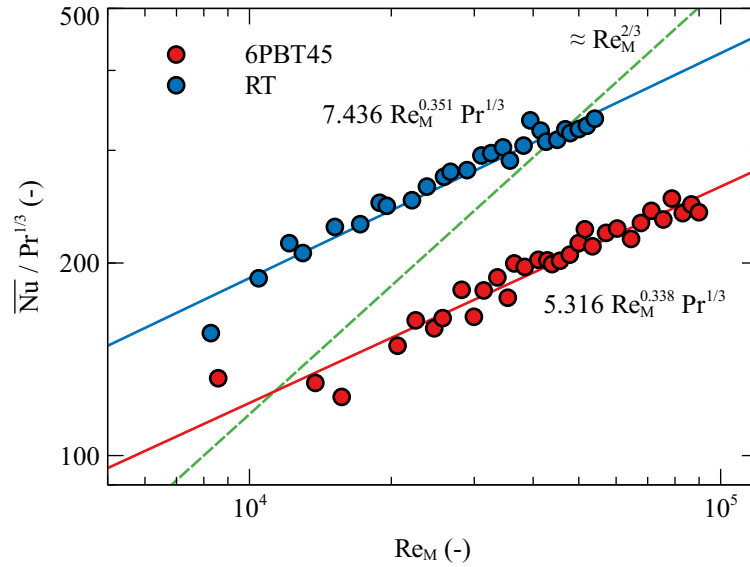
$$\overline{Nu} = 7.436 Re_M^{0.351} Pr^{1/3} \quad (4.71)$$

for 6PBT45 axial agitator and

$$\overline{Nu} = 5.316 Re_M^{0.338} Pr^{1/3} \quad (4.72)$$

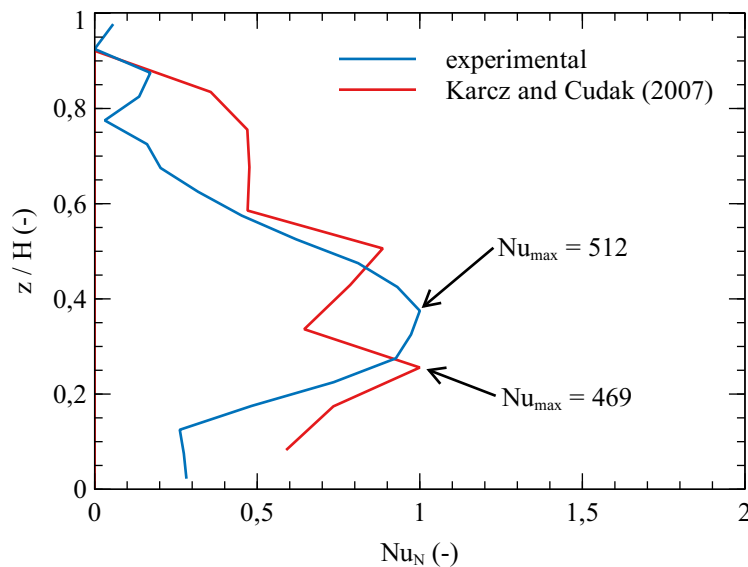
for Rushton turbine. Reynolds number power is approximately  $1/3$  or  $0.4$  in both cases, which should indicate rather the area of laminar flow.

From the comparison with  $Re_M^{2/3}$ , we can see that exponent  $2/3$  is absolutely out of range for our data and cannot be interleaved for a given correlation. Karcz and Cudak (2007) also presented local values of Nusselt number as a dependence of dimensionless coordinate  $z/H$  in their paper on the application of EDD method for measuring heat transfer on the wall of an agitated vessel. They used a hydrodynamically optimized A315 impeller as an axial impeller, but also used a Rushton turbine for radial experiments. In addition to the basic geometry in which the impeller is in axis with the vessel, they also examined the effect of eccentricity on the heat transfer intensity.



■ **Figure 4.42:** Average Nusselt numbers with corresponding correlations (matching colors) depending on mixing Reynolds number. The green dashed line represents approximately Reynolds number power equal to  $2/3$ .

For the Rushton turbine located in the vessel axis, they presented several dependencies of the local Nusselt number depending on the dimensionless height  $z/H$ . Since our Reynolds numbers are not exactly the same, we decided to compare the normalized Nusselt numbers again (see Fig. 4.43).



■ **Figure 4.43:** Comparison of normalized Nusselt numbers  $Nu_N$  for the Rushton turbine located in the vessel axis. Karcz and Cudak (2007) is for  $Re_M = 2.3 \times 10^4$  with  $Nu_{max} = 469$  and our data is for  $Re_M = 2.5 \times 10^4$  with  $Nu_{max} = 512$ .

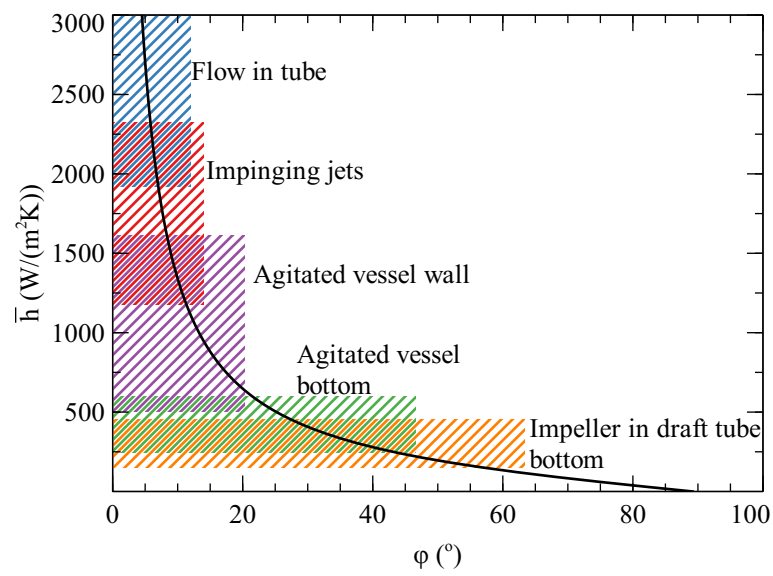
From the comparison with Karcz and Cudak (2007) we can see that my data shows consi-

derable differences, especially in the peripheral areas of measurement, although our data seems to be smoother. Overall, my Nusselt numbers are lower. The local maximum of the Nusselt number is at the same height, approximately in the area of the impeller. In the case of Karcz and Cudak (2007), the maximum is divided into two from which further down from the impeller the Nusselt numbers decrease. For the axial mixer experiments we cannot make the same comparison because we did not use the same mixer (6PBT45 vs A315).

Experimental results show a mismatch with the literature, especially in the exponent of the Reynolds number. Although the absolute values of the Nusselt number are in the same region and the shapes of the local values are very similar, I was not able to fit the data with a similar correlation as in the literature. These discrepancies are likely to be associated with a very complex flow in the vessel wall area, the emergence of macro vortices, and the fact that both axial and radial agitators create minor by-flows. All these issues can lead to incorrect results.

Overall, the TOIRT method is very suitable for measuring local values of the heat transfer coefficient at the bottom of the agitated vessel. When measuring the heat transfer on the wall of the vessel, the method certainly shows inconsistencies and imperfections. This is primarily a very low and suspicious Reynolds number power (about  $1/3$ ) for both the axial and radial agitator correlations. When comparing local values, the basic shape of Nusselt numbers is similar to Karcz and Cudak (2007), but there are also differences.

I have also prepared a plot with the range of measured average values of heat transfer coefficient for individual experiments in comparison with analytical solutions (Eq. (4.43)), see Fig. 4.44. For experiments with a large coefficient of heat transfer (pipe flow, impinging water jet) we can assume that we have a relatively narrow range of measurable phase delays  $\varphi$ . Conversely, for process apparatuses where the heat transfer coefficient is expected to be lower (agitated vessel bottom and wall), the range of measurable phase delays is relatively large, and thus a lower measurement error in this area can be expected.



■ **Figure 4.44:** Analytical solution according to Eq. (4.43) and ranges of mean values of heat transfer coefficient for various experiments. Experiments are not presented for the same value of Reynolds numbers.

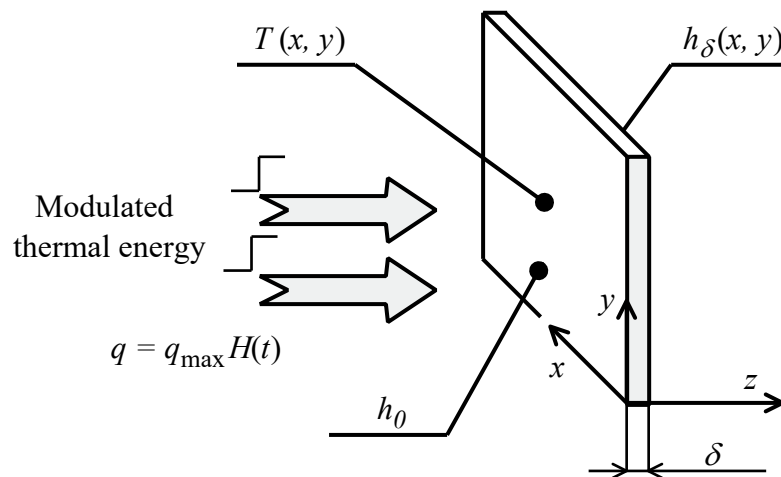


# Chapter 5

## Heat flux jump method

My idea of a new method and the derivation of gradual heating of the measured wall is shown in the Fig. 5.1. The radiative heat flux is modulated by the Heaviside function and is delivered evenly to the measured wall by halogen flood lights where a temperature profile is created by changing the heat flux. The thermophysical properties as well as the heat transfer coefficient  $h_0$  are known (or calculateable) and I assume that the change in wall temperature will not be so great as to fundamentally alter the thermophysical properties.

By the analytical solution of the development of the temperature profile of the surface temperature of the measured wall and its comparison with the experimentally measured surface temperatures (IR camera, TLC color layer ...) it is possible to determine the heat transfer coefficient  $h_\delta$  on the other side of the wall. In the latter case, the modulated sinusoidal heat flux is replaced by a constant heat flux, and for the known heat transfer coefficient  $h_\delta$ , the heat flux that best matches the measured experimental data is found.



■ **Figure 5.1:** The idea of heat flux jump method.

The method expects the thickness of the measured wall to be in the order of units or tenths

of a millimeter and of a relatively well thermally conductive material (stainless steel, aluminum, copper ...). The temperature will be measured by a contactless IR camera, thanks to which we will obtain a large amount of data depending on the camera resolution.

To solve this problem, I have introduced several simplification and assumptions:

- Wall is homogeneous
- Incident heat flux is delivered evenly
- No lateral conduction in the wall
- Thermophysical properties of the wall are constant
- Heat transfer coefficient on the left-hand side  $h_0$  is constant
- No heat losses to the environment
- Infinitely rapid propagation of heat wave in the wall

which lead to simplification of the task and its ability to analytically solve it.

Since the Heaviside and Dirac delta functions are interconnected by their own derivative, this derivation (with minimal modifications) can also be used for the impulse function. However, from an experimental point of view, such a solution is unsuitable because, due to the thermal capacities of the system, it would be necessary to use very strong heat flux sources in order to have a measurable change in the surface temperature.

## 5.1 Theoretical background

Heat conduction in a homogeneous wall with infinitely rapid heat wave propagation in a material is described by the Fourier equation. For my problem, it seems appropriate to use a Cartesian coordinate system, so the Fourier equation becomes

$$\frac{\partial T}{\partial t} = a \left( \frac{\partial^2 T}{\partial x^2} + \frac{\partial^2 T}{\partial y^2} + \frac{\partial^2 T}{\partial z^2} \right) \quad (5.1)$$

where  $a$  represents a temperature diffusivity. Assuming that the incident heat flux to the wall is uniform and there is no lateral conduction in the wall, this equation can be simplified to a 1D problem (in the  $x$  and  $y$  directions the heat fluxes will be equal to zero). This simplification makes it possible to delete the first two partial derivatives on the right hand side of the equation. If it is not in the interest of calculating the absolute value of temperature, but only its change from the initial value  $T_0$ , it is now possible to formulate the problem as

$$\frac{\partial(T - T_0)}{\partial t} = a \frac{\partial^2(T - T_0)}{\partial z^2}. \quad (5.2)$$

The boundary condition on the right hand side of the task is given only by the convective heat flux, which is characterized by the value of the heat transfer coefficient  $h_\delta$  and the temperature difference. This boundary condition can be formulated as

$$-k \frac{\partial(T - T_0)}{\partial z} \Big|_{z=\delta} = h_\delta (T - T_f) \Big|_{z=\delta}, \quad (5.3)$$

where the temperature  $T_f$  is the ambient temperature. The boundary condition on the left hand side of the task is given by the uniform incident heat flux that heats the measured wall. The wall heating causes the flow around the wall and so the boundary condition is supplemented by the convective heat flow due to natural convection, which is characterized by the value of the heat transfer coefficient  $h_0$

$$-k \frac{\partial(T - T_0)}{\partial z} \Big|_{z=0} = qH(t) - h_0 (T - T_f) \Big|_{z=0}. \quad (5.4)$$

Since this is a non-stationary problem, it is necessary to add an initial condition to these equations. I assume that at the beginning the initial temperature  $T_0$  is the same as the ambient temperature  $T_f$  i.e. the system is initially in a state of thermodynamic equilibrium. We can see from equations (5.2 – 5.5) that  $T_0$  (or  $T_f$ ) is only the additive constant and equations (5.2 – 5.5) can be formulated for

$$T_0 = T_f = 0 \quad (5.5)$$

regardless of generality of the problem. This initial condition will simplify the equations as well as the whole solution.

### ■ General solution

To simplify the solution of this system of partial differential equation (5.2), two boundary conditions (5.3) and (5.4) and initial condition (5.5), I introduced some dimensionless variables that simplify the problem. Firstly I introduced a dimensionless  $z^*$  coordinate as follows

$$z^* = \frac{z}{\delta}, \quad (5.6)$$

which is very often seen in the literature. Dimensionless time is usually defined as

$$t^* = \frac{at}{\delta^2} \quad (5.7)$$

also known as the Fourier number. By replacing dimensional variables with those dimensionless, it simplifies the Fourier equation to

$$\frac{\partial T}{\partial t^*} = \frac{\partial^2 T}{\partial z^{*2}}, \quad (5.8)$$

where I also applied the condition  $T_0 = 0$ . Since this system of equations would be very complex to solve, I decided to solve this task with the help of Laplace transformation. The partial differential equation transformed by the Laplace transform to its image is an ordinary differential equation in Laplace space

$$\mathcal{L} \left( \frac{\partial T}{\partial t^*} \right) = \mathcal{L} \left( \frac{\partial^2 T}{\partial z^{*2}} \right) \rightarrow s\bar{T}(z^*, s) - T(z^*, 0) = \frac{d^2 \bar{T}}{dz^{*2}}. \quad (5.9)$$

By this operation I get the image of the Fourier equation with variables dimensionless wall thickness  $z^*$  and complex variable  $s$ . Most often the images are obtained by the translation from the "dictionaries" of the Laplace transformation. The second expression on the left hand side of this equation represents the temperature  $T$  at  $z^*$  and at dimensionless time 0. This temperature is already defined by the initial condition  $T_0 = 0$  and so the equation will simplify to

$$\frac{d^2 \bar{T}}{dz^{*2}} - s \bar{T}(z^*, s) = 0. \quad (5.10)$$

This equation is a homogeneous second order differential equation with constant coefficients that can be solved using the characteristics. The characteristic equation is in this case

$$\lambda_c^2 - s = 0, \quad (5.11)$$

and the roots of equation  $\lambda_c$  are then equal to

$$\lambda_c = \pm \sqrt{s} \quad (5.12)$$

and the general solution of this equation can therefore be found in the form of a sum of hyperbolic functions

$$\bar{T}(z^*, s) = C_1 \sinh(\sqrt{s} z^*) + C_2 \cosh(\sqrt{s} z^*), \quad (5.13)$$

where  $C_1$  and  $C_2$  are constants that has to be solved by boundary conditions.

### ■ Transformation and application of boundary conditions

The boundary conditions from the left and right hand sides of the task can be overwritten with the same dimensionless variables  $z^*$  and  $t^*$ . In addition, we can add an initial condition  $T_0 = T_f = 0$ , which partially simplifies expressions. For the boundary condition on the right hand side we get

$$z^* = 1 \rightarrow -k \left. \frac{\partial T}{\partial z^*} \right|_{z^*=1} = h_\delta \delta T|_{z^*=1} \quad (5.14)$$

and for the left hand side boundary condition

$$z^* = 0 \rightarrow -k \left. \frac{\partial T}{\partial z^*} \right|_{z^*=0} = qH(t) - h_0 \delta T|_{z^*=0}. \quad (5.15)$$

Images of boundary conditions in Laplace space are obtained by forward transformation again according to the "dictionary" of Laplace transformation

$$z^* = 1 \rightarrow -\frac{d\bar{T}(1, s)}{dz^*} = \frac{h_\delta \delta}{k} \bar{T}(1, s) \quad (5.16)$$

and

$$z^* = 0 \rightarrow -\frac{d\bar{T}(0, s)}{dz^*} = \frac{1}{s} q \frac{\delta}{k} - \frac{h_0 \delta}{k} \bar{T}(0, s). \quad (5.17)$$

Since both boundary conditions are of the third kind and are expressed by the derivative of the temperature image, it is necessary to find the derivative of the general solution for the further procedure

$$\frac{d\bar{T}(z^*, s)}{dz^*} = C_1 \sqrt{s} \cosh(\sqrt{s} z^*) + C_2 \sqrt{s} \sinh(\sqrt{s} z^*). \quad (5.18)$$

#### ■ Left hand side

If I substitute for the dimensionless wall thickness  $z^* = 0$  (left hand side of the task) in the general solution, I obtain

$$\bar{T}(0, s) = \underbrace{C_1 \sinh(0)}_{=0} + C_2 \underbrace{\cosh(0)}_{=1} \quad (5.19)$$

where the individual hyperbolic functions are already expressed by their values. Applying this coordinate to the derivative of the general solution we obtain

$$\frac{d\bar{T}(0, s)}{dz^*} = C_1 \sqrt{s} \underbrace{\cosh(0)}_{=1} + \underbrace{C_2 \sqrt{s} \sinh(0)}_{=0} \quad (5.20)$$

where the values of hyperbolic functions are again expressed. Applying the boundary condition we get

$$\frac{\delta q}{ks} + \text{Bi}_0 \bar{T}(0, s) = C_1 \sqrt{s}. \quad (5.21)$$

For expression  $\bar{T}(0, s)$  I can add the solution (5.19) from the general equation. By assigning the  $\bar{T}(0, s)$ , I obtain the first equation for solving integration constants.

$$-\frac{\delta q}{ks} + \text{Bi}_0 C_2 = C_1 \sqrt{s} \quad (5.22)$$

#### ■ Right hand side

If I substitute for the dimensionless wall thickness  $z^* = 1$  in the general solution, I obtain

$$\bar{T}(1, s) = C_1 \sinh(\sqrt{s}) + C_2 \cosh(\sqrt{s}). \quad (5.23)$$

Applying this coordinate to the derivative of the general solution I obtain

$$\frac{d\bar{T}(1, s)}{dz^*} = C_1 \sqrt{s} \cosh(\sqrt{s}) + C_2 \sqrt{s} \sinh(\sqrt{s}) \quad (5.24)$$

and applying the right hand side boundary condition

$$-\text{Bi}_\delta \bar{T}(1, s) = C_1 \sqrt{s} \cosh(\sqrt{s}) + C_2 \sqrt{s} \sinh(\sqrt{s}) \quad (5.25)$$

The expression  $\bar{T}(1, s)$  can be again assigned from (5.23) and I get the second equation

$$-\text{Bi}_\delta [C_1 \sinh(\sqrt{s}) + C_2 \cosh(\sqrt{s})] = C_1 \sqrt{s} \cosh(\sqrt{s}) + C_2 \sqrt{s} \sinh(\sqrt{s}) \quad (5.26)$$

### ■ Particular solution

Application of boundary conditions as well as initial conditions leads to the solution of two equations of two unknowns  $C_1$  and  $C_2$ . This system of two equations can be written into matrix

$$A = \begin{bmatrix} \sqrt{s} & \text{Bi}_0 \\ \sqrt{s} \cosh(\sqrt{s}) + \text{Bi}_\delta \sinh(\sqrt{s}) & \sqrt{s} \sinh(\sqrt{s}) + \text{Bi}_\delta \cosh(\sqrt{s}) \end{bmatrix} \begin{bmatrix} C_1 \\ C_2 \end{bmatrix} = \begin{bmatrix} -\frac{1}{s} \frac{\hat{q}\delta}{k} \\ 0 \end{bmatrix} \quad (5.27)$$

and solved, for example, with Cramer's rule for solving the system of equations. Determinant of the matrix  $A$  is

$$\det A = \sqrt{s} [\sqrt{s} \sinh(\sqrt{s}) + \text{Bi}_\delta \cosh(\sqrt{s})] - \text{Bi}_0 [\sqrt{s} \cosh(\sqrt{s}) + \text{Bi}_\delta \sinh(\sqrt{s})] \quad (5.28)$$

and the constants  $C_1$  and  $C_2$  can be calculated from the subdeterminants (using the Cramer's rule)

$$C_1 \det A = -\frac{1}{s} \frac{\hat{q}\delta}{k} [\sqrt{s} \sinh(\sqrt{s}) + \text{Bi}_\delta \cosh(\sqrt{s})] \quad (5.29)$$

and

$$C_2 \det A = \frac{1}{s} \frac{\hat{q}\delta}{k} [\sqrt{s} \cosh(\sqrt{s}) + \text{Bi}_\delta \sinh(\sqrt{s})]. \quad (5.30)$$

Therefore, finding a non-stationary temperature profile in the wall, as a particular solution to equations (5.2 – 5.5), can be expressed in Laplace's space as

$$\bar{T}(z^*, s) = \frac{C_1 \det A}{\det A} \sinh(\sqrt{s} z^*) + \frac{C_2 \det A}{\det A} \cosh(\sqrt{s} z^*) \quad (5.31)$$

This derivation and application is in the article Solnař and Dostál (2019).

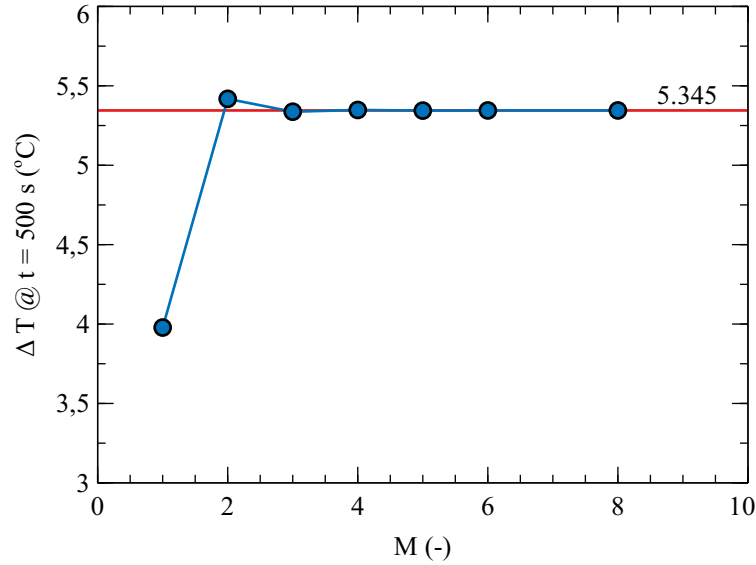
### ■ Inverse Laplace transformation

The inverse Laplace transformation of such a complex image of function  $\bar{T}(z^*, s)$  by direct translation or decomposition into partial fractions is too complicated, so I decided to perform the inverse transformation numerically. Abate and Whitt (2006) introduced a numerical solver for inverse Laplace transformation for MATLAB software which is free to download.

The MATLAB `talbot_inversion(f_s, t, M)` function returns for a given function in Laplace space  $f_s$ , for a vector of computational times  $t$  (in our case the dimensionless values of time  $t^*$ ), and for the number of iterations  $M$  the real value of a function  $f(t)$  in time. In our case, the function  $f(t)$  is the real value of the temperature change  $\Delta T$  from the initial value  $T_0$ . From a mathematical point of view,  $T_0$  is only an additive constant. All results are calculated for thermophysical properties of common stainless steel, see Tab. 5.1.

The number of iterations of the numerical reverse transform  $M$  is dependent on the values used in the equation, but the same result has been achieved since 4 or 5 iterations. We use 64 iterations for analytical calculations.

One of the limit cases of this solution can occur if both heat transfer coefficients are zero (modeled using very low coefficients  $h_0 = h_\delta = 1 \times 10^{-16}$ ). In this case, the temperature change



■ **Figure 5.2:** Dependence of the resulting value of the temperature value at time  $t = 500$  s on the number of iterations  $M$  in the `talbot_inversion` function.

can be calculated analytically based on the calorimetric equation for the unit dimensions in the  $x$  and  $y$  directions ( $x = y = 1$  m). The equation for calculating temperature change is

$$\Delta T = \frac{qt}{\delta \rho c_p} \quad (5.32)$$

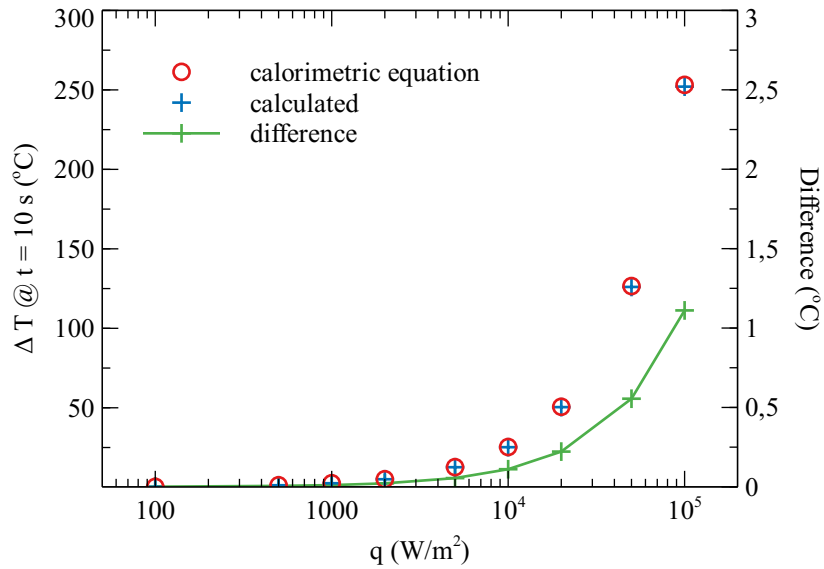
and is dependent on the thermophysical properties of the wall ( $\rho, c_p$ ) as well as on the incident heat flux  $q$  and duration time  $t$ . Comparisons of the analytically calculated temperature changes and those calculated from our derivation are shown in Fig. 5.3 for various heat flux values  $q$ .

For the second limit case, where both heat transfer coefficients are infinitely large, the wall temperature should not change in any way. This prerequisite is also met.

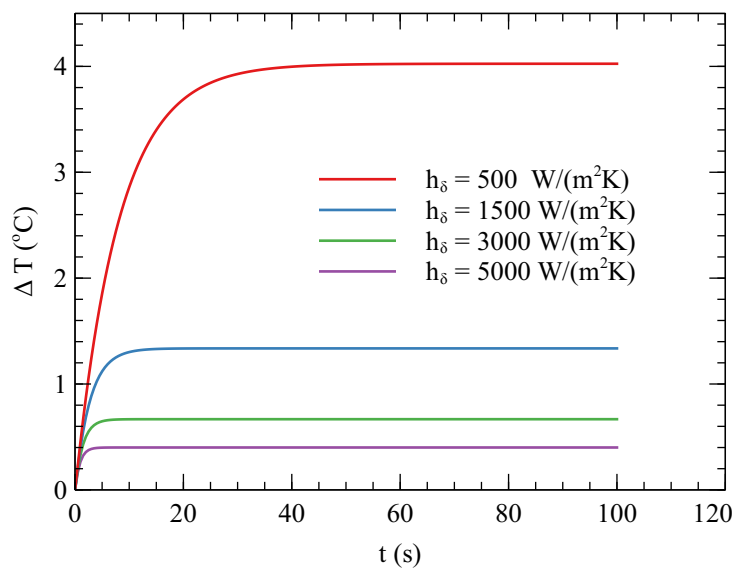
The results of the analytical solution (with numerical inverse transformation) for various values of the heat transfer coefficient  $h_\delta$  that are calculated for the thermophysical properties given in the Tab. 5.1 can be seen in the Fig 5.4.

■ **Table 5.1:** Thermophysical properties of common stainless steel (EN 1.4307) and other variables, which are considered for the calculation of analytical results.

Variable	Value	Unit
heat flux rate $q$	2 000	W/m <sup>2</sup>
heat transfer coefficient $h_0$	3	W/(m <sup>2</sup> K) (free convection)
dimensionless thickness $z^*$	0	—
wall thickness $\delta$	0.001	m
thermal conductivity $k$	15.0	W/(m K)
specific heat capacity $c_p$	500	J/(kg K)
wall density $\rho$	7 900	kg/m <sup>3</sup>



■ **Figure 5.3:** Calculated temperature difference  $\Delta T$  at time  $t = 10$  s for various values of incident heat flux  $\dot{q}$  in the limit case of zero heat transfer coefficients. The thermophysical properties of the wall are the same.



■ **Figure 5.4:** The calculated temperature changes  $\Delta T$  for the different values of the heat transfer coefficient  $h_\delta$  at the location  $z' = 0$ . The thermophysical properties of the wall are given in the Tab. 5.1.

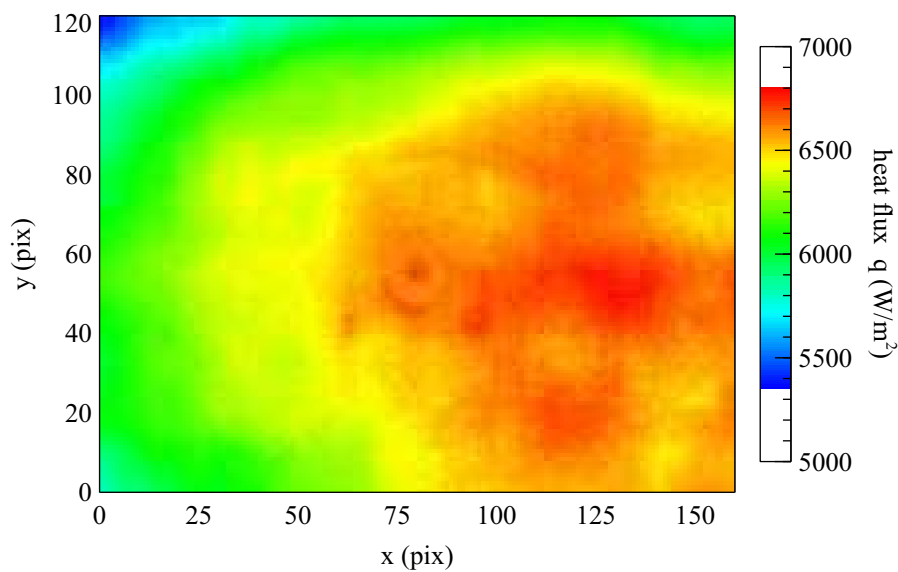
The analytically calculated values of surface temperature changes  $\Delta T$  are also influenced by the magnitude of the incident heat flux  $q$ . Changing the heat flux value results in a change in absolute temperature difference values, but does not affect the shape of the dependence. For real measurements, this means that in the experiment we do not need to know the absolute value of the incident heat flux  $q(x, y)$  if we convert the temperature record into a normalized

form according to

$$T_N = \frac{T - T_0}{\Delta T}. \quad (5.33)$$

Thereafter, any heat flux value  $q$  can be substituted and the result will not be affected.

Nevertheless, it is advisable to position the heat flux sources correctly so that the incident heat flux  $q$  is as even as possible. If I insulate the right hand side of the task (see Fig. 5.1,  $z = \delta$ ,  $z' = 1$ ), I will simulate an environment where the heat transfer coefficient  $h_\delta = 0$ . In this case, the only variable (if I calculate the value  $h_0$  based on the correlations) is the heat flux  $q$ , which becomes measurable. In addition, it is possible to determine the distribution of heat flux  $q(x, y)$  over the entire measured wall. Such a process leads to an improvement in the distribution of the incident heat flux on the wall.

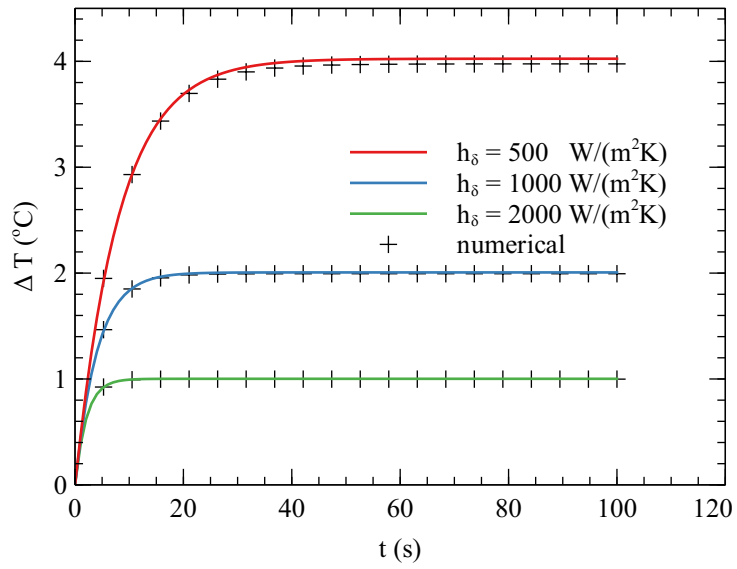


■ **Figure 5.5:** Heat flux distribution on the measured wall  $q(x, y)$ . The position of the heat flux sources has not been adjusted in any way to achieve a more even distribution.

## 5.2 Numerical confirmation

I compared analytically calculated temperature differences with numerical simulation in MATLAB to confirm the correctness of the method derivation. The numerical simulation was performed using the function `pdepe`, which is a solver of partial differential equations. Fourier equation in Cartesian coordinates was supplemented with the same boundary and initial conditions and numerically solved for 5 dimensional points (the study shows that 3 dimensional, which is minimum for calculation, points are sufficient). The analytical and numerical values are compared in the Fig. 5.6.

The comparison of the numerically and analytically calculated values shows that the temperature differences also coincide for different values of the heat transfer coefficient  $h_\delta$ . The



■ **Figure 5.6:** Comparison of analytically and numerically calculated values of temperature differences for different values of heat transfer coefficient  $h_\delta$ .

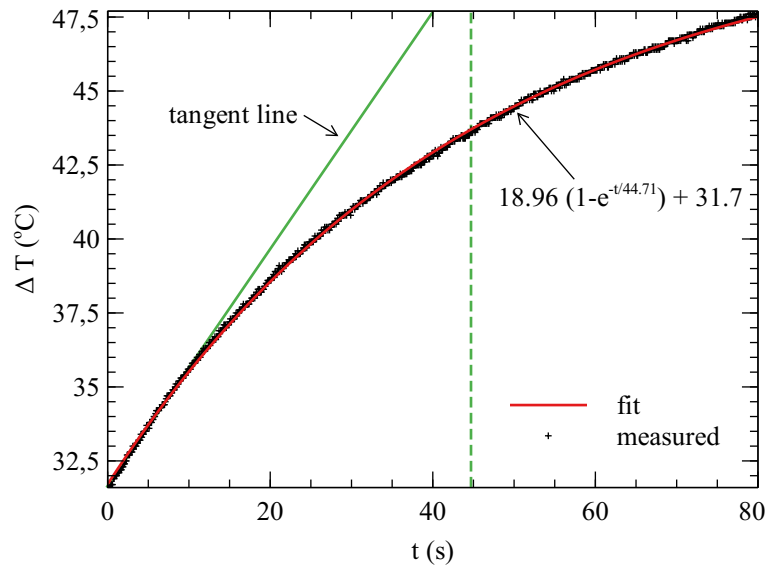
maximum difference recorded is  $0.06 \text{ }^\circ\text{C}$  ( $\approx 1.4\%$ ), which is related to the numerical calculation.

## 5.3 Data reduction

All measured temperature fields from the IR camera are converted into a 3D matrix for further processing in MATLAB. From the surface temperature record at each point (see Fig. 5.7), the value of the time constant  $\tau$  is then obtained by non-linear regression based on the model function

$$\Delta T = A(1 - e^{-t/\tau}) + B. \quad (5.34)$$

From nonlinear regression results, individual time constants  $\tau$  are then stored in the matrix  $\tau(x,y)$ .



■ **Figure 5.7:** Recording of measured surface temperatures for one measuring point with fitted model function. This point has a time constant of about 44 s, which corresponds to a heat transfer coefficient  $h_\delta$  of about  $105 \text{ W}/(\text{m}^2 \text{ K})$  for a given system.

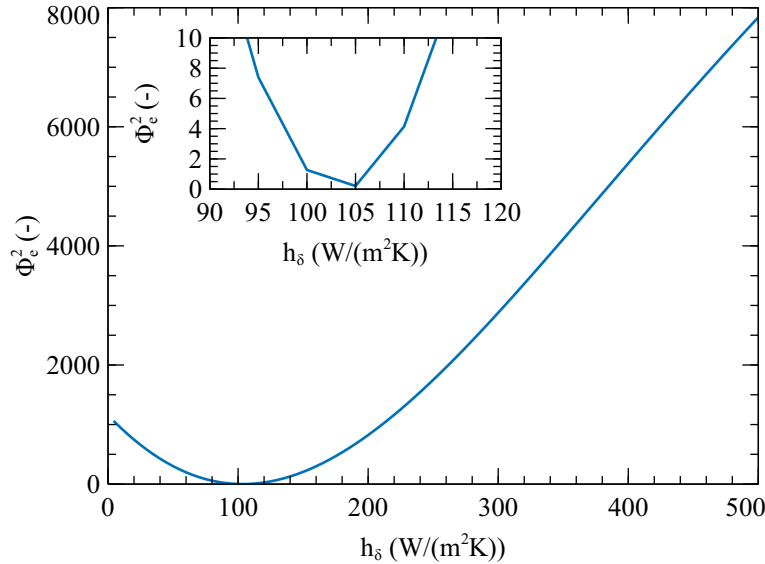
Then I use the analytical solution to calculate the temperature changes  $\Delta T$  for different values of the heat transfer coefficient  $h_\delta$ . Then I evaluate these analytical temperature records in the same way to obtain the dependence of the heat transfer coefficient on the measured time constant  $h_\delta = f(\tau)$ . From the calculated function  $h_\delta = f(\tau)$  it is then possible to determine individual heat transfer coefficients  $h_\delta$  for experimentally measured and evaluated time constants  $\tau$  based on interpolation technique.

Alternatively, it is possible to calculate the heat transfer coefficient values  $h_\delta$  by comparing analytically calculated  $T_a$  and experimentally measured temperature differences  $T_e$  and finding the minimum error  $\phi_e$  between these data. In this case, the analytically calculated values are determined from the experimentally measured values and their squared deviations are added in  $\phi_e^2$ . The smallest deviation is then selected as the correct value, to which we know the entered value of the heat transfer coefficient  $h_\delta$  and can be thus identified.

Since both temperatures  $T_a$  and  $T_e$  are also dependent on the value of heat flux  $q$ , it is necessary to normalize these values (set them between 0 and 1) according to Eq. 5.33. Normalized

temperatures are not influenced by the incident heat flux and their shapes remain the same, so it is possible to find their minimum difference from the analytically calculated values, which leads to the determination of the heat transfer coefficient.

$$\min [\phi_e^2 = \sum (T_{N,a}(h) - T_{N,e})^2] \rightarrow h(x,y). \quad (5.35)$$



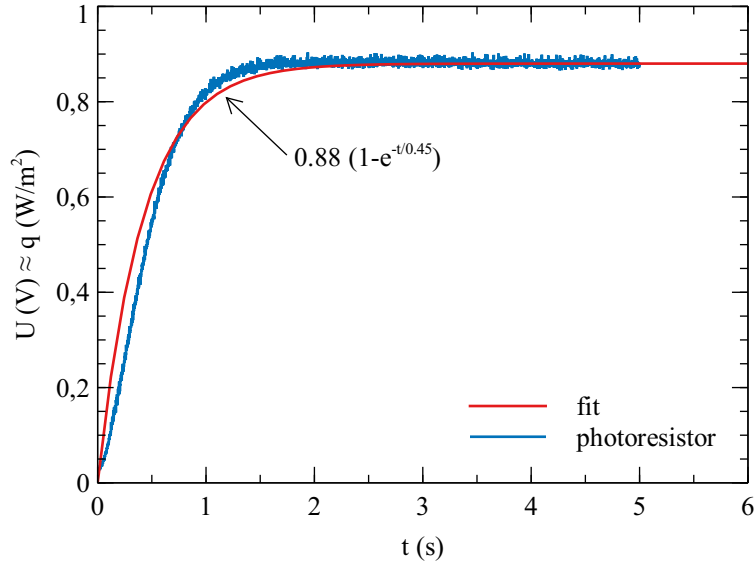
■ **Figure 5.8:** Square of error between individual analytically calculated and experimentally measured surface temperatures. This comparison would lead to an evaluation of the heat transfer coefficient  $h_\delta = 105 \text{ W}/(\text{m}^2 \text{ K})$ .

As can be seen, the two methods of determining the heat transfer coefficient  $h_\delta$ , the time constant determining method and the alternative method through finding the minimum deviation  $\phi_e$  are comparable and evaluate very similar or the same resulting heat transfer coefficients  $h_\delta$ .

For all dynamic methods the shape of the excitation function is critical, in our case it is the perfect Heaviside function. Since the halogen flood lights (used to generate radiative heat flux) have their own heat capacity, the condition of perfect Heaviside function is not met. To describe the transient characteristic and the real shape of the excitation function, I prepared a simple experiment where we installed a photoresistor in front of halogen light, which recorded the intensity of illumination. For simplicity, I assume that the heat flux intensity is proportional to the light intensity.

From the recording of the measured electrical voltage (disproportionate to the electrical resistance) to a step change, I found the transition characteristic of the flood lights, see Fig. 5.9.

From the transient characteristic I can estimate that this is an exponential function. The exponential function that fits the measured data is then used in the inverse Laplace transform to replace the theoretical Heaviside function.



■ **Figure 5.9:** Transient characteristic of halogen flood lights.

## 5.4 Sensitivity analysis

I divided the sensitivity analysis of the method into parts as well as with the oscillation method. In the first part, I observed the effect of noisy, experimentally measured data on the resulting time constant  $\tau$ . In the second part I monitored the sensitivity of the calculated heat transfer coefficient  $h_\delta$  to the change in time constant  $\tau$  and in the last part I monitored the influence of individual thermophysical and other properties on the resulting heat transfer coefficient  $h_\delta$ .

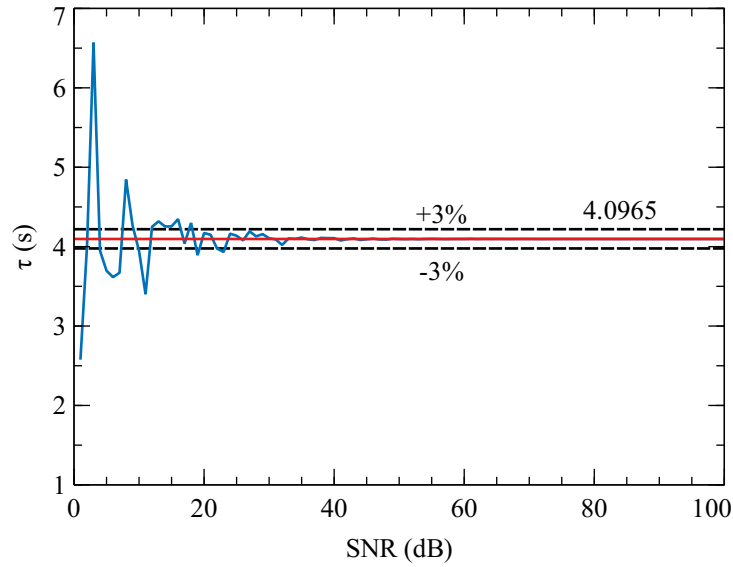
In the first part I observed the effect of data noise on the calculated time constant of temperature recording. Since SNR assumes an oscillating signal, its definition for non-oscillation signals must be changed. In this case, the signal amplitude is referred to the difference between the start and end values of the data recording

$$\text{SNR} = \frac{\Delta T}{A_{\text{noise}}}. \quad (5.36)$$

For the given value of the heat transfer coefficient  $h_\delta$  (and thus for a given time constant  $\tau$ ) I calculated the analytical response of the surface temperature, which I then influenced by a various noise level (MATLAB function `awgn`, type 'measured'). From the noisy data I recalculated the value of time constant  $\tau$ . The dependence of the calculated time constants on the SNR is shown in the Fig. 5.10.

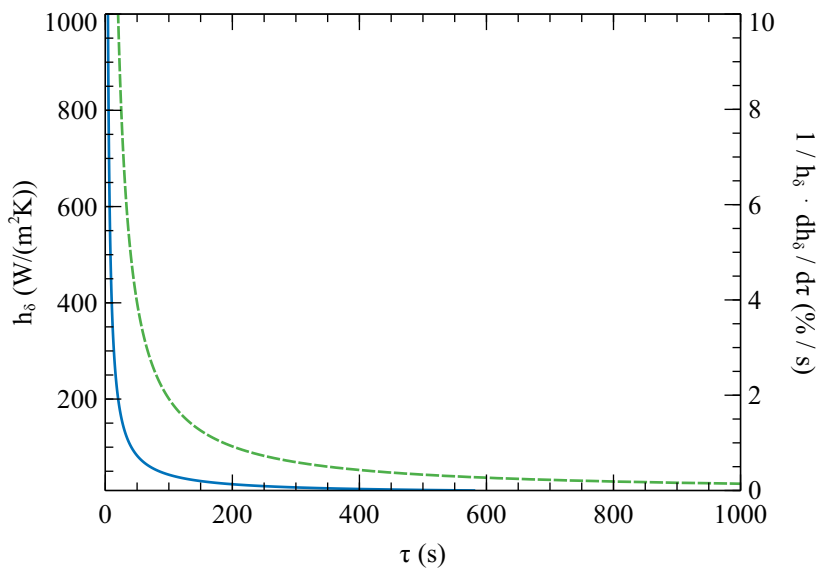
The average value of the upgraded SNR for our experimental data is 60.8 dB, so I can assume that the conversion of the measured temperatures to the time constant is not affected by noise from the data recording.

In the second part I monitored the sensitivity of the heat transfer coefficient  $h_\delta$  to the change in time constant  $\tau$  (see Fig.5.11). For very low heat transfer coefficients, the sensitivity is at a very good level, even below 1 %. However, these values are mostly associated with natural



■ **Figure 5.10:** Dependence of calculated time constants  $\tau$  from a noisy generated data record on the SNR value. The red line represents the set value of the time constant.

convection, which is not in the direct interest of this work and there will also be a risk of non-compliance with the assumptions of the method due to lateral conduction. For higher values of the heat transfer coefficient, the sensitivity increases very quickly, and for  $h_\delta$  values greater than  $1500 \text{ W}/(\text{m}^2 \text{ K})$ , the results will be affected by a larger error.



■ **Figure 5.11:** Dependence of heat transfer coefficient  $h_\delta$  on time constant  $\tau$  of measured wall temperature response. The dependence is supplemented by relative sensitivity  $1/h_\delta \cdot dh_\delta/d\tau$

In the third part I investigated the influence of thermophysical and other parameters on the resulting heat transfer coefficient  $h_\delta$ . The results of uncertainty analysis are shown in Tab 5.2.

From the results we can conclude that most parameters have a fundamental influence in the area of small values of heat transfer coefficient ( $h_\delta \approx 100 \text{ W}/(\text{m}^2 \text{ K})$ ) and for higher values ( $h_\delta > 500 \text{ W}/(\text{m}^2 \text{ K})$ ) their influence decreases. On the other hand, for higher measured values  $h_\delta$ , the sensitivity of the method to change the measured time constant  $\tau$  increases rapidly.

■ **Table 5.2:** Results of sensitivity analysis on thermophysical properties of the wall, its thickness and heat transfer coefficient  $h_0$  given as a change from resulting heat transfer coefficient  $h_{\text{set}}$ . Note:  $h_0$  ( $\text{W}/(\text{m}^2 \text{ K})$ ),  $k$  ( $\text{W}/(\text{mK})$ ),  $\rho$  ( $\text{kg}/\text{m}^3$ ),  $c_p$  ( $\text{J}/(\text{kgK})$ ),  $\delta$  ( $\text{mm}$ )

$h_{\text{set}}$ $\text{W}/(\text{m}^2 \text{ K})$	$k$ $\pm 10\%$	$\rho$ $\pm 10\%$	$c_p$ $\pm 10\%$	$\delta$ $\pm 10\%$	$h_0$ $\pm 10\%$
100	$\pm 0.1$	$\pm 4.6$	$\pm 4.5$	$\pm 4.5$	$\pm 0.2$
500	$\pm 0.4$	$\pm 0.0$	$\pm 0.0$	$\pm 0.3$	$\pm 0.0$
1 000	$\pm 0.7$	$\pm 0.0$	$\pm 0.0$	$\pm 0.7$	$\pm 0.0$

This method can also be used for a negative change in heat flux (heat flux will decrease from some value to a lower one, the measured wall will cool). From a mathematical point of view, nothing for derivation changes, only the sign of the temperature change. By arranging several such heat flux changes in one measurement, it is possible to measure the heat transfer coefficient repeatedly and thus increase the accuracy of the method. The input function would thus be a pulse of finite length (in the order of tens of seconds), which would be repeated several times.

From the experimental point of view, it is a simple modification of the measurement devices. For heat flux generators (halogen flood lights), however, it is necessary to determine their own time constant twice (for increasing heat flux and decreasing heat flux) and evaluate the measured data for individual changes separately.

## 5.5 Experimental validation

As the first validation experimental measurement, I chose probably the most well-known experiment, namely heat transfer during flow in a tube. Due to the fact that the new method is more suitable for measuring lower values of the heat transfer coefficient, I chose an air as a fluid, where I expect a lower intensity of heat transfer.

For the experiment of air flow in a tube, the Gnielinski correlation with Hausen's correction for short tubes still works (and is also most often cited), and the area of Prandtl numbers also covers Prandtl number of air (about 0.7). For this case, I will also try to compare the local values of the Nusselt number from the beginning of the measuring section, where the temperature profile begins to form. For this case, there is a Gnielinski correlation for local Nusselt number values  $\text{Nu}_x$

$$\text{Nu}_x = \frac{(f/8) \text{RePr}}{1 + 12.7 \sqrt{f/8} (\text{Pr}^{2/3} - 1)} \left[ 1 + \frac{1}{3} (d/x)^{2/3} \right], \quad (5.37)$$

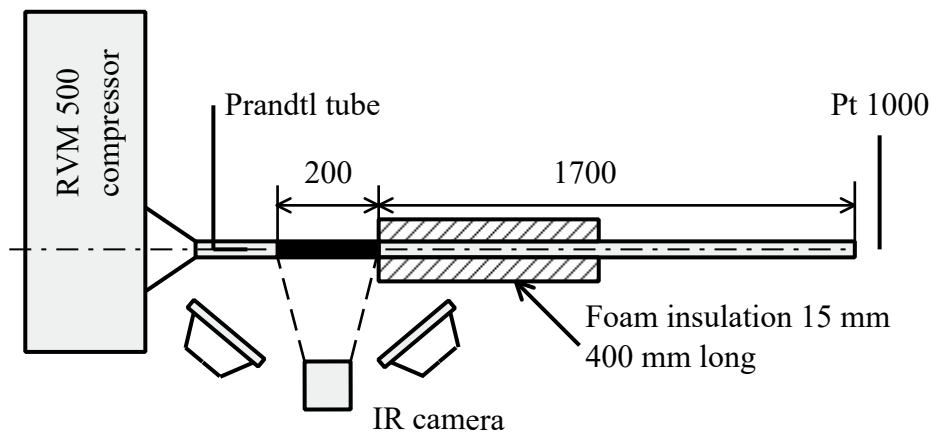
where  $f$  is the friction factor which can be expressed for smooth tubes as

$$f = (1.8 \log_{10} \text{Re} - 1.5)^{-2}. \quad (5.38)$$

The experiment was performed in a stainless steel tube ( $35 \times 1.5$ , mat. EN 1.4307,  $\rho = 7900 \text{ kg/m}^3$ ,  $c_p = 500 \text{ J/(kg K)}$  and  $k = 14.7 \text{ W/(m K)}$ ) that was 2 meters long. To create the flow, I used a radial compressor RVM 500 (max  $2.1 \text{ m}^3/\text{s}$ ) and installed the tube on the under-pressure side of the compressor, so that there is no problem with the temperature change during air compression. The 3D printed part created a transition between the stainless steel tube and the compressor and also served to place the Prandtl probe ( $2 - 90 \text{ m/s}$ ,  $\pm 1\%$ , connected to Ahlborn Almemo 2590 station) for measuring the speed of the air in the tube. Before the air inlet to the tube, I placed a Pt 1000 thermometer (Greisinger GHM 175,  $\pm 0.1^\circ \text{C}$ ) and from the temperature information I found the thermophysical properties of the air, which I used to calculate the Reynolds number (Eq. (1.7)) and Nusselt numbers (Eq. (1.5)).

At a distance of 1.7 meters, I sprayed the measuring section of the tube with a thin layer of matt black painting to increase and more constant emissivity  $\varepsilon = 0.96$ . The section before measurement area (about  $53 \times d$ ) also served to stabilize the hydrodynamic profile. The measuring section was 200 mm long and until the beginning of the measuring section the pipe was provided with thermal insulation, to ensure the development of the temperature profile right at the beginning of the measuring section.

Reynolds and Nusselt numbers are calculated the same was as in the case of TOIRT method. Further details of my measurement on the air flow in the tube are in the Fig. 5.12.



■ **Figure 5.12:** Schematic drawing of an experiment of air flow in a tube that was driven by a radial compressor.

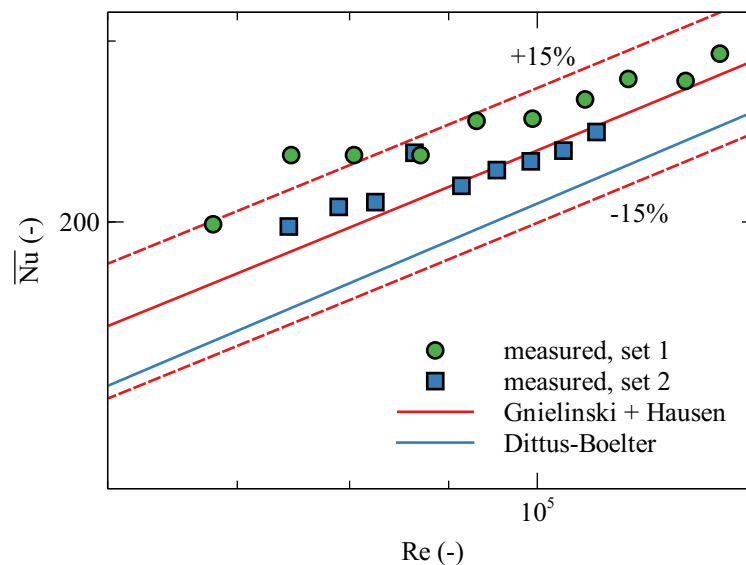
The IR camera was aimed at the flow axis and was set at a distance of about 500 mm from the tube so that it could see the entire measuring zone (200 mm). From the complete view of the IR camera, a band of about  $200 \times 10$  measurement points were selected, which corresponded to the middle of the tube in the axis of the flow. The halogen lights were also set to the flow axis,

but were adjusted to an angle so that light was not reflected from the tube into the IR camera. The angle made by the lights with the camera was about 30 degrees, the distance of the lights from the tube was about 250 mm. During the measurement, the space at the measuring section was covered with a black cloth to minimize other reflections.

Data recording was set to a time of 80 seconds and the frame rate to 10 Hz (I also used the frequencies of 20 and 50 Hz, this change had no significant effect on the measurement, so I used 10 Hz to save data space). Thus, together, each measured point was evaluated from 800 temperature records.

The maximum achievable flow velocity of air in the tube by the radial compressor is about 70 m/s ( $Re = 1.5 \times 10^5$ ), however, for repeated measurements we chose a range of velocities such as is commonly used in gas technologies, ie 30 – 50 m/s ( $7 \times 10^4 < Re < 1.1 \times 10^5$ ).

A comparison of the selection of my experimental values of the overall Nusselt number and the Gnielinski correlation with the Hausen correction for short tubes can be seen in the Fig. 5.13 as well as with the Dittus and Boelter correlation.



■ **Figure 5.13:** Comparison of a selection of experimentally measured overall Nusselt numbers (averaged over the whole measuring section) with the Gnielinski correlation with Hausen correction for short tubes and the Dittus and Boelter correlation.

From the comparison we can see that the selected data (the one with the largest deviation) can be described by Gnielinski correlation with a maximum error of 17 %, the average error is around 8 %. The tendency of the dependence of the Nusselt number on the Reynolds number is very similar to that in the literature.

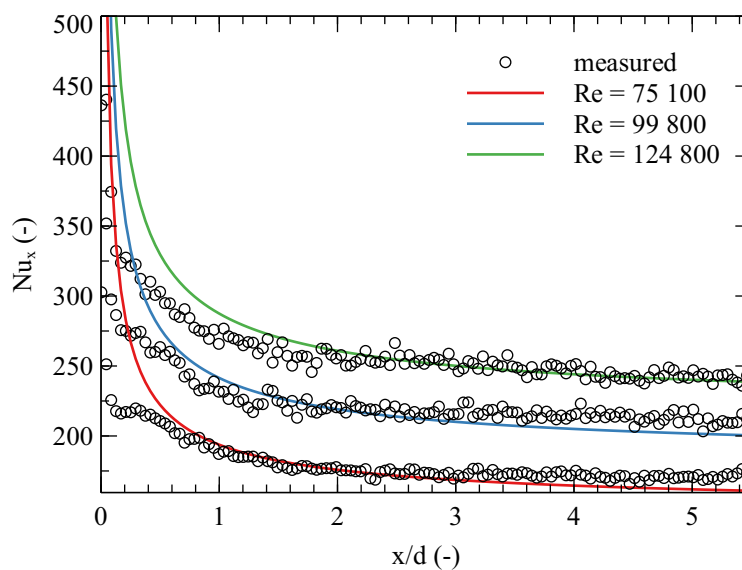
In other areas of air velocities in the tube (resp. Reynolds numbers) the tendency is very similar to the Gnielinski correlation (for  $Re > 1.2 \times 10^5$ ), only in the area of small turbulent Reynolds numbers ( $2500 < Re < 1.2 \times 10^4$ ) I recorded a deviation of tens of percent. However, the Gnielinski correlation is not valid in this area either.

In terms of the average values of the Nusselt number, the method seems to be functional, it may be more interesting to compare the local values that the method allows to measure. In this

case, the local values were averaged along only one coordinate (shorter side of the measured bar, about 10 measuring points) and compared with the Gnielinski correlation to calculate the local values of the Nusselt number  $Nu_x$ .

In the literature, it is usual to plot local values depending on the dimensionless distance from the beginning of the measuring zone, which is related to the inner diameter of the pipe  $x/d$  for various Reynolds numbers. Alternatively, the presentation of the results can be seen in the literature as the ratio of the local Nusselt number to its value in the very far region from the beginning.

A comparison of the local values of Nusselt numbers along the  $x$  coordinate from the beginning of the measuring section with the Gnielinski correlation for various Reynolds numbers can be seen in the Fig 5.14.



■ **Figure 5.14:** Comparison of experimental local values of Nusselt number with Gnielinski correlation for various values of Reynolds number.

From the comparison we can see that the values are very similar to those in the literature. A small deviation can be seen in the region of dimensionless coordinate  $x/d < 1$ , however, this is a deviation of up to 10%, which I consider to be a very good agreement. From the coordinates  $x/d > 1$ , the data are practically identical to the literature with minimal error.

The method seems to work for this experiment, mostly 1D air flow in a tube. In the area of velocities, which often occur in the flow of gases in technologies and factories, the method is in very good agreement with the literature, especially the most cited Gnielinski correlation. In the higher regions of Reynolds numbers, the trend continues and the maximum recorded data deviation is 17 %. In the area of lower Reynolds numbers, I also noticed higher deviations, in the order of tens of percent, but it was an area where there is not valid Gnielinski correlation.

In the case of comparing local values, the method again has a very good agreement with the literature, in the area  $x/d > 1$  the data are practically identical.

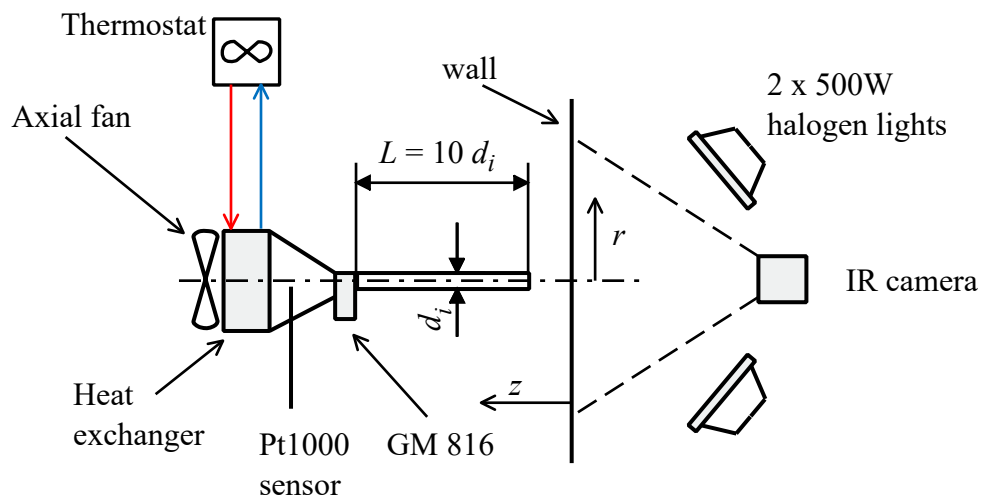
## 5.6 Impinging jets

Heat flux jump method was tested on experimental measurement of local values of heat transfer coefficient between smooth wall and an impinging air jet. For this experiment, air was selected (as opposed to TOIRT method with water) because I assume lower values of the heat transfer coefficient for which this method seems more suitable.

My experimental measurement was carried out on a rigid aluminum frame on which a  $400 \times 400$  mm stainless steel wall was fastened with screws. The wall was made of mat. EN 1.4301 with a thickness of  $\delta = 1$  mm ( $\rho = 7800$  kg/m<sup>3</sup>,  $c_p = 501$  J/(kg K) and  $k = 14.6$  W/(mK)). All other components were also attached to the frame to secure the position.

The air was compressed by an axial fan (SunOn, 12V, 1.6A) which was controlled by an adjustable DC power source to set different flow rates. Air was pushed through the fin heat exchanger ( $120 \times 120$  mm) to maintain the temperature of the flowing air. A tapered 3D printed part was installed behind the heat exchanger, which also held the propeller anemometer (Benetech GM 816, 0 – 30 m/s,  $\pm 5\%$ ) in position. An aluminum tube ( $35 \times 2$  mm,  $d_i = 31$  mm,  $L = 10d_i$ ) was installed just behind the anemometer. Distance of the tube from the wall was set to  $z/d = 1$ . The whole device was firmly mounted to the aluminum frame. Details of this experiment are shown in the Fig. 5.15.

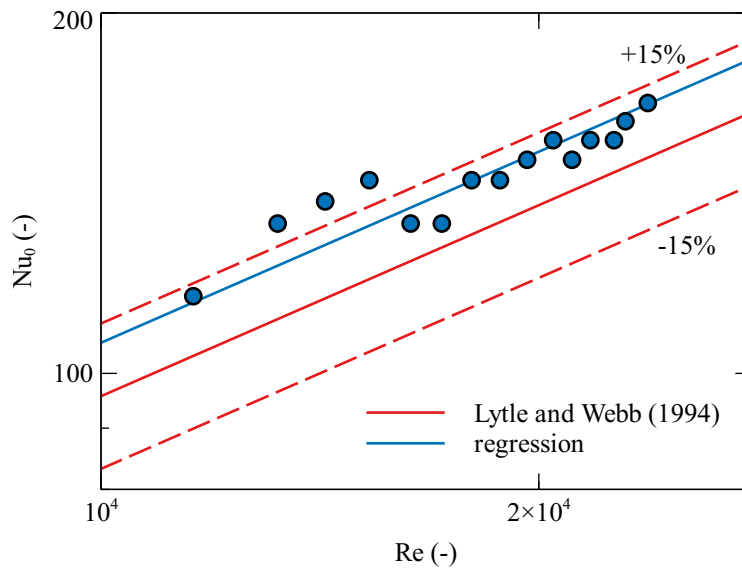
Halogen flood lights and IR camera were positioned from the other side of the experiment to scan the entire surface of the measured wall. The IR camera was about 400 mm away from the measured wall as well as halogen flood lights. The position of the halogens has been adjusted so that the incident heat flux is as even as possible. By correctly adjusting halogens, a heat flux  $q = 5685$  W  $\pm 5.5\%$  was achieved over the entire measured surface.



■ **Figure 5.15:** Schematic drawing of measurement of local values of the heat transfer coefficient between smooth wall and impinging air jet.

The Reynolds number was calculated from the measured air velocities (using a propeller anemometer) in the tube according to Eq. (1.7) and the thermophysical properties of the air were obtained depending on the measured temperature by the Pt1000 sensor. Nusselt number is calculated in the same way as in the experiment of measuring the heat transfer between an impinging water jet and a smooth wall by the TOIRT method, see Eq. (1.5).

In Fig. 5.16 we can see a comparison of our experimental data with the correlation of Lytle and Webb (1994) for Nusselt numbers at the coordinate  $r/d = 0$ , i.e. at the so-called stagnant point. From the comparison we can see that our values are relatively consistent with the literature and hold the same trend on Reynolds number. However, our values are about 10% higher than those predicted by Lytle and Webb (1994). Most of our measured data can be described by this correlation with an error of about 15% and all data with an error of less than 20% which I believe is a very good result.

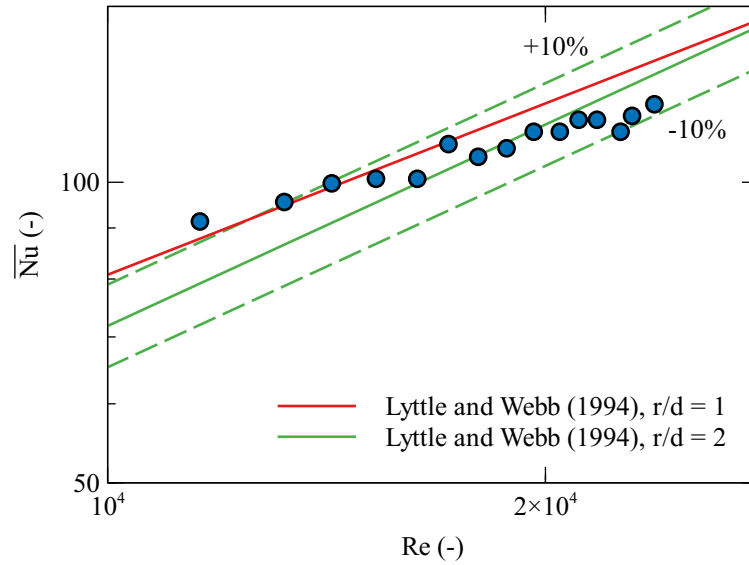


■ **Figure 5.16:** Nusselt numbers at a stagnant point depending on Reynolds number and comparison with the correlation of Lytle and Webb (1994). The red dashed lines represent a deviation of  $\pm 15\%$  from the original correlation of Lytle and Webb (1994).

As with the temperature oscillation method, I also compared the average values of the Nusselt number  $\overline{Nu}$  with the correlation of Lytle and Webb (1994), comparison can be seen in Fig. 5.17.

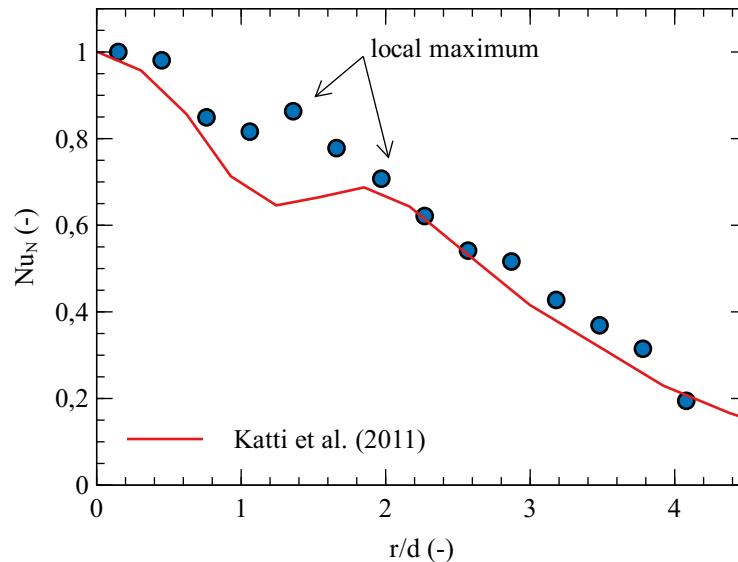
By comparing the average Nusselt numbers  $\overline{Nu}$  we can conclude that the absolute values of the Nusselt numbers agree with the literature. But my data show a slightly different tendency to depend on Reynolds number. However, my data can be described by correlation of Lytle and Webb (1994) for area  $r/d = 2$  with an error of less than 10%, so I consider the data relevant. For experimental data, the correlation for area  $r/d = 1$  is more suitable, but it is not fully correct in terms of evaluation. My averaging area is approximately  $r/d = 3$ .

In the same way, I compared the local values of the Nusselt number depending on the dimensionless radial coordinate  $r/d$ . Katti et al. (2011) published these values for the various values of the Reynolds number and also for various distances  $z/d$  including  $z/d = 1$ . Since I do



■ **Figure 5.17:** Mean values of Nusselt number depending on Reynolds number. Solid lines correspond to the correlations of Lytle and Webb for different averaging area. The dashed line corresponds to deviations from the correlation of  $\pm 10\%$ .

not have measured data for exactly the same values of Reynolds number, I decided to compare normalized values of Nusselt numbers  $Nu_N$  according to Eq. (4.62) and I believe that their dependencies do not change much in the narrow area of Reynolds numbers. Comparing the local values of the Nusselt number (see Fig. 5.18) we can see that the values are very good with those of Katti, only the location of the local maximum differs.



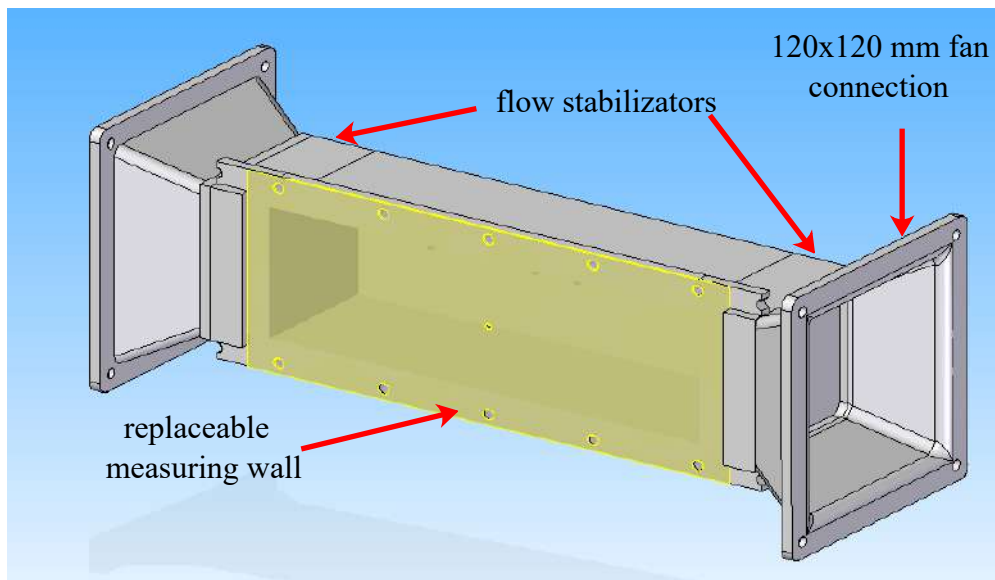
■ **Figure 5.18:** Comparison of local values of Nusselt numbers in dependence on dimensionless radial coordinate  $r/d$ . Katti et al. (2011) presented data for  $Re = 20000$ , our experimental data are for  $Re = 19600$ .

Dependencies of local values of Nusselt numbers for other Reynolds numbers look very similar, still with different location of local maximum, which in our case is closer to the axis.

Despite all slight deviations of the measured data from the literature, the heat flux jump method seems to be functional as a stand-alone measuring method. This is a very simple method that does not require too much laboratory techniques. The results and sensitivity analysis show that it is suitable only for low values of heat transfer coefficient, mainly for gas flows. For higher heat transfer coefficients, the insensitivity and error of the method increases very quickly and is unusable. The results of using the heat flux jump method are also shown in Solnař et al. (2020).

## 5.7 Wind tunnel

As part of testing the method, I also tested measurements in a small wind tunnel, whether the method allows to measure the intensity of heat transfer (or later conversion to the velocity field) during the flow around the bodies. For this experiment, I prepared a design of a small wind tunnel with internal dimensions of  $60 \times 60$  mm and a length of 200 mm, which would be modular and could be extended in length. Due to the size of such a tunnel, it was possible to manufacture it on a 3D printer, so other details depended on this technology. I also prepared a replaceable measuring wall for the tunnel so that it could be used both for an IR camera and for layer of thermochromic liquid crystals (TLC). A 3D model of a wind tunnel can be seen in Fig. 5.19.



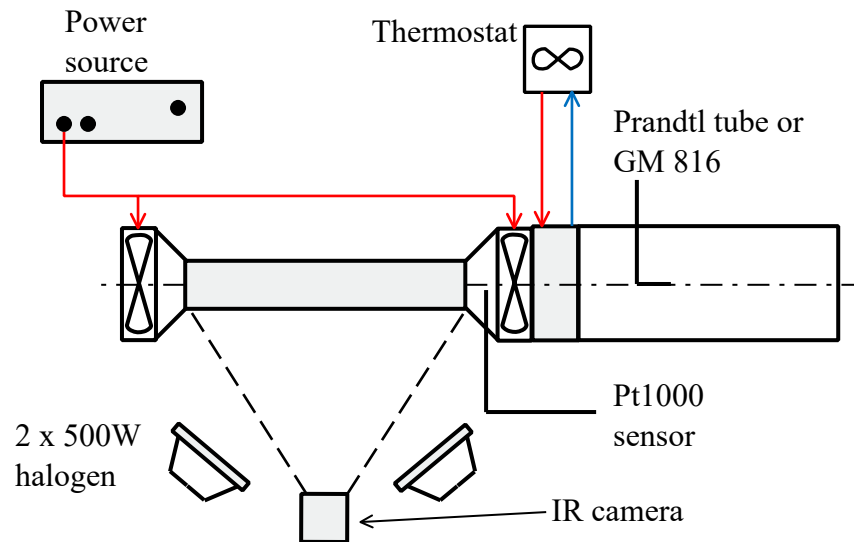
■ **Figure 5.19:** 3D model of a wind tunnel design with a replaceable measuring wall.

The wind tunnel is designed for being driven by a pair of axial fans with dimensions of  $120 \times 120$  mm (standard pc fan) and for the connection of other components such as speed measurement or connection of a finned heat exchangers. Flow stabilizers (grid,  $5 \times 5$  mm and

30 mm long) are installed at the inlet and outlet, as is the case with most large wind tunnels. The setting allows me to operate the tunnel as overpressure, underpressure or equal pressure.

To drive the air, I use a pair of axial fans (SunOn, 12 V, 1.6 A), which are powered by a laboratory source with an adjustable voltage output (max 30 V). This allows me to very precisely control the flow rate in the tunnel.

For measuring lower speeds I use a propeller anemometer (Benetech GM 816, 0-30 m/s,  $\pm 5\%$ ), for higher speeds I use a Prandtl tube (2-90 m/s,  $\pm 1\%$ ) connected to the Ahlborn Almemo 2590 station. Before the air entered the first axial fan, I installed a finned heat exchanger, which was connected to a water thermostat to maintain a constant temperature that flows into the tunnel. The temperature of the flowing air was measured with a Pt 1000 thermometer and then the corresponding thermophysical properties were found in literature. The details of the measurement are shown in Fig. 5.20.



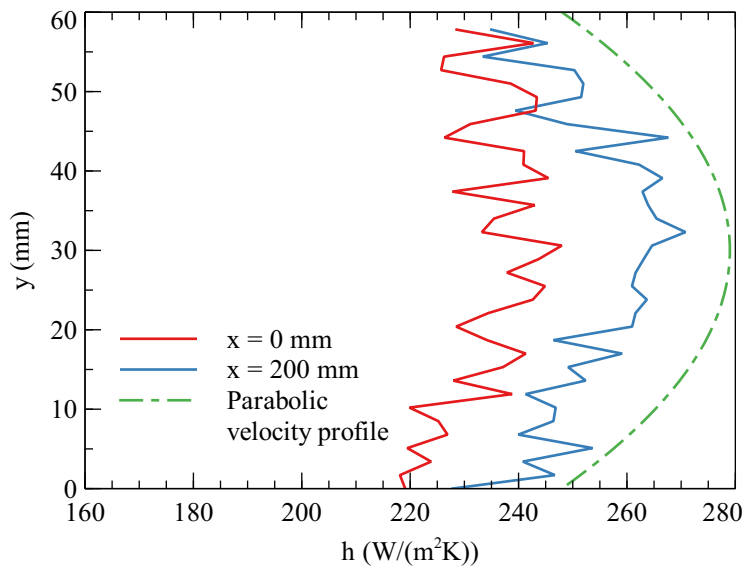
■ **Figure 5.20:** Schematic drawing of an experiment for measuring heat transfer during the flow around bodies in a wind tunnel.

The measuring wall was made of the same material and thickness as in the case of measuring the heat transfer between the smooth wall and the impinging air jet. The outer side of the measured wall was sprayed with a thin layer of matt black paint for higher and constant emissivity of the surface.

The first experiment was performed without any internal installation (object) to determine whether the method for such a geometry works and whether it shows, for example, the development of the internal velocity profile.

In the Fig. 5.21, I plotted the heat transfer coefficient profiles as a function of the vertical coordinate  $y$  at the beginning and end of the wind tunnel. We can notice that the profile changes, at the end of the tunnel it is quite similar to the parabolic velocity profile and at the entrance to the tunnel we can say (with a little imagination) that it is practically constant. The heat

transfer coefficient profiles can be converted to velocity profiles with a suitable correlation, most correlations work in a turbulent flow mode with an exponent at the Reynolds number 0.8, so we can expect a slight change in the shape of the velocity profile.



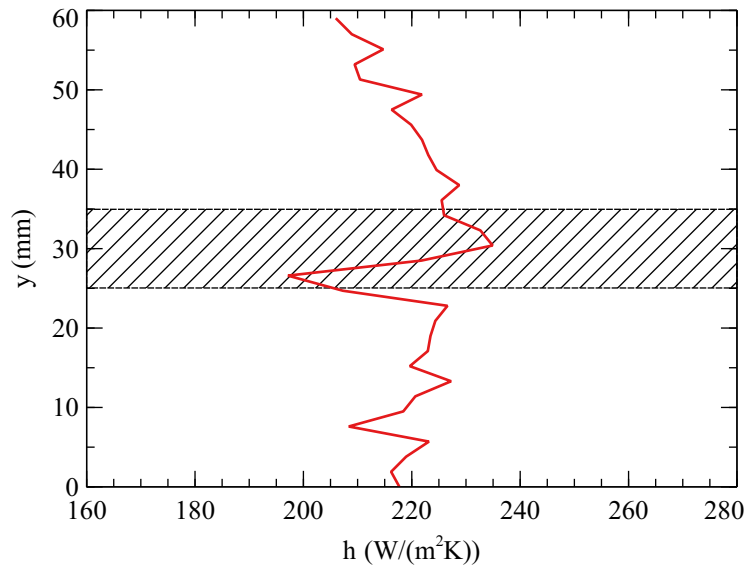
■ **Figure 5.21:** Profiles of the heat transfer coefficient at the inlet ( $x = 0$  mm) and outlet ( $x = 200$  mm) to and from the wind tunnel and illustrative comparison with a parabolic velocity profile. Inlet velocity 10.2 m/s.

Measurements in a tunnel with this method can capture the change in the profile of the heat transfer coefficient in the tunnel without any object. I tried another measurement from the simplest geometry and that is the flow around the cylinder. I placed a cylinder with a diameter of 10 mm in the middle of the measuring section of the wind tunnel and fastened it on both sides with screws. The change of the heat transfer coefficient profile with the  $y$  coordinate can be seen in Fig. 5.22. As can be seen, the change in the heat transfer intensity profile is minimal, barely visible. From the point of view of the overall map of the intensity of heat transfer, it is practically impossible to find the object.

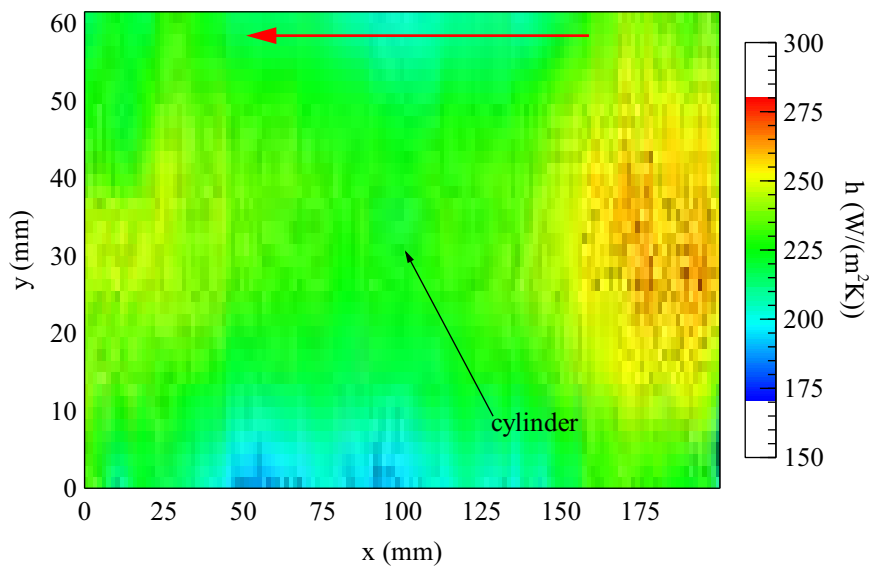
Practically the same situation occurred when I inserted a cylinder with a diameter of 30 mm into the tunnel and tested the measurement with such a large object. It seems that the change in the intensity of heat transfer during the flow around the cylinder at such low speeds (up to 15 m/s) is so small that an IR camera with a given sensitivity and inaccuracy is not possible to record this change (see Fig. 5.23).

To increase the sensitivity of the measured temperature of the scanned wall, I tried to use a TLC layer, which has many times higher sensitivity than the IR camera we use. The high sensitivity to temperature change of the TLC layer is connected to a relatively small range of measured temperatures, so it is necessary to give some time to find the optimal setting of the incident heat flux and the temperature of the flowing air in the tunnel for preparing clearly visible results.

Photograph from the measurements of the same experiment with the TLC layer can be seen in Fig. 5.24, where it is relatively easy to see the over-flowed body and also the temperature



■ **Figure 5.22:** Profile of the heat transfer coefficient in the axis of the over-flowed cylinder (at distance  $x = 100$  mm) with a marked cylinder with a diameter of 10 mm.

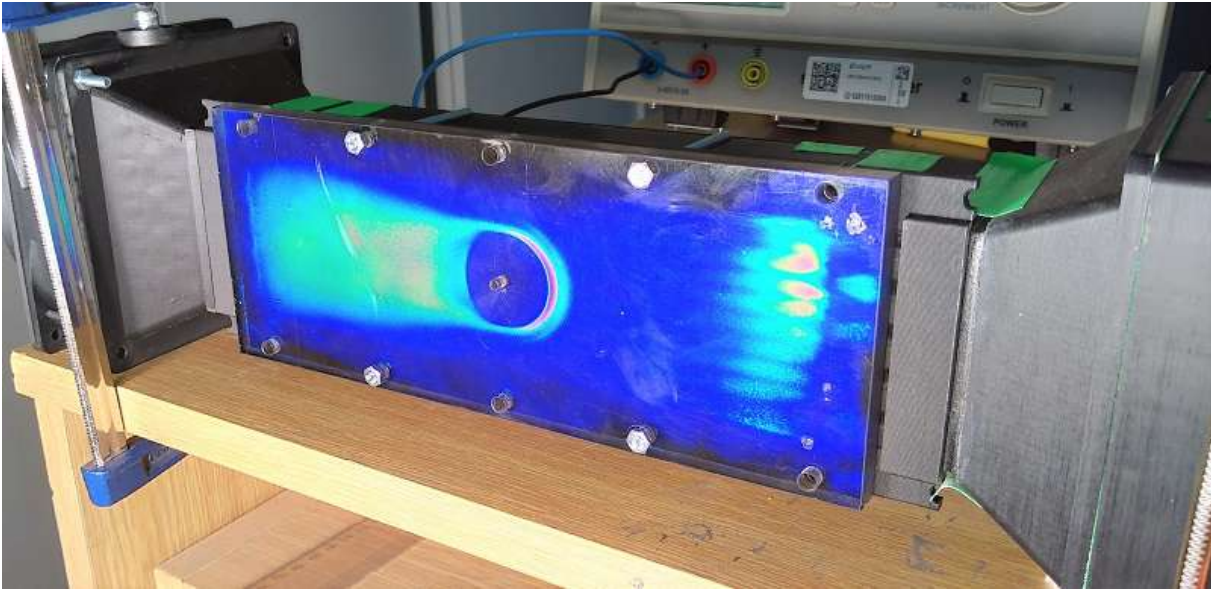


■ **Figure 5.23:** Map of the intensity of heat transfer during the flow experiment in the wind tunnel where the cylinder was installed. Inlet velocity 20.4 m/s. The red line represents the direction of air flow.

profile that is formed around the object.

With several times more sensitive temperature measurement, it is therefore possible to monitor geometries such as the wind tunnel. Due to the fact that the dynamic behavior of the TLC layer I used is not yet known, it is not possible to evaluate the results from measurements with the TLC layer.

For this application, therefore, my new method seems to be unusable with a normal IR camera, which we commonly use, and it is necessary to find an IR camera that has an order of



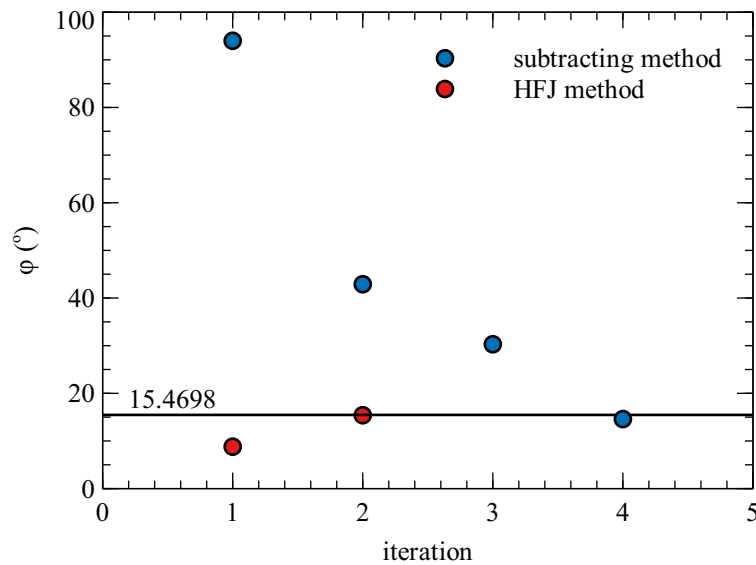
■ **Figure 5.24:** Photo from measurements in a wind tunnel with a TLC layer during the flow around the cylinder.

magnitude higher sensitivity to temperature changes.

## 5.8 Application to oscillation method

I also tried to apply the analytical results from the heat flux jump method to the measured results from the temperature oscillation method. During the application I chose to subtract the measured data from the TOIRT method from the individual analytical results and to observe the square of deviations (practically the same as in the evaluation of the heat flux jump method).

I considered the minimum difference between the measured data and the analytical solution to be a correctly fitted curve. The measured data was subtracted from this curve and the adjusted data was then evaluated as in the subtraction method (original method).



■ **Figure 5.25:** Evaluated phase delay as a function of the number of read iterations on the original data. The black line represents the correctly evaluated phase delay value.

Fig. 5.25 shows that both methods evaluate practically the same results. However, a method that subtracts analytical results from the data shows a faster way to the correct value and only needs two iterations, whereas the original method requires approximately twice the iterations. Therefore, applying this method to evaluating data from the TOIRT method could save processing time.

Overall, the heat flux jump method can be summarized as a functional free-standing method for measuring local values of the heat transfer coefficient. This method seems to be suitable only for smaller values of the heat transfer coefficient, where its insensitivity is within reasonable limits. For higher values of the heat transfer coefficient, the method error increases very quickly and is therefore not applicable.

When applied to TOIRT method and evaluating the data from this method, this procedure shows practically the same results as the original procedure. The only advantage is, by using a new procedure (subtracting from analytical results), that the correct values can be achieved with fewer iterations and thus save computational time.



# Chapter 6

## Future research

Further research of both completely contactless methods Heat flux jump and TOIRT will be focused mainly on:

- **Transient characteristics of radiative heat flux sources**

In the future focus, a more perfect description of the transient characteristics of the halogen lights used is planned, as well as a description of their behavior during the aging of the lights. In the case of unpredictable behavior, I will try to find an alternative source of radiative heat flux that would not have these properties. I have already found special red halogen bulbs that emit at the edge of visible light primarily into thermal radiation, which should have this aging effect suppressed.

- **Use of thermochromic liquid crystals (TLC) in measurement**

Calibrated TLCs are already commonly used in academic world to accurately measure the surface temperatures of objects. Application to dynamic heat transfer measurement methods would be a new, as yet unexplored area, which, however, brings with it other problems such as: light reflections, a relatively small range of measured temperatures, chemical non-resistance or susceptibility to breakage. As part of my doctoral studies, I have already eliminated some problems, but there is still a long way to go to real application.

The main advantage of such a measurement would be a much higher sensitivity of temperature measurement, because TLC layers are usually 3–5 times more sensitive to temperature change than a conventional IR camera. Probably the biggest obstacle seems to be the transient characteristic of the TLC layer itself, which should serve as an immediate indicator of surface temperature. I will focus on the dynamic behavior of TLC.

- **Wind tunnels and velocity profiles measurement**

Wind tunnels are now commonly used in industry to optimize the geometry of various products. My new non-contact method could be used for indirect measurement of velocity fields in such tunnels and thus help in optimizing geometries.



# Chapter 7

## Conclusion

In this work, local values of heat transfer coefficient for various geometric systems were experimentally measured. Two different methods were used to measure these local values, namely the temperature oscillation method (TOIRT) and the heat flux jump method (HFJ). Methods use a different exciting function, but some aspects are the same for them. Both methods are:

- very simple and quick to evaluate,
- fully contactless,
- without having to measure the temperature of the fluid,
- and with selectable spatial resolution

The sensitivity analysis of the temperature oscillation method shows that the method with a reasonable error is applicable in the measurement range  $100 - 3000 \text{ W/m}^2\text{K}$  and I determined from the numerical analysis the minimum number of thermal oscillations for the measurement. The method was numerically confirmed and experimentally validated on probably the best known heat transfer experiment, the flow in the tube which is a very simple flow mostly in one direction. This geometry has been measured many times by various researchers and the most frequently cited correlation is Gnielinski's, mostly accompanied by Hausen's correction for short tubes. In experiments I tried different settings of temperature oscillations, different materials of the measured wall and also different dimensions to confirm the independence of the method on these factors. Most of our measured results can be described by Gnielinski's correlation with an error of up to 20%, which corresponds approximately to the method error in this region of the heat transfer coefficient. The maximum measured error was less than 40%.

The move to more complex geometries was the heat transfer measurement between the smooth wall and the impinging water jet. The method has already been applied to similar geometry and I have achieved excellent results compared to literature. The results show that the method is suitable for measuring such geometries both in terms of average values and local values of heat transfer coefficient.

Experiments on a very complex system such as a vessel with an agitator were divided to measure the heat transfer coefficient at the bottom and wall of the vessel. For various geometries of such a system, a large amount of data was obtained for both axial and radial types of agitators. The results at the bottom of the vessel are very well in line with the literature, even the results of experiments with the agitator placed in the draft tube show good agreement. In addition, in this measurement, I discovered two areas that differed substantially in the Reynolds number exponent, which is mostly associated with changing the flow mode from laminar to turbulent.

I did not achieve such good results on the wall of the vessel with an agitator. The results of experimental measurements, especially the exponent of the Reynolds number, differ from the literature, although the absolute values are in the same range and the local shapes of the Nusselt number are very similar. The data are very consistent with the calculated correlation. The measurement on the wall is likely to be influenced by many factors such as a very complex flow, the emergence of macro vortices and the fact that both the radial and axial stirrers create minor by-flows. All these issues can lead to incorrect results.

Inspired by the temperature oscillation method, I decided to derive my own method that would be easier for experimental techniques. The heat flux jump method calculates the heat transfer coefficient from the measured response of the surface temperature to the sudden change in the heat flux (Heaviside function) that impacts the measured wall. The derivation also serves as a description of the transient effect in the oscillation method and thus allows to use the measured data, which would otherwise be deleted.

Sensitivity analysis showed that this method is suitable only for low values of heat transfer coefficient, above  $1000\text{W}/\text{m}^2\text{K}$  its insensitivity and measurement error grows very quickly. For these reasons I have prepared an experiment of the impinging air jet, where I assume lower values of the heat transfer coefficient. Experimental results correlate very well with literature, only when comparing local values the local maximum in my case is different from the literature. Nevertheless, the method is functional and shows good results.

In addition to the stand-alone measurement method, this procedure also allows the distribution of incident heat flux to be measured. If the other side of the measured wall is thermally insulated, there is only one variable left in the derivation, namely the heat flux, so it is possible to measure these values experimentally.

Future research will focus primarily on the perfect description of the transient characteristics of heat flux sources, which will affect the accuracy of experimental results. Next, I will deal with the application of heat flux jump method on a more complicated system with complex flow, but again on measuring the heat transfer coefficient in air. The possibility of measuring the distribution of incident heat flux is already used in the installation of experiments to ensure that the heat flux is as uniform as possible and that the assumptions of the method are best met. In the future I also want to focus on the possibility to replace quite expensive IR cameras with a TLC layer, which is much cheaper, but with a limited range of measured temperatures.

## Chapter 8

### References



- Abate, J., Whitt, W., 2006. A unified framework for numerically inverting laplace transforms. *Inform journal on computing* 18, 408–421. doi:10.1287/ijoc.1050.0137.
- Ahadi, A., Saghir, M.Z., 2014. An extensive heat transfer analysis using mach zehnder interferometry during thermodiffusion experiment on board the international space station. *Applied Thermal Engineering* 62, 351–364.
- Bhattacharya, P., Nara, S., Vijayan, P., Tang, T., Lai, W., Phelan, P., Prasher, R., Song, D., Wang, J., 2006. Characterization of the temperature oscillation technique to measure the thermal conductivity of fluids. *International Journal of Heat and Mass Transfer* 49, 2950–2956.
- Bokert, R.R.G., Johnson, E.E., 1948. Studies on heat transfer in laminar free convection with the Zhender-Mach interferometer. Technical Report 5747. United States Air Force.
- Carloff, R., Pross, A., Reichert, K.H., 1994. Temperature oscillation calorimetry in stirred tank reactors with variable heat transfer. *Chemical Engineering and Technology* 17, 406–413. doi:10.1002/ceat.270170608.
- Chemieingenieurwesen, V.G.V. (Ed.), 2010. VDI heat atlas; 2nd ed. Landolt-Börnstein. Additional resources, Springer, Berlin.
- Cudak, M., Karcz, J., 2008. Distribution of local heat transfer coefficient values in the wall region of an agitated vessel. *Chemical Papers* 62, 92–99. doi:10.2478/s11696-007-0084-6.
- Cummings, G.H., West, A.S., 1950. Heat transfer data for kettles with jackets and coil. *Industrial and Engineering Chemistry* 69, 2303–2313. doi:10.1021/ie50491a035.
- Czarnetzki, W., Roetzel, W., 1995. Temperature oscillation techniques for simultaneous measurement of thermal diffusivity and conductivity. *International Journal of Thermophysics* 16, 413–422.
- Debab, A., Chergui, N., Bekrentchir, K., Bertrand, J., 2011. An investigation of heat transfer in a mechanically agitated vessel. *Journal of Applied Fluid Mechanics* 4, 43–50.
- Dostál, M., Petera, K., Rieger, F., 2010. Measurement of heat transfer coefficients in an agitated vessel with tube baffles. *Acta Polytechnica* 50, 47–57.

- Dostál, M., Petera, K., Solnař, S., 2018. Gnielinski's correlation and a moder temperature-oscillation method for measuring heat transfer coefficients, in: Dančová, P. (Ed.), Proceedings of the Experimental Fluid Mechanics, Prague, Czech Republic, pp. 111–122.
- Freund, S., 2008. Local Heat Transfer Coefficients Measured with Temperature Oscillation IR Thermography. Ph.D. thesis. Helmut-Schmidt-Universität, Universität der Bundeswehr Hamburg.
- Glaser, H., 1938. Der warmeubergang in regeneratoren. Z. VDI, Beiheft Verfahrenstechnik 4, 112–125.
- Hagedorn, D.W., 1965. Prediction of batch heat transfer coefficients for pseudoplastic fluids in agitated vessels. Ph.D. thesis. Newark College of Engineering. 186 Bleeker St., Newark, New Jersey.
- Han, J.C., Park, J.S., 1988. Developing heat transfer in rectangular channels with rib turbulators. *International Journal of Heat and Mass Transfer* 31, 183–195.
- Hauke, G., 2008. *An Introduction to Fluid Mechanics and Transport Phenomena*. Springer.
- Hausen, H., 1976. *Wärmeübertragung im Gegenstrom, Gleichstrom und Kreuzstrom*. 2 ed., Springer, Berlin.
- Herchang, A., Yuh, J.J., Jer-Nan, Y., 2002. Local heat transfer measurements of plate finned-tube heat exchangers by infrared thermography. *International Journal of Heat and Mass Transfer* 45, 4069–4078.
- Incropera, F.P., Dewitt, D.P., Bergman, T.L., Lavine, A.S., 2007. *Fundamentals of Heat and Mass Transfer*. 6 ed., John Wiley and Sons.
- Ingole, S.B., Sundaram, K.K., 2016. Experimental average nusselt number characteristics with inclined non-confined jet impingement of air for cooling application. *Experimental Thermal and Fluid Science* , 124–131doi:10.1016/j.expthermflusci.2016.04.016.
- Ishibashi, K., Yamanaka, A., Mitsuishi, N., 1979. Heat transfer in agitated vessels with special types of impellers. *Journal of Chemical Engineering of Japan* 12, 230–235.
- Jainski, C., Lu, L., Sick, V., Dreizler, A., 2014. Laser imaging investigation of transient heat transfer processes in turbulent nitrogen jets impinging on a heated wall. *International Journal of Heat and Mass Transfer* , 101–112doi:10.1016/j.ijheatmasstransfer.2014.02.072.
- Karcz, J., 1999. Studies of local heat transfer in a gas–liquid system agitated by double disc turbines in a slender vessel. *Chemical engineering journal* 72, 217–227.
- Karcz, J., Cudak, M., 2007. Studies of local heat transfer at vicinity of a wall region of an agitated vessel. *Proc. 34th International conference of SSCHE 2007* , 029/1 – 029/10.

- Kast, W., 1965. Messung des wärmeüberganges in haufwerken mit hilfe einer temperaturmodulierten stormung. *Allg. Warmetech* 12, 119–125.
- Katti, V.V., Prabhu, S.V., 2008. Experimental study and theoretical analysis of local heat transfer distribution between smooth flat surface and impinging air jet from a circular straight pipe nozzle. *International Journal of Heat and Mass Transfer* , 4480–4495doi:10.1016/j.ijheatmasstransfer.2007.12.024.
- Katti, V.V., Yasaswy, S.N., Prabhu, S.V., 2011. Local heat transfer distribution between smooth flat surface and impinging air jet from a circular nozzle at low reynolds numbers. *Heat Mass Transfer* , 237–244doi:10.1007/s00231-010-0716-1.
- Kupčák, F., 1974. Heat transfer on the wall and bottom in containers with impellers (in czech). *Chemický průmysl* 24, 491–494.
- Langhans, W.U., 1952. Wärmeübergang und druckverlust in regeneratoren mit rostgitterartiger speichermasse. *Arch. Eisenhüttenw* 33, 347–353 and 441–451.
- Lehner, M., Mewes, D., Dingreiter, U., Tauscher, R., 1999. *Applied Optical Measurements*. Springer.
- Lytle, D., Webb, B.W., 1994. Air jet impingement heat transfer at low nozzle-plate spacings. *International Journal of Heat and Mass Transfer* 37, 1687–1697.
- Matulla, H., Orlicek, A.F., 1971. Bestimmung der wärmeübergangskoeffizienten in einem dopplerrohrwärmeaustauscher durch frequenzganganalyse. *Chemi-Ing. Techn.* 43, 1127–1130.
- Nebuchinov, A.S., Lozhkin, Y.A., Bilsky, A.V., Markovich, D.M., 2017. Combination of piv and plif methods to study convective heat transfer in an impinging jet. *Experimental Thermal and Fluid Science* , 139–146doi:10.1016/j.expthermflusci.2016.08.009.
- Newton, P.J., Yan, Y., Stevens, N.E., Evatt, S.T., Lock, G.D., Owen, J.M., 2003. Transient heat transfer measurements using thermochromic liquid crystal. part 1: An improved technique. *International Journal of Heat and Fluid Flow* 24, 14–22.
- Nusselt, W., 1916. The combustion and gasification of coal on the grid (in german, reprint). *Z. Ver. Dtsch. Ing.* 60, 359–369.
- Pereyra, M.C., Ward, L.A., 2012. *Harmonic Analysis From Fourier to Wavelets*. Student Mathematical Library.
- Persoons, T., Balgazin, K., Brown, K., Murray, D.B., 2013. Scaling of convective heat transfer enhancement due to flow pulsation in an axisymmetric impinging jet. *JOURNAL OF HEAT TRANSFER-TRANSACTIONS OF THE ASME* 135, HT/12/1301.
- Petera, K., and M. Věříšová, M.D., Jirout, T., 2017. Heat transfer at the bottom of a cylindrical vessel impinged by a swirling flow from an impeller in a draft tube. *Chem. Biochem. Eng.* 31, 343–352.

- Ramirez, J.A., Timmerhaus, K.D., Radebaugh, R., 1997. Application of the periodic temperature variation technique to the measurement of heat transfer coefficients in high-ntu matrices. *Cryocoolers* , 441–452.
- Rieger, F., Novák, V., Jirout, T., 2005. *Hydromechanical processes II* (in Czech). CTU in Prague.
- Roetzel, W., 1989. Measurement of heat transfer coefficients in tubes by temperature oscillation analysis. *Chem. Eng. Technol.* 12, 379–387.
- Roetzel, W., Das, S.K., Luo, X., 1994. Measurement of the heat transfer coefficient in plate heat exchangers using a temperature oscillation technique. *International Journal of Heat and Mass Transfer* 37, 325–331.
- Roetzel, W., Prinzen, S., 1991. Measurement of local heat transfer coefficients using temperature oscillations, in: Keffer, J.F., Shah, R.K., Ganic, E.N. (Eds.), *Experimental Heat Transfer, Fluid Mechanics, and Thermodynamics*, p. 497.
- Rohsenow, W.M., Harnett, J.P., Cho, Y.I. (Eds.), 1998. *Handbook of Heat Transfer*, 3rd ed. McGraw-Hill.
- Solnař, S., 2016. Heat transfer measurement using the oscillation method (in Czech). Master's thesis. Czech Technical University in Prague. Technická 4.
- Solnař, S., Dostál, M., 2019. Heat flux jump method as a possibility of contactless measurement of local heat transfer coefficients. *Acta Polytechnica* 59, 411–422. doi:10.14311/AP.2019.59.0411.
- Solnař, S., Dostál, M., Jirout, T., 2018a. Heat transfer measurements with temperature oscillation method, in: Kruczek, B. (Ed.), *Proceedings of the 5th International Conference of Fluid Flow, Heat and Mass Transfer, Niagara Falls, Canada*, pp. 118/1–118/2. doi:10.11159/ffhmt18.118.
- Solnař, S., Dostál, M., Jirout, T., 2019. Local values of heat transfer coefficient at the bottom of an agitated vessel measured with toirt method, in: Meyer, J.P. (Ed.), *Proceedings of the 14th International Conference on Heat Transfer, Fluid Mechanics and Thermodynamics, Wicklow, Ireland*, pp. 336–341.
- Solnař, S., Dostál, M., Jirout, T., 2020. A novel contactless transient method for measuring local values of heat transfer coefficient. *Heat and Mass Transfer* (in print) .
- Solnař, S., Dostál, M., Petera, K., Jirout, T., 2018b. Application of the temperature oscillation method in heat transfer measurements at the wall of an agitated vessel. *Acta Polytechnica* 58, 144–154. doi:10.14311/AP.2018.58.0144.
- Solnař, S., Petera, K., Dostál, M., Jirout, T., 2016. Heat transfer measurements with toirt method, in: Dančová, P. (Ed.), *Proceedings of the Experimental Fluid Mechanics, Mariánské Lázně, Czech Republic*, p. 734.

- Stang, J.H., Bush, J.E., 1974. The periodic method for testing compact heat exchanger surfaces. *J. Eng. Power* 96, 87–94.
- Taler, D., 2016. A new heat transfer correlation for transition and turbulent fluid flow in tubes. *International Journal of Thermal Sciences* 108, 108–122. doi:10.1016/j.ijthermalsci.2016.04.022.
- Tydlitát, V., Jadavan, J., Augusta, I., 1977. Absolute heat transfer coefficient measurement method and apparatus for making them (in Czech). Technical Report. No. 168975.
- Věříšová, M., Dostál, M., Jirout, T., Petera, K., 2015. Heat transfer in a jacketed agitated vessel equipped with multistage impellers. *Chemical Papers* 69, 690–697. doi:10.1515/chempap-2015-0080.
- Šesták, J., Bukovský, J., Houška, M., 1996. Heat processes. Transport and thermodynamic data. Publishing Czech Technical University in Prague, Prague. In Czech.
- Wandelt, M., Roetzel, W., 1997. Lockin thermography as a measurement technique in heat transfer. *Quantitative Infra-Red Thermography*, 189–194. doi:10.21611/qirt.1996.031.
- Wiberg, R., Lior, N., 2005. Heat transfer from a cylinder in axial turbulent flows. *International Journal of Heat and Mass Transfer* 48, 1505–1517. doi:10.1016/j.ijheatmasstransfer.2004.10.015.
- Willmott, A.J., 1993. The development of thermal regenerator theory from 1931 to the present. *J. Inst. Energy* 66, 54–70.
- Yi, S.J., Kim, M., Kim, D., Kim, H.D., Kim, K.C., 2016. Transient temperature field and heat transfer measurement of oblique jet impingement by thermographic phosphor. *International Journal of Heat and Mass Transfer* 102, 691–702. doi:10.1016/j.ijheatmasstransfer.2016.06.062.
- Zuckerman, N., Lior, N., 2006. Jet impingement heat transfer: Physics, correlations, and numerical modeling. *Advances in Heat Transfer* 39, 565–631.

## Authors references

- [1] Solnař, S. Heat transfer measurement using the oscillation method (in Czech): Diplomová práce. Praha: České vysoké učení technické v Praze, 2016.
- [2] Solnař, S., Dostál, M. Heat flux jump method as a possibility of contactless measurement of local heat transfer coefficients. *Acta Polytechnica*, 2019, vol. 59, p. 411–422.
- [3] Solnař, S., Dostál, M., Jirout, T., 2018a. Heat transfer measurements with temperature oscillation method, in: Kurczek, B. (Ed.), *Proceedings of the 5th International Conference of Fluid Flow, Heat and Mass Transfer, Niagara Falls, Canada*, pp. 118/1-118/2. doi:10.11159/ffhmt18.118.

- [4] Solnař, S., Dostál, M., Jirout, T., 2019. Local values of heat transfer coefficient at the bottom of an agitated vessel measured with toirt method, in: Meyer, J. P. (Ed.), Proceedings of the 14th International Conference on Heat Transfer, Fluid Mechanics and Thermodynamics, Wicklow, Ireland, pp. 336-341.
- [5] Solnař, S., Dostál, M., Jirout, T., 2020. A novel contactless transient method for measuring local values of heat transfer coefficient. Heat and Mass Transfer. (in print) IF: 1.867, 5y IF: 1.852
- [6] Solnař, S., Dostál, M., Petera, K., Jirout, T., 2018b. Application of the temperature oscillation method in heat transfer measurements at the wall of an agitated vessel. Acta Polytechnica 58, 144–154. doi:10.14311/AP.2018.58.0144.
- [7] Solnař, S., Petera, K., Dostál, M., Jirout, T., 2016. Heat transfer measurements with toirt method, in: Dančová, P. (Ed.), Proceedings of the Experimental Fluid Mechanics, p. 734.
- [8] Dostál, M., Petera, K., Solnař, S., 2018. Gnielinski's correlation and a moder temperature oscillation method for measuring heat transfer coefficients, in: Dančová, P. (Ed.), Proceedings of the Experimental Fluid Mechanics, Prague, Czech Republic, pp. 111-122.
- [9] Solnař, S., 2016. Aplikace metody teplotních oscilací pro měření součinitele přestupu tepla, in Studentská tvůrčí činnost. ISBN 978-80-01-05929-6.

## **RESPONSES**

Usage of [6]: Liaposhchenko, O. et al, 2019. Improvement of Parameters for the Multi-Functional Oil-Gas Separator of 'HEATER-TREATER' Type, in: 2019 IEEE 6th International Conference on Industrial Engineering and Applications, ICIEA 2019

Total citations: 3 (excluded self citations)

*h*-index = 1

# Chapter 9

## Appendix

### Heat flux jump method - calculation using time constant

```
clear all; format compact; clc;
data = importdata('dataset.mat');
tmax = 80;
freq = 10;
data = data(:, :, 1:tmax*freq);
fun = @(a,x) a(1)*(1-exp(-x/a(2)))+a(3);

D = load('calculated-tau-vs-alfa-set.txt');
tauset = D(:,2);
alfaset = D(:,1);

for x=1:120 %Spatial resolution of IR camera
for y=1:160
t=linspace(0.1,tmax,tmax*freq);
T=squeeze(data(x,y,:));
T=transpose(T);
result(x,y,:)=nlinfit(t,T,fun,[10 10 10]);
tau(x,y)=result(x,y,2);
clear T t

htc(x,y)=interp1(tauset,alfaset,tau(x,y));

end
end

surf(htc)
```

## Heat flux jump method - calculation using minimum difference

```
clear all; format compact; clc;
data = importdata('dataset.mat');
tmax = 40; %optional
freq = 10;
data = data(:, :, 1:tmax*freq);
Tan = importdata('calculated-analytical-temperature-set.mat');
Tan = Tan(:, 1:tmax*freq);

for x=1:120 %Spatial resolution of IR camera
for y=1:160
Tex = transpose(squeeze(data(x,y,:)));
Tex = Tex - Tex(1);
Te = Tex./max(Tex);

for c = 1:100
Ta = Tan(c, :);
Ta = Ta - Ta(1);
Ta = Ta./max(Ta);
error(x,y,c) = sum(Ta-Te).^2;
end

[v(x,y), loc]=min(error(x,y,:));
[ap, jj, kk]=ind2sub(size(error), loc);
htc(x,y)=ap;

end
end

mean = mean(mean(htc))
min = min(min(htc))
max = max(max(htc))
stdev = std(alfa(:))
surf(htc)
```

## Calculation of analytical temperature change using Talbot algorithm

```
clear all; format compact; clc d=0.001;l=15;cp=500;rho=7900;
zstar=1;q=8000;
a=1/(rho*cp);
alfa0=3; Bi0=alfa0*d/l;
```

```

t = linspace(0.0001,40,400);
time = (a*t)/(d^2);

for i=1:2000
alfad = i*1;
Bid=alfad*d/l;
funT = @(s) ( ((-q.*d./(s.*l)).*(sqrt(s).*sinh(sqrt(s))...
+Bid.*cosh(sqrt(s))))... C1detA
/ ( sqrt(s).(sqrt(s).*sinh(sqrt(s))+Bid.*cosh(sqrt(s)))...
-Bi0.*(sqrt(s).*cosh(sqrt(s))+Bid.*sinh(sqrt(s))) ) )... /detA
*sinh(zstar*sqrt(s)) + ...
( ( (q.*d./(s.*l)).*(sqrt(s).*cosh(sqrt(s))...
+Bid.*sinh(sqrt(s))) )... C2detA
/ ( sqrt(s).(sqrt(s).*sinh(sqrt(s))+Bid.*cosh(sqrt(s)))...
-Bi0.*(sqrt(s).*cosh(sqrt(s))+Bid.*sinh(sqrt(s))) ) )... /detA
* cosh(zstar*sqrt(s)));
Ta(i,:) = talbot_inversion(funT,time,128);
end

```

## Measured datasets

### Oscillating method

**001** - bottom of an agitated vessel with baffles,  $D = 392$  mm,  $H = 392$  mm,  $B = 40$  mm  
 $D/d = 3$ ,  $H_2/d = 0.75$ , 6PBT45 axial impeller

10×10 s oscillations @ 10Hz, 4×500W

Temperatures measured:  $384 \times 10^6$

**002** - bottom of an agitated vessel with baffles,  $D = 392$  mm,  $H = 392$  mm,  $B = 40$  mm  
 $D/d = 6.4$ ,  $H_2/d = 0.75$ , 6PBT45 axial impeller

10×10 s oscillations @ 10Hz, 4×500W

Temperatures measured:  $537 \times 10^6$

**003** - bottom of an agitated vessel with baffles,  $D = 392$  mm,  $H = 392$  mm,  $B = 40$  mm  
 $D/d = 6.4$ ,  $H_2/d = 0.75$ , 6PBT45 axial impeller

10×10 s oscillations @ 10Hz, 4×500W

Temperatures measured:  $883 \times 10^6$

**004** - bottom of an agitated vessel with baffles,  $D = 392$  mm,  $H = 392$  mm,  $B = 40$  mm  
 $D/d = 3$ ,  $H_2/d = 0.75$ , 6PBT45 axial impeller

10×10 s oscillations @ 10Hz, 4×500W

Temperatures measured:  $691 \times 10^6$

**005** - bottom of an agitated vessel, impeller in a draft tube,  $D = 392$  mm,  $H = 392$  mm,  
 $D/d = 6.4$ ,  $H_2/d = 1$ , 6PBT45 axial impeller in draft tube

10×10 s oscillations @ 10Hz, 4×500W

Temperatures measured:  $768 \times 10^6$

**006** - bottom of an agitated vessel, impeller in a draft tube,  $D = 392$  mm,  $H = 392$  mm,  
 $D/d = 6.4$ ,  $H_2/d = 0.5$ , 6PBT45 axial impeller in draft tube

10×10 s oscillations @ 10Hz, 4×500W

Temperatures measured:  $768 \times 10^6$

**007** - bottom of an agitated vessel, impeller in a draft tube,  $D = 392$  mm,  $H = 392$  mm,  
 $D/d = 6.4$ ,  $H_2/d = 0.25$ , 6PBT45 axial impeller in draft tube

10×10 s oscillations @ 10Hz, 4×500W

Temperatures measured:  $595 \times 10^6$

**008** - bottom of an agitated vessel, impeller in a draft tube,  $D = 392$  mm,  $H = 392$  mm,  
 $D/d = 6.4$ ,  $H_2/d = 1$ , 6PBT45 axial impeller in draft tube

15×10 s oscillations @ 10Hz, 4×500W

Temperatures measured:  $288 \times 10^6$

**009** - wall of an agitated vessel with baffles,  $D = 300$  mm,  $H = 300$  mm,  $D/d = 3$ ,  $H_2/d = 1$ ,  
6PBT45 axial impeller

10×10 s oscillations @ 10Hz, 4×500W

Temperatures measured:  $691 \times 10^6$

- 010** - wall of an agitated vessel with baffles,  $D = 300$  mm,  $H = 300$  mm,  $D/d = 3$ ,  $H_2/d = 1$ , Rushton turbine  
 $10 \times 10$  s oscillations @ 10Hz,  $4 \times 500$ W  
 Temperatures measured:  $211 \times 10^6$
- 011** - wall of an agitated vessel with baffles,  $D = 300$  mm,  $H = 300$  mm,  $D/d = 3$ ,  $H_2/d = 1$ , Rushton turbine  
 $7 \times 10$  s oscillations @ 10Hz,  $4 \times 500$ W  
 Temperatures measured:  $363 \times 10^6$
- 012** - wall of an agitated vessel without baffles,  $D = 300$  mm,  $H = 300$  mm,  $D/d = 3$ ,  $H_2/d = 1$ , Rushton turbine  
 $5 \times 20$  s oscillations @ 10Hz,  $4 \times 500$ W  
 Temperatures measured:  $288 \times 10^6$
- 013** - flow of water in pipe, copper tube  $26 \times 1$   
 $10 \times 10$  s oscillations @ 10Hz,  $2 \times 500$ W  
 Temperatures measured:  $365 \times 10^6$
- 014** - flow of water in pipe, copper tube  $26 \times 1$   
 $5 \times 20$  s oscillations @ 10Hz,  $2 \times 500$ W  
 Temperatures measured:  $192 \times 10^6$
- 015** - flow of water in pipe, copper tube  $26 \times 1$   
 $5 \times 20$  s oscillations @ 10Hz,  $2 \times 500$ W  
 Temperatures measured:  $249 \times 10^6$
- 016** - flow of water in pipe, copper tube  $26 \times 1$   
 $5 \times 20$  s oscillations @ 20Hz,  $2 \times 500$ W  
 Temperatures measured:  $768 \times 10^6$
- 017** - wall of an agitated vessel without baffles,  $D = 400$  mm,  $H = 400$  mm,  $D/d = 6.4$ ,  $H_2/d = 1$ , 6PBT45 axial impeller located in draft tube  
 $5 \times 20$  s oscillations @ 20Hz,  $6 \times 500$ W  
 Temperatures measured:  $652 \times 10^6$
- 018** - wall of an agitated vessel without baffles,  $D = 400$  mm,  $H = 400$  mm,  $D/d = 6.4$ ,  $H_2/d = 1$ , 6PBT45 axial impeller located in draft tube  
 $10 \times 10$  s oscillations @ 10Hz,  $6 \times 500$ W  
 Temperatures measured:  $460 \times 10^6$
- 019** - wall of an agitated vessel without baffles,  $D = 400$  mm,  $H = 400$  mm,  $D/d = 6.4$ ,  $H_2/d = 1$ , 6PBT45 axial impeller located in draft tube  
 $20 \times 10$  s oscillations @ 10Hz,  $6 \times 500$ W  
 Temperatures measured:  $576 \times 10^6$
- 020** - wall of an agitated vessel without baffles,  $D = 400$  mm,  $H = 400$  mm,  $D/d = 6.4$ ,

$H_2/d = 1$ , 6PBT45 axial impeller located in draft tube  
10×10 s oscillations @ 10Hz, 6×500W  
Temperatures measured:  $384 \times 10^6$

**021** - flow of water in pipe, copper tube 26×1, special red lights  
100×10 s oscillations @ 10Hz, 2×500W  
Temperatures measured:  $4224 \times 10^6$

**022** - flow of water in pipe, copper tube 26×1  
20×5 s oscillations @ 10Hz, 2×500W  
Temperatures measured:  $269 \times 10^6$

**023** - flow of water in pipe, copper tube 26×1  
10×20 s oscillations @ 10Hz, 2×500W  
Temperatures measured:  $384 \times 10^6$

**024** - flow of water in pipe, copper tube 26×1  
10×20 s oscillations @ 10Hz, 2×500W  
Temperatures measured:  $845 \times 10^6$

**025** - flow of water in pipe, copper tube 26×1  
10×20 s oscillations @ 10Hz, 2×500W  
Temperatures measured:  $461 \times 10^6$

**026** - flow of water in pipe, copper tube 26×1  
10×10 s oscillations @ 10Hz, 2×500W  
Temperatures measured:  $345 \times 10^6$

**027** - flow of water in pipe, stainless steel tube 35×1.5  
10×10 s oscillations @ 10Hz, 2×500W  
Temperatures measured:  $326 \times 10^6$

**028** - flow of water in pipe, stainless steel tube 35×1.5, laminar flow  
10×10 s oscillations @ 10Hz, 2×500W  
Temperatures measured:  $307 \times 10^6$

**029** - flow of water in pipe, stainless steel tube 35×1.5  
10×10 s oscillations @ 10Hz, 2×500W  
Temperatures measured:  $96 \times 10^6$

**030** - flow of water in pipe, stainless steel tube 35×1.5  
10×10 s oscillations @ 10Hz, 2×500W  
Temperatures measured:  $941 \times 10^6$

**031** - flow of water in pipe, stainless steel tube 35×1.5  
10×20 s oscillations @ 10Hz, 2×500W  
Temperatures measured:  $576 \times 10^6$

**032** - flow of water in pipe, stainless steel tube  $35 \times 1.5$   
10×8 s oscillations @ 10Hz, 2×500W  
Temperatures measured:  $322 \times 10^6$

**033** - flow of water in pipe, stainless steel tube  $35 \times 1.5$   
10×15 s oscillations @ 10Hz, 2×500W  
Temperatures measured:  $201 \times 10^6$

**040** - heat transfer between smooth wall and impinging water jet with gravitational force, pipe  
 $16 \times 1$ ,  $H_2/d = 0.5$   
10×10 s oscillations @ 10Hz, 4×500W  
Temperatures measured:  $115 \times 10^6$

### **Heat flux jump method**

**SQ001** - heat transfer between smooth wall and impinging air jet, pipe  $16 \times 1$ ,  $H_2/d = 0.5$   
80 seconds @ 10Hz, 4×500W  
Temperatures measured:  $920 \times 10^6$

**SQ002** - flow of air in pipe, stainless steel tube  $35 \times 1.5$   
80 seconds @ 10Hz, 4×500W  
Temperatures measured:  $368 \times 10^6$

**SQ003** - flow of air in pipe, stainless steel tube  $35 \times 1.5$   
80 seconds @ 10Hz, 4×500W  
Temperatures measured:  $368 \times 10^6$

**SQ004** - flow of air in pipe, stainless steel tube  $35 \times 1.5$   
80 seconds @ 10Hz, 4×500W  
Temperatures measured:  $169 \times 10^6$

**SQ005** - flow of air in pipe, stainless steel tube  $35 \times 1.5$   
80 seconds @ 10Hz, 4×500W  
Temperatures measured:  $460 \times 10^6$

**J001** - heat transfer between smooth wall and impinging air jet, pipe  $16 \times 1$ ,  $H_2/d = 1$   
80 seconds @ 10Hz, 4×500W  
Temperatures measured:  $92 \times 10^6$

**J002** - heat transfer between smooth wall and impinging air jet, pipe  $16 \times 1$ ,  $H_2/d = 1$   
80 seconds @ 10Hz, 4×500W  
Temperatures measured:  $108 \times 10^6$

**J003** - heat transfer between smooth wall and impinging air jet, pipe  $16 \times 1$ ,  $H_2/d = 1$   
80 seconds @ 10Hz, 4×500W  
Temperatures measured:  $108 \times 10^6$

**J004** - heat transfer between smooth wall and impinging air jet, pipe  $16 \times 1$ ,  $H_2/d = 1$

80 seconds @ 10Hz,  $4 \times 500\text{W}$

Temperatures measured:  $108 \times 10^6$

**J005** - heat transfer between smooth wall and impinging air jet, pipe  $16 \times 1$ ,  $H_2/d = 1$

80 seconds @ 10Hz,  $4 \times 500\text{W}$

Temperatures measured:  $230 \times 10^6$

**WT001** - heat transfer around cylinder in the wind tunnel,  $d = 10\text{mm}$  80 seconds @ 10Hz,  
 $2 \times 500\text{W}$

Temperatures measured:  $77 \times 10^6$

**WT002** - heat transfer around cylinder in the wind tunnel,  $d = 10\text{mm}$  80 seconds @ 10Hz,  
 $2 \times 500\text{W}$

Temperatures measured:  $213 \times 10^6$

**WT003** - heat transfer around cylinder in the wind tunnel,  $d = 30\text{mm}$  80 seconds @ 10Hz,  
 $2 \times 500\text{W}$

Temperatures measured:  $213 \times 10^6$

Overall, I have measured and processed about  $23.2 \times 10^9$  temperatures.